

Computer Simulations of
Phase Behavior and Adsorption Kinetics
in Metal–Organic Frameworks (MOFs)

Inaugural-Dissertation

zur Erlangung des Doktorgrades
der Mathematisch-Naturwissenschaftlichen Fakultät
der Heinrich-Heine-Universität Düsseldorf

vorgelegt von

Nicolas Höft

aus Frankfurt (Oder)

Düsseldorf, Oktober 2016

Aus dem Institut für Theoretische Physik II: Weiche Materie

Gedruckt mit der Genehmigung der
Mathematisch-Naturwissenschaftlichen Fakultät der
Heinrich-Heine-Universität Düsseldorf

Referent: Prof. Dr. Jürgen Horbach
Korreferent: Prof. Dr. Stefan U. Egelhaaf

Tag der mündlichen Prüfung: 28.11.2016

ACKNOWLEDGEMENTS

First and foremost I would like to thank Prof. Dr. Jürgen Horbach for advising and guiding me through my Ph.D. He has been a great, patient mentor with an excellent sense of humor who also was a valuable source of curses in many foreign languages.

Science is most enjoyable if you can collaborate and share your results. Therefore, I am grateful for the fruitful collaborations with Mojtaba Eshraghi, Christoph Janiak, Victor Martín-Mayor, Gamall Makhloufi and Beatriz Seoane. Thanks go also to Felix Höfling, who shares the same interest in modern C++ programming and discussing how to perfectly implement an algorithm for HALMD.

All of that would not have been possible without the support of my family and my friends. My parents, for whom education has always been important and encouraged me during my time at the University.

I also want to thank my colleagues and friends Saswati Ganguly, Mehrdad Golkia, Oliver Hielscher, Pegah Poshtareh, Gaurav Shrivastav and Nima Siboni for their time, discussions, and coffee we have shared at the institute.

Finally, thanks also go to Julian Bialke, Tobias Glanz, Matthias Kohl and Michaela Spiegel for proofreading this thesis and giving useful suggestions.

SUMMARY

Adsorption and condensation processes in porous materials have been the subject of many experimental and computational studies. In many porous materials, such as zeolites, the accessible void space is very narrow, thus the storage capacities and available inner surface area to guest molecules is quite limited. Conversely, metal–organic frameworks (MOFs) have much larger pores, only held together by an open framework structure. Consequently, guest molecules in MOFs are expected to show different phase behavior and adsorption kinetics compared to more closed porous materials.

In this thesis, we investigate phase transitions of methane (CH_4) in the metal–organic frameworks IRMOF-1, IRMOF-8 and IRMOF-16 (isorecticular MOFs) using extensive grand-canonical Monte Carlo (GCMC) computer simulations in combination with successive umbrella sampling. In IRMOF-1, we find two novel first-order phase transitions: (a) a transition related to the pore filling and liquefaction of the adsorbed gas in the void space and (b) a second transition at low densities and pressures on the inner surface of the MOF. While the first transition is similar to the liquid–gas transition in the bulk, thus called IRMOF-liquid–gas (ILG) transition, the nature of the IRMOF-surface (IS) transition has not been reported before. The structure of the coexisting phases is analyzed in detail. Remarkably, we find that in the IS transition the methane particles undergo a first-order phase transition between two heterogeneous bulk states where the gas particles are condensed on the surface of the framework. In the bulk phase at low densities gas particles cover the stronger interacting metallic corners of the MOF, only. This phase is in coexistence with a phase where the inner surface area of the framework is fully covered by methane particles.

The openness of the pores makes the phase behavior act differently from those in other confinements as (e.g., capillary condensation in thin films) where a cross-over to 2D Ising scaling behavior is observed asymptotically. Using finite-size scaling methods we determine that both the IS and ILG transition belong to the 3D Ising universality class. In MOFs with larger pores, IRMOF-8 and -16, very similar phases are observed, but the temperature range of IS transitions lowers with increasing pore diameter, making it increasingly difficult to observe the surface transition in IRMOF-16. Contrarily, the ILG condensation transition becomes more similar to the bulk CH_4 liquid–gas transition when the framework becomes more open and the pores larger.

The enrichment of methane molecules around the corners of the

framework allows us to define a local order parameter for the IS transition to distinguish between the coexisting phases by counting the adsorbed molecules around the metallic corners of the MOFs. With such a local order parameter we identify and study the structure and thermal fluctuations of the interface between the heterogeneous phases. We find evidence that the presence of the MOF suppresses thermal undulations along the interfaces.

We develop an Ising spin model where a similar framework structure as in IRMOFs is realized via frozen in spins. We show that this model can reproduce the phase behavior of the ILG phase transition. The simplicity of the Ising–IRMOF model allows for larger system sizes, thus finite-size corrections are suppressed and a more accurate finite-size scaling analysis close to the critical point is employed. We find small corrections to the universal value of the Binder cumulant of the 3D Ising model.

Finally, molecular dynamics (MD) computer simulations on graphics processing units (GPU) are employed to investigate the diffusion dynamics of methane in MOFs. In particular, the mobility of methane is almost identical in the two IS phases and unaffected by the critical point. The values of the diffusion coefficients that we find along the IS binodals are of similar order of magnitude as in previous experimental and theoretical works.

Moreover, our MD simulations are extended to simulate the adsorption kinetics of gaseous methane into a single IRMOF-1 grain. Even though in our simulations the pressure is two orders of magnitude lower than the bulk liquid–vapor coexistence pressure, we observe a condensation of methane in and around the grain. We find that the porous material acts as a nucleation site for the liquid–vapor transition in the bulk. As experiments indicate, such a condensation can also happen in MOF powder, where condensation bridges are formed between MOF grains. This affects adsorption measurements, by slowing down the particle kinetics significantly. Therefore, careful preparation in adsorption experiments with MOF powders is required in order to avoid condensation in the free volume between the MOF grains.

ZUSAMMENFASSUNG

Adsorptions- und Kondensationsprozesse werden sowohl experimentell als auch mit Hilfe von Computersimulationen seit langem untersucht. In vielen porösen Materialien, wie etwa Zeolithen, sind die für Gase zugänglichen Poren dabei sehr klein, was die Beladungskapazität und die innere Oberfläche begrenzt. Im Gegensatz dazu besitzen Metall-Organische Gerüste (metal-organic frameworks, MOFs) sehr viel größere Poren, die nur von einem offenen Gerüst zusammengehalten werden. Demzufolge ist zu erwarten, dass Moleküle in MOFs ein anderes Phasenverhalten sowie eine andere Adsorptionskinetik zeigen als in porösen Materialien, in denen sich die Teilchen weniger frei bewegen können.

Mittels großkanonischer Monte-Carlo-Computersimulation in Kombination mit sukzessivem Umbrella-Sampling untersuchen wir in dieser Arbeit Phasenübergänge von Methan (CH_4) in den Metall-Organischen Gerüsten IRMOF-1, IRMOF-8 und IRMOF-16 (isoretikuläre MOFs). Im prototypischen MOF IRMOF-1 beobachten wir zwei neuartige Phasenübergänge erster Ordnung: (a) Ein Phasenübergang, der mit dem Auffüllen der Poren durch die Gasmoleküle und deren Verflüssigung im Freiraum des porösen Netzwerks assoziiert ist. Sowie (b) ein zweiter Übergang auf der Oberfläche des MOFs (daher als IRMOF-Surface (IS)-Übergang bezeichnet), der bei kleinen Drücken und niedrigen Dichten auftritt. Während der erste Übergang dem Flüssig-Gas-Phasenübergang im Volumen ähnlich ist und dementsprechend als IRMOF-Flüssig-Gas (IRMOF-liquid-gas, ILG) bezeichnet wird, ist der zweite Übergang in der Literatur bisher noch nicht beschrieben worden. In der vorliegenden Arbeit werden die Strukturen der koexistierenden Phasen aufgeklärt und beschrieben. Bemerkenswert am IS-Übergang ist, dass das Methan dort einen Phasenübergang erster Ordnung zwischen zwei heterogenen Volumenphasen durchläuft: Einerseits haben wir eine Phase, bei der das Gerüst nur teilweise, nämlich an den metallischen Zentren bedeckt ist. Diese ist in Koexistenz mit einer anderen Phase, bei der die Gasteilchen auf der gesamten inneren Oberfläche kondensiert sind. Dieser Übergang wird hauptsächlich durch die inhomogene Struktur des Gerüsts verursacht. Dadurch, dass das Gerüstnetzwerk sehr offen aufgebaut ist, ist das Phasenverhalten anders als in anderen eingeschränkten Geometrien, wie zum Beispiel bei der Kapillarkondensation in dünnen Filmen, bei der am kritischen Punkt ein 2D-Ising-Skalenverhalten zu beobachten ist. Mit Hilfe von Finite-Size-Scaling-Methoden ermitteln wir, dass sowohl der ILG- als auch der IS-Übergang zur 3D-Ising-Universalitätsklasse gehö-

ren. In MOFs mit größeren Poren, wie IRMOF-8 und -16, sind sehr ähnliche Phasen zu beobachten, jedoch verschiebt sich der kritische Punkt des IS-Phasenübergangs zu derart niedrigen Temperaturen, sodass es zunehmend schwierig wird, diesen Übergang zu untersuchen. Im Gegensatz dazu wird der ILG-Übergang dem Flüssig-Gas-Übergang im Volumen immer ähnlicher, je offener und größer die Poren des MOF-Gerüsts sind.

Die Anreicherung von CH_4 -Molekülen an den Ecken des Gerüsts erlaubt uns die Einführung eines lokalen Ordnungsparameters bezüglich der IS-Phasenumwandlung, welcher es erlaubt, durch Zählen von Methan-Molekülen um ein einzelnes metallisches Zentrum, eine IS-Phase zuzuordnen. Mit diesem Ordnungsparameter identifizieren und untersuchen wir die Struktur und thermischen Fluktuationen entlang der Grenzfläche zwischen den koexistierenden Phasen. Wir zeigen, dass die Anwesenheit des MOFs Kapillarwellenanregungen entlang dieser Grenzflächen unterdrückt.

Wir entwickeln ein Ising-Spin-Modell, in dem mit Hilfe von eingefrorenen Spins eine ähnliche Gerüststruktur wie in IRMOFs nachgestellt wird. Wir weisen nach, dass dieses Modell in der Lage ist, die ILG-Phasen und die entsprechenden Phasenübergänge zu reproduzieren. Das Ising-IRMOF-Modell erlaubt die Untersuchung des Skalenverhaltens für größere Systeme als im atomistischen Modell. Aufgrund der viel größeren Systeme wird die Finite-Size-Scaling-Analyse nur noch von kleinen Korrekturen beeinflusst. Mit diesen Berechnungen bestimmen wir außerdem die Korrekturen zur universellen Binder-Kumulante des 3D-Ising-Modells.

Zum Abschluss dieser Arbeit führen wir Molekulardynamik (MD)-Computersimulationen auf Grafikkarten durch, um die Diffusionsdynamik von Methan in MOFs zu untersuchen. Es zeigt sich, dass die Beweglichkeit der Moleküle in beiden IS-Phasen fast identisch ist und kaum vom kritischen Punkt beeinflusst wird, in Übereinstimmung mit früheren experimentellen und theoretischen Arbeiten.

Die MD-Simulationen wurden daraufhin erweitert, um die Adsorptionskinetik eines Gases in ein MOF-Korn zu simulieren. Obwohl der Druck zwei Größenordnungen kleiner als der Koexistenzdruck des Flüssig-Gas-Übergangs ist, beobachten wir um und im MOF-Kristall eine Kondensation des Methans. Hierbei agiert der poröse Kristall als Nukleationskeim im Volumen. Experimente deuten an, dass eine solche Kondensation auch in den Zwischenräumen des MOF-Pulvers stattfinden kann und so die Adsorptionskinetik erheblich verlangsamt. Eine sorgfältige Durchführung von Adsorptionsmessungen ist erforderlich, um diese Gaskondensation zwischen den MOF-Kristallen zu vermeiden.

CONTENTS

| | | |
|-----|------------------------------------------------------|----|
| 1 | Introduction | 1 |
| 2 | Metal–Organic frameworks | 7 |
| 3 | Basics of phase transitions | 15 |
| 3.1 | The Ising model: The fruit fly for phase transitions | 16 |
| 3.2 | From the Ising model to simple fluids | 22 |
| 3.3 | Phase transitions in confinement | 23 |
| 4 | Methods | 27 |
| 4.1 | Computer Simulations | 27 |
| 4.2 | Modeling Methane and Metal–Organic Frameworks | 27 |
| 4.3 | Monte Carlo simulations | 30 |
| 4.4 | Finite-Size scaling | 37 |
| 4.5 | Molecular dynamics simulations | 39 |
| 4.6 | Cell- and Verlet neighbor lists | 42 |
| 5 | Results | 45 |
| 5.1 | Evidence for two critical points | 45 |
| 5.2 | Dependence on pore size | 51 |
| 5.3 | Structure and thermodynamic properties of interfaces | 64 |
| 5.4 | Ising model for gas condensation in MOFs | 72 |
| 5.5 | Adsorption kinetics and diffusion dynamics | 79 |
| 6 | Conclusions & Outlook | 91 |
| | Bibliography | 95 |

INTRODUCTION

Energy storage and transport are important aspects in our world: Cars would not drive, in case of a power blackout there would be no possibility to bridge the loss of power by a local energy storage. One of the open questions in this regard is how to store the energy? One very obvious solution is to use a simple fuel tank, put our gasoline in and be done; and for oil, this works very well. On the other hand, light gases, such as Methane and Hydrogen, have to be liquefied and compressed to very high pressures¹: an expensive and space consuming process. One method to lower the required pressures is to make use of adsorption in porous materials. The adsorption in porous media then is in principle similar to the condensation of water that is present in air on the surface of a window glass, but porous materials have a much larger (inner) surface, thus the amount of gas that can be adsorbed increases significantly. Adsorption processes are not only interesting for energy or gas storage, but are important to build molecular sieves, particle sensors or catalysis.

One very promising class of materials which have gained much interest in the last 15 years are metal-organic frameworks (MOFs) (Farrusseng, 2011). High chemical and mechanical stability, vast inner surface and the ability to tailor the structure by exchanging specific parts, makes MOFs particularly interesting for gas storage, filtering and as catalysts. One of the central experimental properties are adsorption isotherms, measuring the amount of gas adsorbed as a function of ambient pressure at a certain temperature. The six types of adsorption isotherms classified by the IUPAC² are shown in Figure 1.1. Mesoporous materials with pore diameters between 2 to 50 nm such as MOFs often show isotherms of type IV, while for example on planar surfaces or in macroporous adsorbents a type II isotherm is obtained, where the point B would indicate the point where a single wetting layer is formed and multilayer adsorption begins. A detailed discussion about the types of sorption isotherms can be found in Sing, Everett, et al., (1985), Gelb, Gubbins, Radhakrishnan, and Sliwinska-Bartkowiak, (2000), and Thommes, Kaneko, et al., (2015).

Using the adsorption isotherms, other properties of the porous medium can be determined, e.g. pore size distribution or surface area. It is common practice in chemistry to assume a layer-by-layer growth of the adsorbent on a planar surface. Applying Langmuir or BET theories³ assuming such a growth, an inner surface area can be calculated (Mason, Veenstra, and Long, 2014).

It is questionable whether such a simple model is applicable on



1. For example, *compressed natural gas* (CNG) is compressed to 20 to 25 MPa in order to improve the volume to energy ratio.

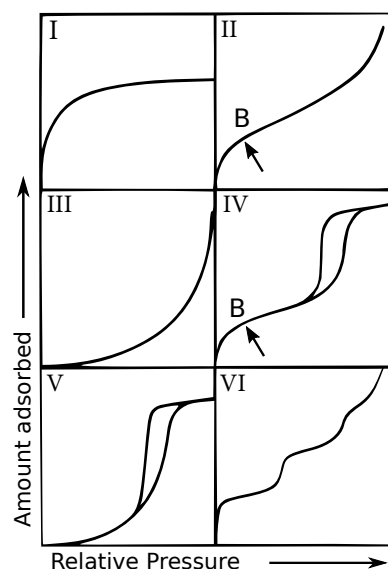


Figure 1.1: Schematic sorption isotherms and their classification of as per recommendation of IUPAC. Modified version from Sing, Everett, et al., (1985).

2. International Union of Pure and Applied Chemistry.

3. For the original works, see Langmuir, (1916), Langmuir, (1918), and Brunauer, Emmett, and Teller, (1938).

heterogeneous porous media such as MOFs, where the inner surface is not flat, but has a complicated surface structure along the framework, available to the guest particles. Applying BET theory to MOFs also requires a pressure regime where a (linear) growth in layers actually occurs (indicated by point B in Figure 1.1). If the pressure is too low the surface is covered inhomogeneously by the gas, and at very large pressures the gas will liquefy and fill whole pores. In addition to inner surface area measurements adsorption isotherms can be interpreted to reveal hierarchies in the porous structures – for example, multistep features may indicate a network of small and larger pores as large pores get filled only at high relative pressures (Sing, 2001). Note that often these isotherms show hysteresis loops, i.e. the adsorption is different whether one increases or decreases the pressure. Only one of these curves can satisfy thermodynamic equilibrium, but the system may be stuck in a well-defined metastable state and could be associated with a liquid–vapor like phase transition (F. Rouquerol, J. Rouquerol, et al., 2014). While having a similar shape as type VI isotherms (c.f. the occurrence of steep jumps at certain pressures) it is completely unrelated to its usual interpretation of adsorption in pores of different sizes. Also, phase transitions may affect the kinetic behavior of pore filling and evacuation significantly. Therefore, knowledge about phase transitions in MOFs is of important practical relevance – but difficult to understand without information at molecular length scales, which is not provided by adsorption isotherms.

While adsorption experiments only provide a macroscopic information, X-ray diffraction (XRD) and Nuclear magnetic resonance (NMR) measurements at low pressures have shown that, depending on the loading of the MOF (Rowell, Spencer, et al., 2005; Braun, J. J. Chen, et al., 2015), a structural change of the preferred adsorption sites takes place. This is a very different behavior from “classical” adsorption on a planar surface where a homogeneous layer-per-layer adsorption can be assumed, and isotherms cannot resolve such differences. While adsorption isotherms are a useful measure for the loading of guest particles, it does not tell anything about *where* the guest particles are. Note that adsorption isotherms are often given in units of the vapor saturation pressure P_0 on a linear axis. For many gases P_0 is in the order of kPa at room temperature (20 °C) (e.g. Ethanol 5.83 kPa, Water 2.3 kPa), but can be also much higher, as in the case of CO_2 , where $P_0 = 5.7$ MPa. To observe the preference of the guest molecules to certain sites in the MOF structure, very low pressures are required, as only a small number of particles is adsorbed in these phases. Thus, it is useful to plot the pressure on a logarithmic scale instead of linear scale (as used in Figure 1.2) to resolve possible phase transitions in this parameter range.

Methane, being the most simple hydrocarbon, is quite important as a candidate for energy storage, since burning CH_4 produces only a single CO_2 molecule⁴, therefore having a smaller carbon dioxide footprint than burning oil while having a slightly higher heat of combustion (M. Q. Wang and Huang, 2000). Additionally, methane is easy to model which makes it a good prototype to study the phase behavior

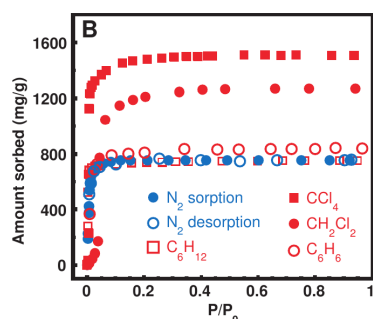


Figure 1.2: Adsorption isotherm as a function of pressure P relative to the vapor pressure P_0 in IRMOF-6 at 78 K. Source: Eddaoudi, Kim, et al., (2002).

4. Under ideal conditions Methane burns as $\text{CH}_4 + 2\text{O}_2 \rightarrow \text{CO}_2 + 2\text{H}_2\text{O}$.

in MOFs using computer simulations, predict associated equilibrium adsorption isotherms and characterize the coexisting phases. With the use of computer simulations we can give information about the microscopic structure and kinetics involved in the phase transitions being inaccessible otherwise and are able to explore the parameter space much faster and in a more controlled way than experiments can often do. For example, [Toni, Pullumbi, Coudert, and Fuchs, \(2010\)](#) were able to predict a first-order phase transition of carbon dioxide in IRMOF-1⁵ with a critical temperature 30% below the T_c of bulk CO₂ using computer simulations.

Their result is compatible with what is known from thin film confinements (discussed in, e.g. [Binder, Horbach, Vink, and De Virgiliis, \(2008\)](#)): Depending on the distance of the confining walls, the critical point as well as the width of the coexistence region can be tuned. A strong confinement (i.e. a narrow slit) causes the critical temperature to be lowered significantly and can change the phase behavior in general reducing the dimensionality of the transition from three to two-dimensional behavior. In another work done by [Lenz and Lipowsky, \(1998\)](#) it is shown that wetting layers on patterned surfaces exhibit transitions between a homogeneous and inhomogeneous phases, depending on the droplet volume and contact angle.

The aim of this thesis is to characterize the phase transitions that can be observed in the confinement of MOFs and compare their structural and kinetic properties of the coexisting phases these to the bulk liquid–vapor phase transition of methane using computer simulations. As shown in this work, by varying the pore size, one can change the width and critical point of the liquid–vapor coexistence region at presence of the framework – where there is the trend that smaller pores cause a lower critical temperature. This IRMOF-liquid–gas (*ILG*) transition has a shifted coexistence region towards higher densities, due to a wetting layer on the inner surface in the gas phase of the pores. While the thin film geometry restricts the growth of critical fluctuations eventually on two dimensions, therefore reducing the effective behavior from 3D- to 2D-universality class, such a cross-over scaling is not expected in MOFs since the fluid is not spatially restrained in any way: all pores are open and connected to each other.

Further, the previously mentioned heterogeneity of the surface of the MOF induces a new type of phase transition (*IRMOF-Surface (IS)* transition) between two three-dimensional inhomogeneous phases. These heterogeneous phases are characterized by a partial (at low densities) wetting of the corners of the framework and a complete wetting layer (at higher densities) on the inner surface of the MOF. Compared to the liquid–gas transition, the IS transition occurs in IRMOF-1, the prototype of MOFs ([H. Li, Eddaoudi, O’Keeffe, and Yaghi, 1999](#)) and a member of the large class of “IRMOFs”, at pressures 3 – 4 orders of magnitudes lower than the bulk coexistence pressure. This raises the question how the interface between heterogeneous phases behaves in IRMOFs. We study if thermal fluctuations of the interface can be suppressed by the MOF structure and how the structure of the interface between the IS phases is affected by heterogeneous coexisting phases.

5. IRMOF-1, also known as MOF-5 is one of the most prominent MOF, first synthesized by [H. Li, Eddaoudi, O’Keeffe, and Yaghi, \(1999\)](#).

We also want to understand to what extent the external field (due to the framework) can influence the geometry of phase interfaces.

Comparing the phase behavior of CH₄ in other IRMOFs, IRMOF-8 and -16, reveals that the critical points of the IS and ILG phase transitions can be shifted by tuning the pore size (IRMOF-16 has the largest pores, with IRMOF-8 being in between IRMOF-1 and -16): With increasing pore size the ILG transition becomes more bulk-like as its critical temperature is higher and the coexistence density region becomes broader. The IS transition is affected in the reverse, the density differences between the phases become smaller and the critical temperature lower, making the IS practically inaccessible or absent in the system with the largest pores.

As the phase behavior is very complicated, to reduce computational effort it is tempting to introduce a minimal model for gas condensation in a MOF-like porous structure, while preserving the features of phase transitions in MOFs. In collaboration with Beatriz Seoane and Victor Martin-Mayor we have developed a minimal model based on Ising⁶ system. In this model spin particles are placed on a lattice. The only allowed value for the spin are up and down, they can align to the neighboring spins or, if an external (magnetic) field is applied, they may align to this field. Even though the microscopic physics is very different, by carefully recreating the geometry we are able to reproduce the structure ILG phases behavior of the MOFs in the Ising model. Using this model we are able to study systems of larger scale, which allows for more accurate measurements of the universal behavior in (MOF) confinements.

As it turns out, finding evidence of the IS and ILG phase transitions in experiment becomes difficult, because the liquid–vapor phase transition of the bulk can cause liquid droplets to form on MOF grains. Condensation of the gas on the grain can become a quite important effect, since MOFs are typically in powder form, thus have also a large outer surface, meaning the gas would not be *inside* the MOF, but between MOF grains. Adsorption experiments done by Gamall Makhloufi at the Heinrich-Heine Universität Düsseldorf and computer simulations on single MOF grains give evidence that this is indeed the case.

This thesis is organized as follows. After this introduction metal–organic frameworks are briefly described and an overview of their physical and chemical properties is given. The third chapter gives an introduction into phase transitions using the Ising model to describe the physics and observations as they occur in phase transitions and in the vicinity of the critical point, the “end point” of phase coexistence. The critical point is of certain importance as many phase transition show the same qualitative (universal) behavior, even though they are microscopically very different.

Then, in Chapter 4 (p. 27) computational methods required to study phase transitions and adsorption kinetics are presented. It includes an introduction to grand canonical Monte Carlo (GCMC) methods, finite-size scaling, molecular dynamics (MD) simulations and their application to our problem. While GCMC is used to generate

6. The Ising model is a lattice model originally developed to describe ferromagnetism.

equilibrium configurations and for the calculation of coexistence points in the phase diagrams, MD simulations (on computer graphics cards) allow for the study of kinetic properties related to, e.g. diffusion dynamics.

Equipped with the above algorithms and methods, Chapter 5 (p. 45) presents the results. There are five main findings in this work:

1. We observe two novel lines of first-order phase transitions, both ending in a critical point. One line is associated with a liquid–vapor like transition related to the pore filling. The other one, here reported for the first time, is related to the transition on the inner surface of the framework. In the following we call these transitions ILG- and IS transition, respectively.
2. Studying three different MOFs, we observe that, with respect to temperature and density range, the location of both phase transitions can be tuned upon varying the pore size.
3. We analyze the interface between the coexisting inhomogeneous phases of the IS transition and reveal a suppression of thermal fluctuations along the interface. Evidently, the presence of the framework is inhibiting this kind of distortions in the interface structure. Further, our results show 3D Ising compatible scaling behavior in the critical region of the IS transition.
4. We introduce an Ising model resembling a MOF structure and reproduce the ILG phase behavior as found in MOFs. This minimal and therefore computationally faster model allows to study the critical scaling and universality with greater accuracy.
5. Also, the diffusion dynamics and adsorption kinetics of methane in MOFs are studied. We calculate diffusivities of the IS phases with respect to single particle– and collective diffusion dynamics. Further, the adsorption kinetics are studied on single MOF grains to understand microscopic details of the adsorption required to understand adsorption isotherms obtained from experiments.

METAL–ORGANIC FRAMEWORKS

Metal–organic frameworks (MOFs), also referred to as porous coordination polymers (PCP), are a relatively new class of porous media of very large pore volume and inner surface area. The definition as recommended by [Batten, Champness, et al., \(2013\)](#) is as follows:

A metal–organic framework, abbreviated to MOF, is a coordination network with organic ligands containing potential voids.

They consist of two building units: The metallic cluster, also known as *secondary building unit* (SBU) and the organic linkers, connecting the SBUs and forming the framework. This topology enables uncountable possibilities of building many framework topologies and allows for tailoring porosity, reactivity (e.g. by adding side chains with catalytic properties to the linkers), magnetism and other physical or chemical properties ([Janiak and Vieth, 2010](#)). The remarkable properties of MOFs have gained interest in the scientific community greatly in the last decade as indicated by the rapid increase of publications on these materials in the last 15 years (cf. Figure 2.1).

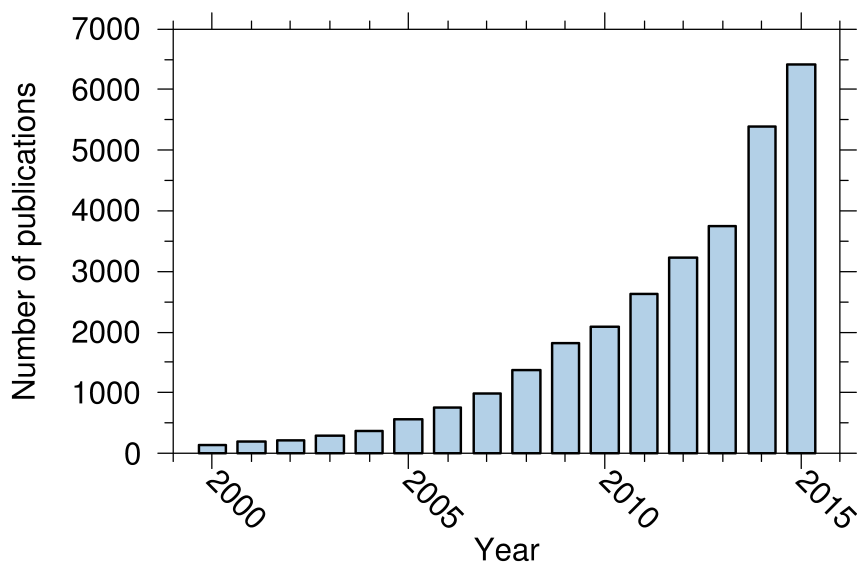


Figure 2.1: Number of publications with keywords “Metal–organic framework” or “mof” from 2000 – 2015 as determined from Thomson Reuters Web of Science.

2

Adsorption in MOFs



Figure 2.2: Powder of MOF as it is prepared for adsorption measurements.

In recent years, a vast number of MOFs have been synthesized and categorized by their physical and chemical properties. As in other porous media, one of the most important properties of MOFs are adsorption isotherms. They measure the amount of guest molecules that can be adsorbed by the framework as a function of the pressure at constant temperature. Adsorption isotherms are experimentally easily accessible and they give already information about the inner surface that is available for the gas molecules in a porous medium. In volumetric adsorption experiments, the MOF samples (typically a powder as in Figure 2.2) are evacuated and the test tube is put into a bath or thermostat with the desired temperature. Then a valve is opened to allow further gas to enter the tube until the target pressure is reached and the system is in equilibrium (or after a certain time interval). Repeating this for a number of pressures, one obtains the adsorption isotherm. Alternatively, instead of measuring the volume, one can also use the gravimetric method, where the changes in weight of a sample are recorded instead.

From an adsorption isotherm one can quantify the specific inner surface area using the BET theory, selectivity¹, pore volume and distribution (Barrett, Joyner, and Halenda, 1951), or hysteresis effects. The BET equation, based on an empirical model, reads²:

$$\frac{p/p^0}{n(1-p/p^0)} = \frac{1}{n_m C} + \frac{C-1}{n_m C} \left(\frac{p}{p^0} \right), \quad (2.1)$$

where p is the pressure, p^0 is the vapor pressure, n the amount of gas adsorbed by the material, n_m the monolayer capacity. The parameter C is associated exponentially with the energy of monolayer adsorption and the value of C can indicate the shape of the adsorption isotherm (in the BET range). The objective is to derive the monolayer capacity n_m to calculate the inner surface area using the average area σ the test molecule occupies on the surface. Typically, one uses Nitrogen at 77 K (which has a molecular cross section $\sigma = 0.162 \text{ nm}^2$) to obtain the BET area. One of the four criteria (J. Rouquerol, P. Llewellyn, and F. Rouquerol, 2007) to select the valid pressure range for BET calculation is that if $n(p^0 - p)$ is plotted as a function of p/p^0 , the valid range must be below the maximum (cf. Figure 2.3b). In this range the BET plot of $(p/p^0)/[n(1-p/p^0)]$ should become linear. From the intersection with the axis and the slope of the fitted curve according to Eq. (2.1) this allows to determine the quantities n_m and C . However, identifying the relevant linear pressure range from adsorption in micro- or mesoporous materials is more complicated, as shown in Figure 2.3. In the shown case the slope in the BET curve is not constant with increasing pressure, and one could identify three different linear regions in the BET plot (plus a linear fit over the whole curve). While there exist criteria (Thommes, Kaneko, et al., 2015) which region to select by omitting nonsensical results, an interpretation of the other ranges remains unclear nonetheless. Further, the result only gives information about the area that is accessible at

1. In gas mixtures, the selectivity compares the amount adsorbed for each species at a certain pressure.
2. A derivation of the equation can be found in F. Rouquerol, J. Rouquerol, et al., (2014).

this measured temperature with the test gas. Other gases at different temperatures can behave very differently and “see” a different surface. However, the MOF community is well aware of the above problems in the BET calculations, thus calling the determined area “BET area” is preferred over “BET surface area”³ and is still a useful quantity to validate synthesized material with reference values of the BET area. Therefore, it is also understood and used as a “fingerprint” for the material (Thommes, Kaneko, et al., 2015). As stated in the review by Thommes and Cychosz, (2014), one of the big challenges in the detailed understanding of physical adsorption includes the development of new simulation methods coupled with advanced experimental protocols.

3. Simulation studies by Walton and Snurr, (2007) and Bae, Yazaydin, and Snurr, (2010) suggest that the accessible N₂ area can be very similar to the BET area.

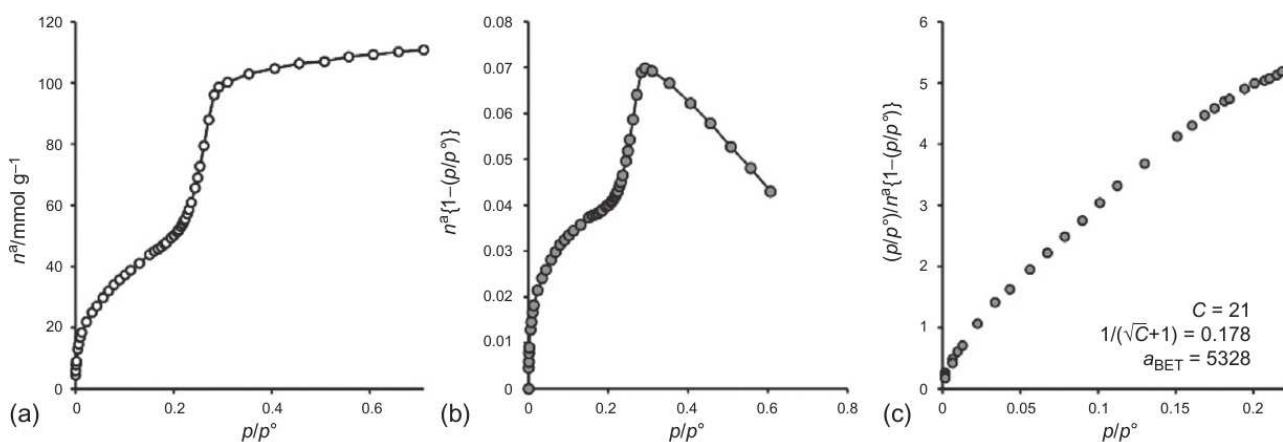


Figure 2.3: a) Nitrogen adsorption isotherm for NU-109 at 77 K. Consistency plot as shown in b) determines the maximum pressure range to consider for BET calculation – only pressures below the maximum $p/p^0 = 0.28$. The BET plot in c) becomes inconclusive, consisting of multiple linear regions. From F. Rouquerol, J. Rouquerol, et al., (2014) with data from Farha, Eryazici, et al., (2012).

| Material | BET area (m ² /g) | Reference |
|------------------------------|---------------------------------|--------------------------------------------|
| ZSM-5 | 260–310 | Sang, Chang, et al., (2004) |
| LTA-SiO ₂ zeolite | 695 | Palomino, Corma, Rey, and Valencia, (2010) |
| IRMOF-1 | 2833 | Millward and Yaghi, (2005) |
| IRMOF-8 | 4326 | Feldblyum, Dutta, et al., (2013) |
| MIL-101 | 4230 | P. L. Llewellyn, Bourrelly, et al., (2008) |

Table 2.1: BET areas for various MOFs and zeolites from N₂ adsorption at 77 K. Note that depending on the reference, the reported BET areas for the MOFs may be significantly different (cf. Mason, Veenstra, and Long, (2014)).

Comparison to zeolites

While MOFs have been developed out of zeolite⁴ research (Cheetham, Férey, and Loiseau, 1999), their high modularity and porosity (large

4. The term *zeolite* was introduced by the swedish chemist Axel Cronstedt, who observed that some minerals appear to boil while heating, thus calling them “boiling stones”, greek “zeolite”.

inner surface area and pore volume, cf. Table 2.1) makes MOFs competitive to zeolites. Zeolites are porous inorganic minerals with frameworks constructed of SiO_4 and AlO_4 tetrahedra, interlinked with each

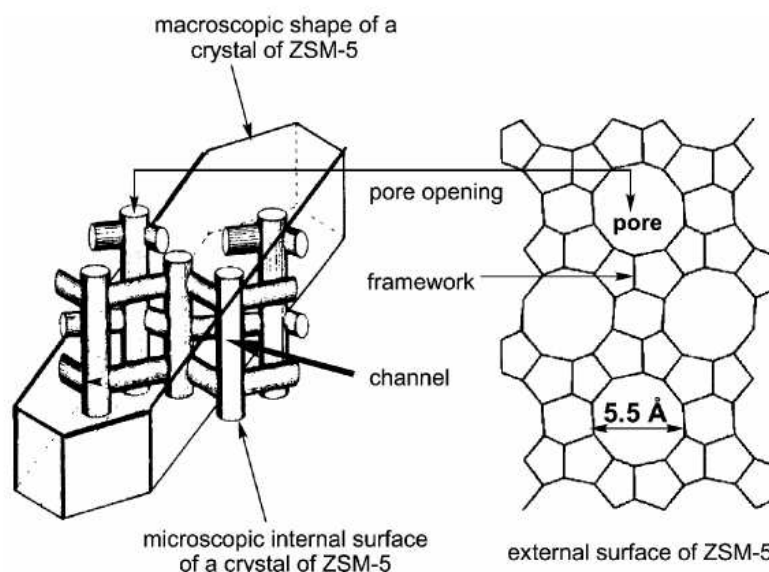


Figure 2.4: Pore structure of ZSM-5 zeolite. Pores are connected by narrow channels. From [Lei, Jockusch, Ottaviani, and Turro, \(2003\)](#).

other. They are extremely stable (mechanically as well as chemically) and have very high melting temperatures $> 1000\text{ }^\circ\text{C}$. Some structures occur naturally (e.g. herschelite, mordenite and others) but are also synthesized and both are used in industry for water purification, odor control and more ([S. Wang and Peng, 2010](#); [Virta and Flanagan, 2015](#)). Zeolites have pore networks with diameters below $10\text{ }\text{Å}$ and typically form cylindrical narrow channels, as displayed in Figure 2.4 for one of the most prominent zeolite, ZSM-5. Similarly to MOFs, zeolites are interesting for capture of CO_2 and many computer simulations studies have been done to understand the adsorption in zeolites. Limiting in the application of zeolites are the narrow pores which can inhibit mass transport (diffusion) in and out of the pores. Channels may also be clogged by large molecules, decreasing the catalytic performance of these materials. Metal-organic frameworks, on the other hand, have very open, easily accessible pores, which allow higher diffusivities in the pores. With their building block approach one can easily exchange of linkers or metallic clusters, which allows for larger pore sizes and a huge variety of structures, as the examples of MIL-101 and MIL-53 (displayed in Figure 2.5) indicate. In contrast to zeolites, which are used in petrochemical industry, a large-scale application of MOFs has not appeared yet, due to difficult synthesis and therefore high production cost ([Yilmaz, Trukhan, and U. Müller, 2012](#)). But as the synthesis of new materials and the development of new techniques is an active field of research, a breakthrough is still possible.

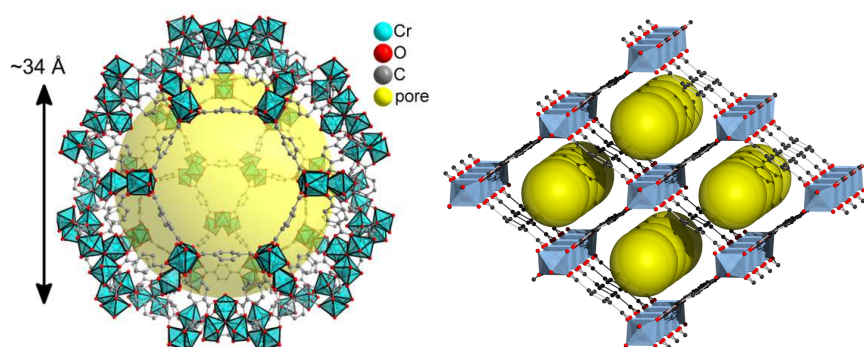


Figure 2.5: Different topologies of the framework structures. On the left a schematic picture of MIL-101, a MOF with spherical pores with diameters of $\approx 34 \text{ \AA}$, from Jeazet, Koschine, et al., (2013). Right: MIL-53ht, a MOF with rhombic channels and a pore diameter of 8.5 \AA , first described by Loiseau, Serre, et al., (2004). Image from Wikimedia Commons, (2010).

MOFs used in this work

A particularly promising application for MOFs is methane storage⁵ and separation of $\text{CH}_4\text{-CO}_2$ mixtures for natural gas upgrading (Zhang, Sunarso, S. Liu, and R. Wang, 2013). There, a detailed knowledge about adsorption of methane on the inner surface and an understanding of the phase behavior is important to understand the macroscopic adsorption. We expect this to be relevant also for other gases, such as Hydrogen (energy storage), Water (dehumidification) and so on.

5. For a recent review about methane storage in MOFs see He, W. Zhou, Qian, and B. Chen, (2014).

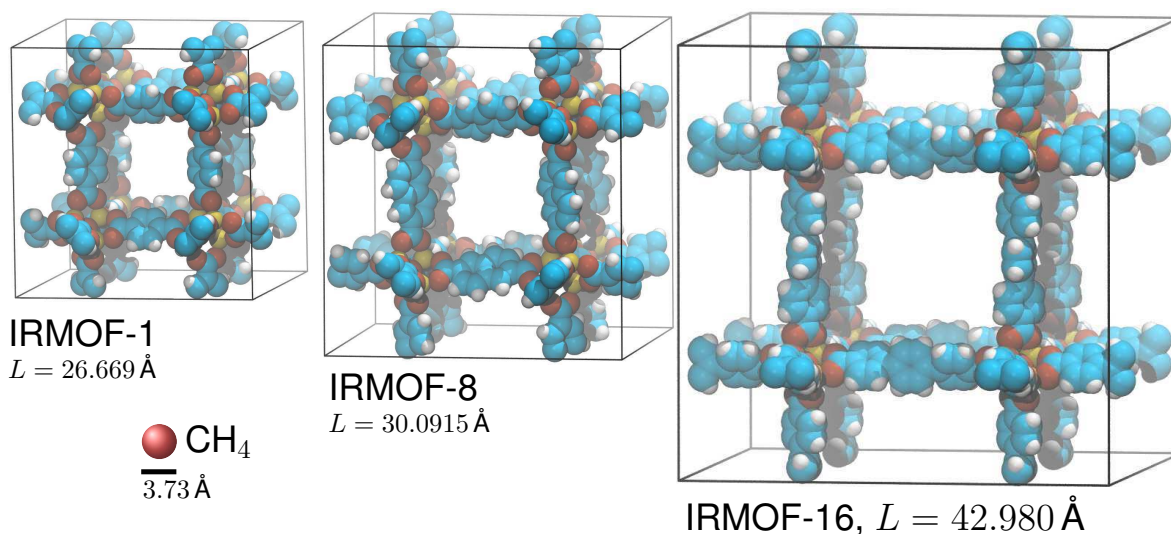


Figure 2.6: Unit cells of exemplary MOF structures from left to right: IRMOF-1, IRMOF-8 and IRMOF-16. These structure have identical metallic centers but different ligands, therefore tuning the pore size. Methane molecule diameter as approximate reference length scale.

The MOFs studied in this work are different variations of the “IRMOF”-class. The acronym stands for *Isoreticular metal-organic framework*. As defined in Random House Webster Unabridged Dictionary, “reticular” means “net-like”, or “having the form of a net”. Therefore,

isorecticular is defined as “having the same network topology”. Three types of IRMOFs (IRMOF-1, -8, and -16) are shown in Figure 2.6.

While structurally extremely similar (only the ligands connecting the metal oxides at the corners are different), they vary in mechanical stability and inner surface area. Due to the large free volume in IRMOF-8 and -16 they often form (doubly) interpenetrated porous networks as in the example shown in Figure 2.7. Interpenetration increases the mass density, inner surface area and reduces the free volume of the MOF and must be considered during synthesis, but interpenetrated MOFs are not within the scope of this work. In our model we must introduce simplifications, such as we fix the MOF atoms at their positions. Thus, we will be unable to study *breathing*

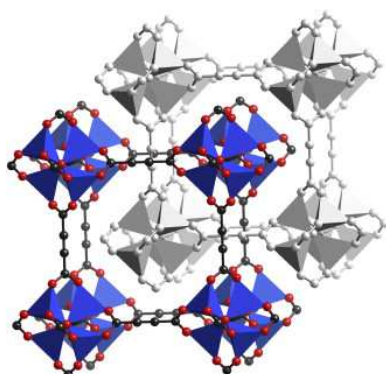


Figure 2.7: Structure of doubly interpenetrated IRMOF-0, the second interpenetrating framework is shown as in gray. Source: [Tranchemontagne, Hunt, and Yaghi, \(2008\)](#).

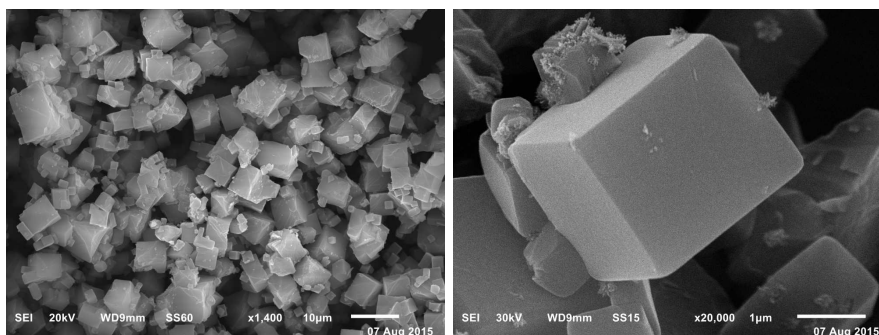


Figure 2.8: Raster electron microscopy (REM) images of IRMOF-1. Due to the cubic geometry of the unit cell, the macroscopic crystals become cubic, too. Shot taken by Gamall Makhoulfi from HHU.

of MOFs, where the crystal deforms upon gas loading ([Coudert, Boutin, Fuchs, and Neimark, 2013](#)). From crystallographic analysis it can be also shown that the metallic clusters in IRMOFs display a structural isomerism: One way to place the metallic center is by simple translation or by introducing an additional rotation, see Figure 2.9. In principle, it is random which metal center is rotated. The linker itself is not necessarily affected from this isomerism (e.g. by a rotation). Even though the structure does not change dramatically and previous

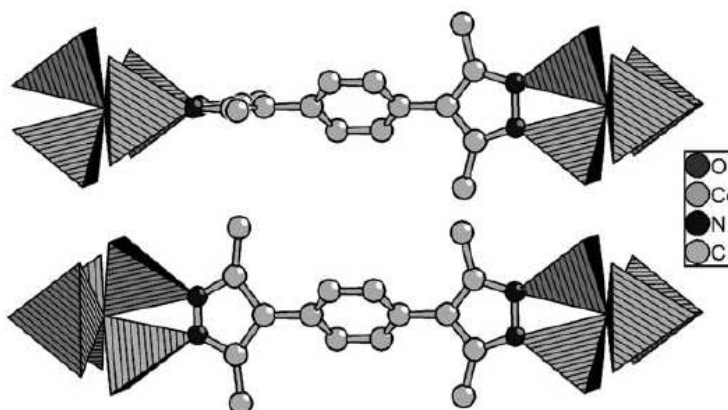


Figure 2.9: Two possible conformations of metallic centers in MFU-1. Such a rotation of the ionic clusters can be found in IRMOF-1, too. From [Tonigold, Lu, et al., \(2011\)](#).

simulation studies do not include this property, it is important to be aware of this behavior, as it may become important when comparing the numeric results to experimental observations. Other MOFs, e.g. MFU-4 developed at the University Augsburg (Biswas, Grzywa, et al., 2009) do not have this isomerism, which exhibits the same topology as IRMOF-1.

The crystalline structure of the IRMOF class features a cubic symmetry. Thus, the grains, which have edge lengths up to 10 μm , form also cubic crystals, as shown in the REM image in Figure 2.8.

Computer simulation studies by Toni, Pullumbi, Coudert, and Fuchs, (2010) have already shown the existence of a phase transition of CO_2 in IRMOFs and with the prediction of adsorption isotherms as shown in Figure 2.10. Magdysyuk, Denysenko, et al., (2014) have studied crystallization of Xenon in MOFs, observing preferred adsorption sites on the inner surface, similar to what Rowsell, Spencer, et al., (2005) have reported. Thus, phase transitions in MOFs have gained

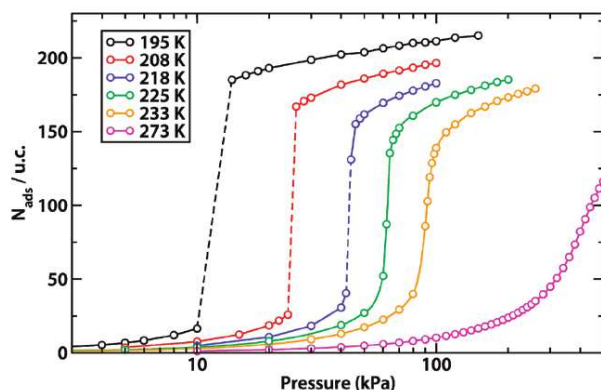


Figure 2.10: Adsorption isotherm as determined from computer simulation studies where at temperatures lower than 225 K a phase transition occurs. Dashed lines indicate the first-order phase transitions and coexistence regions.

some interest in the scientific community. To understand what a phase transition is and what interesting phenomena can be found in such state changes will be elucidated in the following chapter.

BASICS OF PHASE TRANSITIONS

Matter can be found in very different states, one of the examples known to everyone is water. The states of water that are best known in everyday life are ice (solid), water (liquid) and water vapor (gas) – and all of them can coexist:

1. Liquid water and ice: An iceberg floating in the ocean.
2. Vapor and ice: During winter, at temperatures below 0°C , water will freeze to ice and coexist with steam.
3. Liquid and vapor: This is observed at room temperature. It is most obvious when boiling water: A part of the liquid will evaporate and forms gas bubbles in the water.
4. At the triple point of water (at 273.16 K and 611.73 Pa) all states of matter coexist and very small changes to temperature or pressure can already fully transform the substance into liquid, ice, or gas.

Except for the triple point, these phenomena are well known from everyday life, and are neither limited to water nor must the phase be liquid, gas, or solid – matter can form diverse types of phases. For example, a phase can be defined by its density, the concentration of a species in a binary mixture, the structural order, magnetization or conductivity. If these properties change and a new phase is formed and both phases can coexist at the same time, then a *phase transition* is taking place. During a first-order phase transition an *order parameter* relevant for the transition makes a sudden jump with respect to an intensive thermodynamic variable. In the liquid–vapor transition, for example, the order parameter is the density. The information under which conditions phase transitions occur, are maintained in phase diagrams. For water, such a phase diagram is given in Figure 3.1a (see also [Wagner, Saul, and Pruss, \(1994\)](#)). The above p-T diagram shows coexistence pressures as a function of temperature. Note that water is somewhat exceptional; there, the coexistence pressure of ice and water *increases* with temperature. This is one of the many anomalies of water – as increasing the pressure usually favors a solidification.

Both pressure and temperature are intensive thermodynamic variables¹ and at phase coexistence all the intensive variables must be equal, as the phases must be in thermodynamic equilibrium. Extensive variables, on the other hand, may show a discontinuity: The densities between liquid and vapor phase are distinct and exhibits a jump in the Pressure-Volume plane (cf. Figure 3.1b).

3

1. Intensive variables (such as temperature, pressure, or chemical potential) are invariant of system size. Extensive variables depend on the system size, examples are particle number, volume, or inner energy.

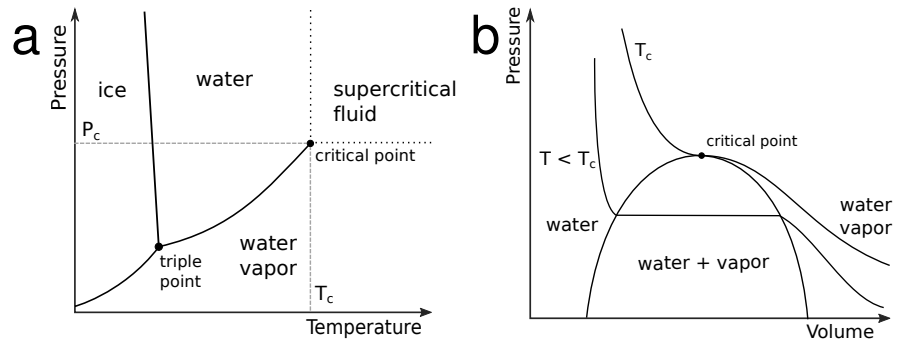


Figure 3.1: Simplified phase diagram of water in the Pressure–Temperature (*a*) and pressure–volume (*b*) plane. Solid lines in the p-T plane denote coexistence curves of water, vapor, and ice. Plateaus in the V-P plane of isotherms represent the coexistence region of vapor and liquid. At supercritical temperatures, the plateau vanishes a continuous transition takes place instead.

2. The correlation length ξ is the “typical” length scale over which microscopic fluctuations are correlated.

3. The absence of a characteristic length scale is also a key feature of fractals.

One observes that – in contrast to the liquid–solid transition – the liquid–vapor phase transition (and also the order parameter) vanishes above a certain temperature. This point denotes the *critical point* of the fluid and is of certain importance. At the critical point, the correlation length² ξ associated with density fluctuations diverges³; if the correlation length becomes infinite, in return it means that very small changes can change the whole system very quickly. Critical opalescence, observed in regions of second order phase transitions (also said to be continuous), is one of the effects caused by the large fluctuations. In this region many thermodynamics properties act in a scale-invariant manner.

Scale invariant behavior implies an underlying power-law behavior. Even with this large variety of phase transitions, it turns out they can be classified by their power-law exponents. This *universality class* is set by the dimensions of the system space and order parameter. It means that different phase transitions can obey the same universal (power) laws and allows for studying simplified systems while learning about the characteristics of very distinct systems. For example, the three-dimensional spin lattice with the magnetization as an order parameter (i.e. the 3D-Ising model) lies in the same universality class as the liquid–vapor transition in simple fluids. As the Ising model is of such importance to this date, a brief introduction follows in the next section.

3.1 The Ising model: The fruit fly for phase transitions

As noted above, the phenomena present in phase transitions become universal in the vicinity of a critical point, meaning that exponents of very distinct systems are identical. One of the most important system for the study of phase transition is the Ising model, which was introduced to describe ferromagnetic behavior in solids (Ising, (1925), for a review about the history see Niss, (2005), for example). In the Ising model, particles are placed on a lattice and assigned a

“spin” s , which can have the value $+1$ or -1 (\uparrow and \downarrow , respectively). Interactions between the spins is restricted to the nearest neighbors and an external magnetic field may be applied, to which the spins align to with a certain probability. The Hamiltonian $\mathcal{H}_{\text{Ising}}$ of this system with N particles in the configuration $\mathbf{s} = \{s_1, \dots, s_N\}$ is given by

$$\mathcal{H}_{\text{Ising}}(\mathbf{s}) = -J \sum_{\langle i,j \rangle} s_i s_j - H \sum_{i=1}^N s_i, \quad (3.1)$$

where $\sum_{\langle i,j \rangle}$ denotes the sum over all nearest neighbors of particles, J is *exchange energy* of nearest-neighbor interaction and H the constant external magnetic field.

The equilibrium probability for a configuration \mathbf{s} at a given inverse temperature $\beta = 1/k_B T$ can be expressed by

$$P(\mathbf{s}) = \frac{1}{Z} e^{-\beta \mathcal{H}_{\text{Ising}}(\mathbf{s})}, \quad (3.2)$$

where $Z = \sum_{\mathbf{s}} e^{-\beta \mathcal{H}_{\text{Ising}}}$ is the partition function summing over all possible configurations \mathbf{s} , which normalizes $P(\mathbf{s})$ such that $\sum P(\mathbf{s}) = 1$. At higher temperatures the spins will show like a paramagnetism: If the external field is turned off, the average magnetization per spin will be zero. If the field is turned on, spins will align towards this field. $H > 0$ will prefer $\sigma = +1$ and for $H < 0$ more spins will be $\sigma = -1$. However, at lower temperatures the spin-spin contributions become more important and the system shows ferro- or anti-ferromagnetic behavior. There, the spins align with the external field and keep a net magnetization even in the absence of the magnetic field.

In the following we assume $J > 0$, i.e. ferromagnetic behavior. From Eq. (3.1), we can see that the alignment of spins is more likely⁴ and that with increasing external magnetic field strength H , spins will have a preferred alignment along the field.

One observable quantity in the Ising ferromagnet is the magnetization per spin, defined by

$$m = \frac{1}{N} \sum_{i=1}^N s_i, \quad (3.3)$$

which is in the range from -1 (all spins down) to $+1$ (all spins up). This can be also expressed by means of partial derivatives of the partition function:

$$m = \frac{k_B T}{N} \left. \frac{\partial \ln Z(N, H, T)}{\partial H} \right|_T. \quad (3.4)$$

In the Ising model one observes the following for m (Cipra, 1987): If we are at a high temperature with the external field H , spins will align preferably along this external field, depending on its strength. If H is reduced, the system will go into an disordered paramagnetic state and the magnetization will vanish.

4. In an anti-ferromagnetic system where $J < 0$, the ground state is given by alternating spins ($\uparrow \downarrow \uparrow \dots$).

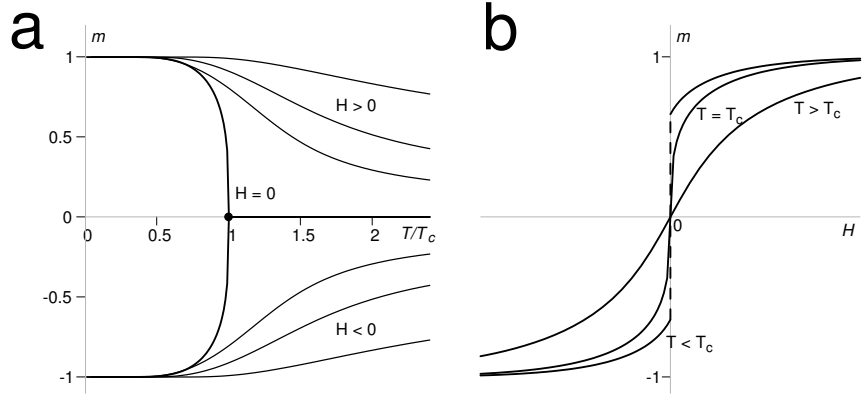


Figure 3.2: Sketch of phase diagrams of the Ising model in the temperature– (a) and external field–magnetization (b) plane.

Repeating the experiment below a certain (critical) temperature T_c , a certain magnetization will persist instead. This *spontaneous magnetization* at zero magnetic field is a first-order phase transition and the order parameter is m , as defined above. The phase diagram in the m - T plane is shown in Figure 3.2. The shown binodal curve defines the parameter range where a phase coexistence appears from the one phase region. Coexisting phases, on the other hand imply there is an interface between the two phases. According to Eq. (3.2), this interface is minimized in an equilibrated system. Thus, in finite sized systems, the form of the interface depends strongly on the geometry of the system.

The interface has some interesting properties: First, there are thermally caused undulations and *capillary wave theory* (CWT) (Buff, Lovett, and Stillinger Jr, 1965; Bedeaux and Weeks, 1985) is a framework to describe long-wavelength distortions along the interface. Capillary waves result from Goldstone modes in symmetry-broken systems (a phase-separated system breaks translational symmetry). The Goldstone theorem (Wallace, 1982) predicts an excitation of low-energy modes. These modes cost no energy as the wave number $q \rightarrow 0$ and introduce a displacement $h(x, y)$ in the surface perpendicular to the interface.

According to capillary wave theory, the height-height correlation function in Fourier space $\langle h(\mathbf{q})h(-\mathbf{q}) \rangle$, with $h(\mathbf{r}) = h(x, y) = \frac{1}{L} \sum_{\mathbf{q}} h(\mathbf{q}) e^{i\mathbf{q} \cdot \mathbf{r}}$ behaves in the limit of infinite system size $L \rightarrow \infty$ like

$$\langle |h(\mathbf{q})|^2 \rangle = \frac{k_B T}{\gamma q^2}, \quad (3.5)$$

where γ is the interfacial tension. Transforming this back into real space by integrating over all possible modes $\mathbf{q} = [q_{\min}, q_{\min}]^5$ we find an expression for the mean-squared interfacial width w^2 (Weeks, 1977),

$$w^2 = \langle h(\mathbf{r})^2 \rangle = \frac{k_B T}{2\pi\gamma} \ln \frac{L}{l}, \quad (3.6)$$

5. $q_{\min} = 2\pi/L$ is set by the lateral system size L (and therefore the longest wavelength) and $q_{\max} = 2\pi/l$ is a required cutoff above the microscopic length scale.

where l is the bulk correlation length. Therefore, in the thermodynamic limit $L \rightarrow \infty$, w diverges – very weakly, since w grows with $\ln L$. In the presence of gravitation with strength g , the height-height correlation $\langle |h(\mathbf{q})|^2 \rangle$ yields (Weeks, 1984)

$$\langle |h(\mathbf{q})|^2 \rangle = \frac{k_B T}{\gamma(\mathbf{q}^2 + \xi_g^{-2})}, \quad (3.7)$$

where ξ_g is the correlation length in lateral dimension, or *capillary length* and measures the range of the correlations along the interface. It is given by

$$\xi_g = \sqrt{\frac{\gamma}{\Delta m g}}, \quad (3.8)$$

where Δm is the difference in the magnetizations of the coexisting phases $\Delta m = m_+ - m_-$. The real-space transformation the height fluctuation spectrum from Eq. (3.7) reads

$$\langle h^2(\mathbf{r}) \rangle = \frac{k_B T}{2\pi\gamma} \ln \left(\frac{\xi_g}{l} \right). \quad (3.9)$$

If the system size $L \gg \xi_g$, the width $w = \sqrt{\langle h^2(\mathbf{r}) \rangle}$ is dominated and limited by the gravitation and even when $L \rightarrow \infty$.

Therefore, in finite systems we can assign a width w to the interface located around x_0 , which is typically determined from a $\tanh(x)$ -fit of the form

$$m(x) = \frac{m_+ + m_-}{2} - \frac{m_+ - m_-}{2} \tanh \left(\frac{x - x_0}{2w} \right), \quad (3.10)$$

where the interface is perpendicular to the x -axis and m_{\pm} are the respective magnetizations of the system on the binodal line (cf. Figure 3.2). The above equation can be applied also for asymmetric cases where $m_+ \neq -m_-$. w is dependent on the lateral size of the interface, temperature and the interaction strength J . Although the shape of the interface profile described by Eq. (3.10) is actually a result from mean field theory, which is only valid in the critical region, the hyperbolic tangent fit is useful to determine an effective interface width w from density profiles (Rozas and Horbach, 2011).

Approaching the critical temperature T_c from a temperature below T_c , w will grow and finally diverge (this will be explained in the next section), resulting in the absence of an interface. This can be seen in Figure 3.3: While at temperatures far away from criticality the interface is well-defined, close to T_c it becomes increasingly difficult to determine the location of an interface.

Further, an interface formation implies a free energy cost, which in turn means there is an interfacial tension⁶. In the Ising ferromagnet the free energy cost contributes from neighboring spins of opposite sign. While in the thermodynamic limit this contribution vanishes, there is a finite contribution in the two-phase region.

6. The interfacial surface tension has the dimension of energy per unit area or equivalently, force per unit length.

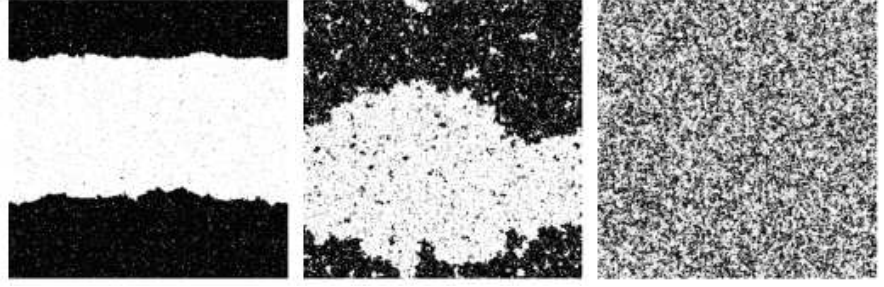


Figure 3.3: Example snapshots of the two-dimensional square lattice Ising model at $k_B T/J = 1.66, 2.2, 3.0$ (from left to right) as determined from computer simulations with no external field applied. Black/white color indicate the spin values $s = \pm 1$. Periodic boundary conditions have been applied and a magnetization around $m = 0$ was enforced for $T < T_c$. The critical point in this model is at $k_B T_c/J = 2/\ln(1 + \sqrt{2}) \approx 2.269$.

3.1.1 The critical point and critical phenomena

One ansatz to describe the behavior of the Ising model close to the critical point at zero field is mean field theory. Within this model, each spin s_i is replaced by the average magnetic field m plus a small fluctuation δs_i (Tuckerman, 2010):

$$s_i \rightarrow m + \delta s_i, \quad (3.11)$$

therefore $s_i s_j$ can be rewritten as:

$$\begin{aligned} s_i s_j &= (m + \delta s_i)(m + \delta s_j) \\ &= m^2 + m(\underbrace{\delta s_i + \delta s_j}_{=s_i - m}) + \delta s_i \delta s_j \\ &= -m^2 + m(s_i + s_j) + \delta s_i \delta s_j. \end{aligned} \quad (3.12)$$

Within the mean-field approximation, fluctuations are considered small and the term $\delta s_i \delta s_j$ is dropped. Inserting Eq. (3.12) into Eq. (3.1) yields the mean-field Hamiltonian for the Ising model:

$$\begin{aligned} \mathcal{H}_{\text{Ising, MF}} &= -J \sum_{\langle i,j \rangle} (-m^2 + m(s_i + s_j)) + H \sum_i s_i \\ &= \frac{1}{2} N J m^2 - (H + J m) \sum_i s_i \end{aligned} \quad (3.13)$$

for N spins. The result in Eq. (3.13) is the same as for an ideal (noninteracting spins) paramagnet in an effective field:

$$\mathcal{H}_{\text{eff}} = H + J m. \quad (3.14)$$

We then obtain a self-consistent equation for the magnetization of each spin experiencing this effective field,

$$m = \langle s \rangle = \frac{\sum_i s_i e^{\beta \mathcal{H}_{\text{eff}} s_i}}{\sum_i e^{\beta \mathcal{H}_{\text{eff}} s_i}} = \frac{e^{\beta \mathcal{H}_{\text{eff}}} - e^{-\beta \mathcal{H}_{\text{eff}}}}{e^{\beta \mathcal{H}_{\text{eff}}} + e^{-\beta \mathcal{H}_{\text{eff}}}} \quad (3.15)$$

$$= \tanh[\beta(Jm + H)], \quad (3.16)$$

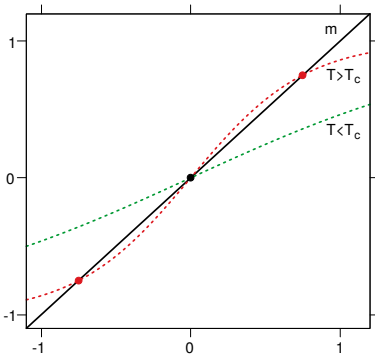


Figure 3.4: By plotting m (straight line) and $\tanh(\beta J m)$ (dotted lines) in the same graph, one can read off the solutions (the intersection between both curves) from the self-consistent equation of the mean-field approximation of the two-dimensional Ising model. For $1/\beta = k_B T > k_B T_c$ one a single solution $m = 0$ exists. For $T < T_c$, three solutions can be found.

which can be solved numerically, or graphically as shown in Figure 3.4. For $T > T_c$ there is only the paramagnetic solution, $m = 0$ – but for lower temperatures we have two, $\pm|m|$. We can find them by expanding Eq. (3.15) in the field free case $H = 0$ and assuming that $m \ll 1$ holds close to the critical point

$$m = \tanh(\beta J m) = \beta J m - \frac{1}{3}(\beta J)^3 m^3 + \mathcal{O}(m^5) . \quad (3.17)$$

At the critical point we have $\beta_c J = J/(k_B T_c) = 1$ and dropping the higher order terms $\mathcal{O}(m^5)$ yields

$$1 = \frac{T_c}{T} - \frac{1}{3} \left(\frac{T_c}{T} \right)^3 m^2 , \quad (3.18)$$

with the solutions

$$m = \pm \sqrt{3} \left(\frac{T}{T_c} \right)^{3/2} \left(\frac{T_c - T}{T_c} \right)^{1/2} , \quad (3.19)$$

which behaves as (the β used here is *not* the inverse temperature)⁷

$$m \propto (T - T_c)^\beta \quad \text{with} \quad \beta = 1/2 . \quad (3.20)$$

Similarly, the magnetic susceptibility $\chi = \frac{\partial m}{\partial H}|_T$, describing the variance of the magnetization has an analogous behavior at the critical point

$$\chi \propto |T - T_c|^{-\gamma} \quad \text{with} \quad \gamma = 1 , \quad (3.21)$$

thus fluctuations become singular at the critical point. A quantity closely related to χ which is of importance in phase transitions is the correlation length ξ , in the Ising model it measures the length scale of correlations between fluctuations $\Delta s_i = s_i - \langle s_i \rangle$ of spins s_i :

$$\langle (s_i - \langle s_i \rangle)(s_j - \langle s_j \rangle) \rangle = e^{-|d_{ij}|/\xi} , \quad (3.22)$$

where d_{ij} is the distance between the spins i and j . The characteristic length scale on which such correlations decay, ξ is called the correlation length. It can be understood as the linear dimension of the “typical” cluster size of regions with same magnetization. Consider a single spin flipping at a certain position, the correlation length then measures the distance where the probability of other spins also flipping are affected by this flip and it can be shown to scale within the framework of mean field theory like

$$\xi \propto \left| \frac{T - T_c}{T_c} \right|^{-\nu} \quad \text{with} \quad \nu = 1/2 . \quad (3.23)$$

As fluctuations grow with the increase of the correlation length, the interface width separating the two phases will grow, too. Within mean-field theory the interface between the two phases has a profile which can be expressed as (Cahn and Hilliard, 1958; Fisk and Widom, 1969)

$$m(x) = m_+ \tanh \left(\frac{x}{2w} \right) , \quad (3.24)$$

7. And it should be clear from the context. The unit of the inverse temperature $1/k_B T = \text{Energy}^{-1}$, while the scaling exponent is dimensionless.

with the assumption of an intrinsic width w . This width w is proportional to the correlation length ξ , and scales near the critical point accordingly. Consequently, the width diverges with the exponent ν , too.

From Eqs. (3.23) and (3.21) we find that fluctuations become increasingly important as criticality is approached, while the mean-field model is able to predict the qualitative phase behavior, it fails quantitatively in systems of low (< 4) dimensions, as shown in Table 3.1. The

| Quantity | Exponent | MFT | Ising | |
|-----------------------------------|----------|-----|-------|-------|
| | | | 2D | 3D |
| $\tau \equiv T - T_c /T_c$ | | | | |
| specific heat, $\tau^{-\alpha}$ | α | 0 | 0 | 0.125 |
| order parameter, τ^β | β | 0.5 | 0.125 | 0.326 |
| susceptibility, $\tau^{-\gamma}$ | γ | 1 | 1.75 | 1.25 |
| correlation length, $\tau^{-\nu}$ | ν | 0.5 | 1 | 0.630 |

Table 3.1: Incomplete list of critical exponents for different universality classes, where quantities show a power-law behavior of $x \propto (T - T_c)^y$ close to the critical temperature T_c , with y as critical exponent. Values for mean-field theory (MFT) and two-dimensional (2D) Ising models are exact, while critical exponents from in 3-dimensional (3D) Ising universality class are determined from numerical models. Parameters were taken from [Pelissetto and Vicari, \(2002\)](#).

reason for the failure of the correct prediction of the scaling behavior is due to the large fluctuations and the initial assumption of the mean field theory does not hold anymore. A diverging correlation length means that all length scales become important, and at dimensions smaller than 4, the mean field theory gives wrong quantitative results. Nevertheless, it is remarkable that such a simple model predicts correct qualitative behavior with regard to power-law scaling in phase transitions.

3.2 From the Ising model to simple fluids

In the previous section we explained that at the critical point one observes scale-invariant behavior due to the divergence in the correlation length. This means, on the other hand, that the very local, microscopic details of the particle interaction become unimportant at the critical point and the same scaling behavior can be found in other systems. In the Ising model there are spins, up and down, which interact only with the nearest neighbors and their preferred orientation (depending on the temperature) can be influenced by the external field H .

Let us now consider a classical gas of N particles in a system with volume V interacting attractively with each other. We divide our total volume into N_{cell} small sub-volumes v in such a way that each v can be occupied by a single particle only (but move freely around) and particles are allowed to interact with nearest-neighbor cells. The fraction of occupied sub volumes x is given by

$$x = \frac{N}{V/v} = \frac{N}{N_{\text{cell}}}. \quad (3.25)$$

This model is known as the *lattice gas model* (C. N. Yang and Lee, 1952; Lee and C. N. Yang, 1952) and even though it describes a fluid, its relation to the Ising model is easily noticeable (and mathematically equivalent). An occupied cell corresponds to a spin up (\uparrow) and vacant sites to spin down (\downarrow), other quantities can be related between the two models, as shown in Table 3.2. Even though expressed via different

| Ising model | Lattice gas |
|-----------------------------|-------------------------------------------|
| No. of spins | volume V |
| No. of spins \uparrow | No. of atoms N |
| Magnetization m | Avg. volume occupied by atoms |
| External magnetic field H | Chemical potential difference $\Delta\mu$ |
| Free energy per spin | Pressure P |

Table 3.2: Relationships between corresponding quantities of lattice gas and Ising model.

quantities, phase transitions in the lattice gas will look very similar compared to the Ising model (cf. Figure 3.3). Above the critical temperature T_c , only homogeneous phases can be observed and the local density $\chi(\delta V)$ of a block δV (larger than v) will be identical to the total average of $\chi(V)$. At temperatures far below T_c phase separation occurs and macroscopic phases of two different fractions of occupied cells emerge, a gas and a liquid phase with $\chi = \chi_{\text{gas}}$ and χ_{liquid} , respectively. These phases will be separated by an interface. At the critical point, the correlation length grows and clusters of occupied and vacant regions appear, and fluctuations of $\chi(\delta V)$ increase and the local density will deviate strongly from the mean value of $\chi(V)$. Thus, the lattice gas is thermodynamically equivalent to the Ising model.

Extending the lattice gas model further to effectively describe noble gases, the liquid–gas transition is qualitatively (by the means of critical scaling) identical to 3D-Ising universal behavior. This close relation between the Ising model and simple fluids is one of the reasons why the Ising model has become so valuable in statistical mechanics. As long as two systems belong to the same universality class, an Ising ferromagnet (may it be two- or three-dimensional) behaves identical (by the means of scaling) to in the vicinity of the critical point.

3.3 Phase transitions in confinement

Introducing geometrical confinement (for example walls, thin film geometries, or in porous media) to systems undergoing a phase transition, have been known to induce exciting phase behavior unknown from bulk phases (Dietrich, 1999; Gelb, Gubbins, Radhakrishnan, and Sliwinska-Bartkowiak, 2000).

One extensively studied example are thin films geometries. There, the fluid is confined by two attractive parallel walls separated by a distance D as sketched in Figure 3.5. A vapor–liquid phase transition is still present, but it is modified compared to the bulk transition.

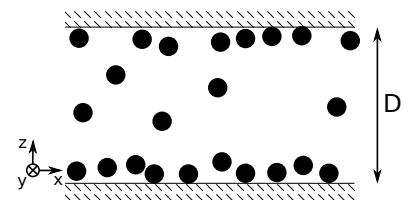


Figure 3.5: A fluid confined in a thin film geometry with attractive walls. Particles can move freely in x and y directions, but are limited in z to $[0; D]$.

Depending on the thickness D of the slit, the critical temperature and coexistence pressure is lowered with varying wall distance D . Figure 3.6 illustrates this for the analogue Ising system. This process is called *capillary condensation*. Close to the critical point, with the growth

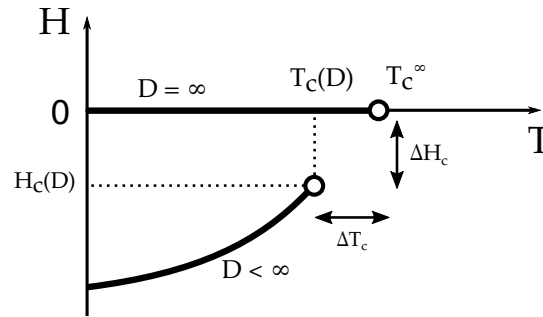


Figure 3.6: Schematic of the shift in the coexistence curve and critical point induced by a thin film geometry of thickness D . Redrawn from [Binder, D. P. Landau, and M. Müller, \(2003\)](#).

of the correlation length, ξ becomes larger than D and a gradual cross-over scaling from three- to two dimensional universality takes place ([Binder and D. P. Landau, 1992](#)) as the correlation length is not limited in x and y direction. Similar phenomena also exist in confined cylindrical pores, as present in various porous materials, where the correlation length is bounded by the pore diameter. The lateral dimension, however is much larger, thus the fluid gains a one-dimensional character ([Wilms, Winkler, Virnau, and Binder, 2010](#)).

Slit pore confinements have been extensively studied in experiments and with computer simulation models of colloid-polymer suspensions ([Binder, Horbach, Vink, and De Virgiliis, 2008](#); [Aarts and Lekkerkerker, 2004](#)). Such suspensions are experimentally easier to study due to their large particle size (of the order of $\approx 1 \mu\text{m}$), so the phase behavior and interface phenomena can be investigated using laser scanning microscopy as shown in Figure 3.7. In these

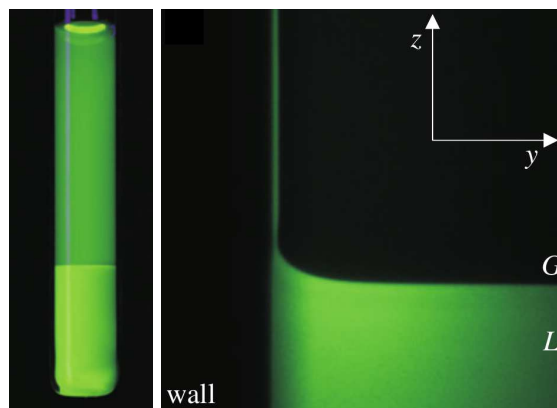


Figure 3.7: Interface between gas (G) and liquid (L) phases close to a hard wall, as determined from experiment using laser scanning microscopy. From [Aarts and Lekkerkerker, \(2004\)](#).

mixtures, the colloid-rich phase correspond to the liquid phase and

the polymer-rich phase to the vapor phase. When confined by hard walls, a meniscus occurs between the coexisting phases (see Figure 3.7 and from computer simulation in Figure 3.8).

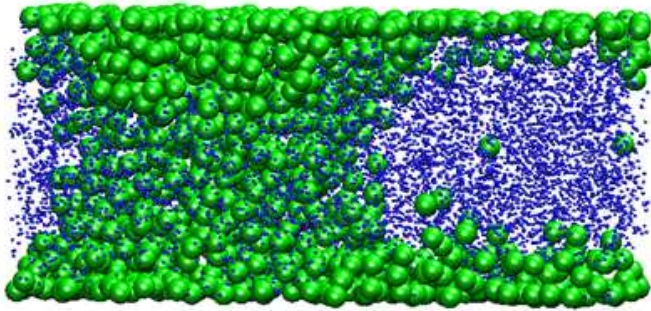


Figure 3.8: Simulation snapshot of a model colloid-polymer mixture at coexistence condition of polymer and colloid-rich phases. From [Vink, De Virgiliis, Horbach, and Binder, \(2006\)](#).

In another system, where the wall substrate is subject to an inhomogeneous pattern of hydrophilic and hydrophobic areas, as studied by [Lenz and Lipowsky, \(1998\)](#) and [Gau, Herminghaus, Lenz, and Lipowsky, \(1999\)](#), wetting layers of different morphologies can form on the substrate, depending on the droplet volume. Water droplets can form heterogeneous patterns on the substrate domains as shown in Figure 3.9. With increasing adsorbed volume the adsorption pattern undergoes a transition from partial to full wetting of the surface. Modifying the pattern to include edges introduces additional effects, as there is a preferred enrichment of water at the kinks, as shown in Figure 3.9b.

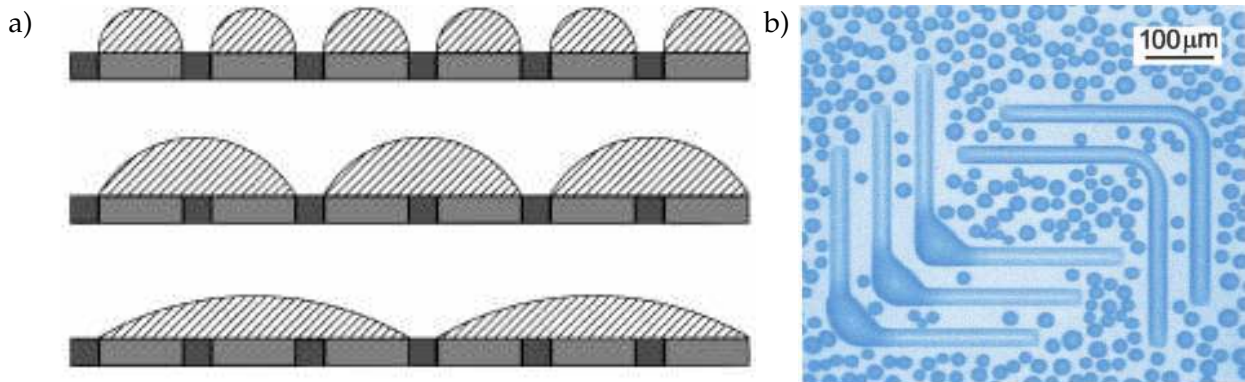


Figure 3.9: a) Depending on the adsorbed volume, the striped pattern of the hydrophobic surface promotes different droplet phases. Results from experiments with water adsorbed on a pattern with kinked hydrophilic stripes are shown in b). From [Lenz and Lipowsky, \(1998\)](#) and [Gau, Herminghaus, Lenz, and Lipowsky, \(1999\)](#).

Now, metal-organic frameworks combine some properties explained above, it introduces a confinement given by the framework. Yet, this structure is much more open, so one can expect fluids to behave differently compared to capillary condensation as observed

in many porous materials. The character (i.e. universality class) of phase transitions in this medium is not obvious and could depend on multiple properties of the MOF, e.g. pore size, interaction strength, mobility of guest molecules in the MOF and so forth.

Another feature in MOFs is the heterogeneity of the interaction of the MOF with the fluid. The metallic clusters at the framework corners are known to interact stronger (i.e. more attractive) with guest molecules (Walton and Snurr, 2007), as illustrated in Figure 3.10. At very low pressures only the corners are covered (point A in Figure 3.10 and with increasing pressure a wetting layer covers the whole framework (B and C) until at very high pressures the pore is filled with liquid completely (D). Still, it remains unclear whether the transi-

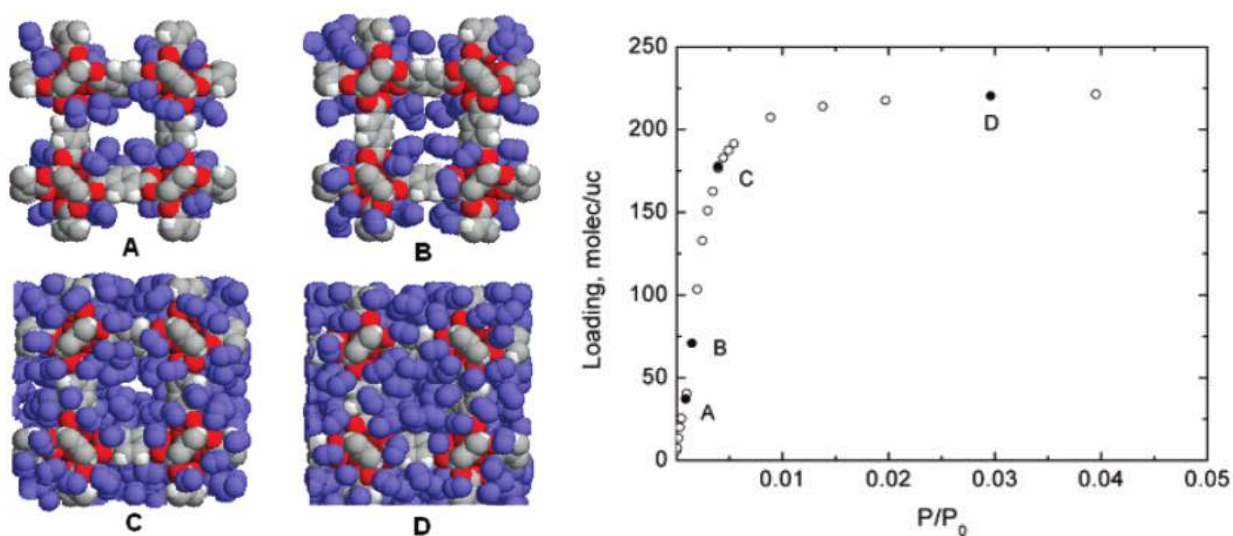


Figure 3.10: Snapshots from computer simulations of the adsorption of Nitrogen in IRMOF-1 at 77 K. Labels A-D correspond to the pressure as marked in the adsorption isotherm. From Walton and Snurr, (2007).

tion between the different state points A-D is associated with one or more thermodynamic phase transitions with critical points and which universal scaling applies there.

The aim of this work is to elucidate the phase behavior of methane in the prototypical MOF, IRMOF-1, and its close relatives IRMOF-8 and -16 and try to understand the role of the heterogeneous interaction of the framework with its guest particles. Patterned wetting layers analogous to the two-dimensional pattern on substrates are imaginable – with the important difference that MOFs are, of course three-dimensional. If there is more than a liquid–vapor like phase transition in MOFs, a structural analysis will follow. With the methods introduced in the following chapter we will analyze the critical behavior and compare it with the confinements mentioned in this chapter. Further, as the mobility and diffusion of particles in IRMOFs plays an important role for industrial use (Stallmach, Gröger, et al., 2006), the adsorption kinetics (also with respect to possible phase transitions in the MOF) must be understood in more detail – also in conjunction with the bulk phase behavior of the fluid.

METHODS

This chapter gives an introduction into the applied methods required to calculate the phase diagram of methane in MOFs. As purely analytical methods often fail in more complicated systems with many particles, numerical methods are applied to investigate the phase behavior and adsorption kinetics in metal–organic frameworks.

4

4.1 Computer Simulations

Pioneered by the work of *von Neumann and Goldstine, (1947)*, computers have become the most valuable tool for numerical calculations. They have long outperformed humans on doing repetitive, identical work. Still, there are numerous numerical methods and algorithms, depending on the problem that needs to be solved. In physics, many of the methods originate from the Manhattan Project in the 40's and 50's of the 20th century. While computer simulations span a wide field of methods and strategies, the focus in this work is on particle based computer simulations. This means each particle will be handled individually and the only input into the simulations is the interaction potential, no further assumptions about the substances is required. The most simple systems are models of hard spheres, which have an infinite repulsion below a certain distance (its behavior is similar to steel balls without the influence of an external field, i.e. gravity). For the description of noble gases the Lennard-Jones (LJ) model has proven to work well – also for other spherical uncharged molecules, such as methane. Lennard-Jones particles have a short-ranged repulsion, caused by the Pauli repulsion of the electrons while at larger distances there is an attraction originating in van-der-Waals forces.

In the following interaction models used in the simulations to model metal–organic frameworks and methane are presented as well as the methods, namely grand canonical Monte Carlo and molecular dynamics simulations.

4.2 Modeling Methane and Metal–Organic Frameworks

From a computational point of view methane has some advantages over other molecules as CO₂, H₂, or polymers. It is almost spherical (reducing the translational degrees of freedom), it has no dipole (so long-ranged electrostatic interaction can be omitted) and it can be

described by the means of classical mechanics in the targeted temperature range of 30 – 300 K. The united atom model (i.e. describing methane as a single spherical particle instead of considering each atom separately) follows the work of [Smit, Karaborni, and Siepmann, \(1995\)](#), approximating CH₄ by a cut-off and shifted Lennard-Jones interaction potential $u(r)$:

$$u_{\text{LJ}}(r) = 4\epsilon_{\alpha\beta} \left[\left(\frac{\sigma_{\alpha\beta}}{r} \right)^{12} - \left(\frac{\sigma_{\alpha\beta}}{r} \right)^6 \right]$$

$$u(r) = \begin{cases} u_{\text{LJ}}(r) - u_{\text{LJ}}(r_c) & \text{if } r \leq r_c \\ 0 & \text{otherwise} \end{cases}, \quad (4.1)$$

where r is the distance between particle centers, $\epsilon_{\alpha\beta}$ the depth of the potential, and $\sigma_{\alpha\beta}$ the effective diameter of this interaction. r_c is the cut-off distance.

Similarly, Metal–Organic Frameworks (MOFs) are described by an atomistic particle model, i.e. each atom of the framework will interact separately with the guest particles¹. To determine $\epsilon_{\alpha\beta}$ and $\sigma_{\alpha\beta}$, Lorentz-Berthelot mixing rules² are applied. The potential parameters for the framework atoms based on the van-der-Waals parameters of the Unified-Force-Field (UFF) as described in [Rappé and Casewit, \(1992\)](#) and are listed in Table 4.1. The cut off radius r_c is $2.5\sigma_{\text{CH}_4}$ for guest-guest interactions and in the case of guest-host $r_c^{\alpha\beta} = 3.43\sigma_{\alpha\beta}$. Further,

1. Also known as *all-atom* models as each atom is simulated individually.

2. Lorentz-Berthelot mixing rules for two particle types α and β are defined as

$$\epsilon_{\alpha\beta} = \sqrt{\epsilon_{\alpha}\epsilon_{\beta}},$$

$$\sigma_{\alpha\beta} = \frac{\sigma_{\alpha} + \sigma_{\beta}}{2}.$$

Original works by [Lorentz, \(1881\)](#) and [Berthelot, \(1898\)](#).

| Particle | ϵ/k_B (K) (original work) | ϵ/k_B (K) (this work) | σ (Å) |
|----------------------------|---------------------------------------|-----------------------------------|--------------|
| Methane (CH ₄) | 148.0 | 175.9 | 3.73 |
| Carbon (C) | 52.84 | 62.81 | 3.43 |
| Hydrogen (H) | 22.14 | 26.31 | 2.57 |
| Oxygen (O) | 30.19 | 35.88 | 3.12 |
| Zinc (Zn) | 62.40 | 74.17 | 2.46 |

Table 4.1: Lennard-Jones parameters of methane and the framework atoms. The constant factor multiplied to ϵ is introduced in order to shift the critical point of bulk methane to the experimentally obtained value. For details, see text.

all framework atoms will be fixed at their positions, so flexibility of the MOF structure is not taken into account.

This model has been used in other works determining adsorption isotherms from computer simulations and the results match experimental values quite accurately ([Düren, Sarkisov, Yaghi, and Snurr, 2004](#)).

4.2.1 Grid-interpolation for MOF-Methane interaction

As noted above, the framework atoms are on fixed positions, which allows for pretabulation of the potential energy landscape (and its derivatives) on a three-dimensional lattice. These lattice points are used with a 3-D cubic Hermite spline interpolation ([Schultz, 1973](#)) for a faster computation of the guest-host interaction in the porous

medium. This method has the advantage that it works very nicely with periodic boundary conditions even with asymmetric unit cells and has been well tested for modeling methane in silicates (June, Bell, and Theodorou, 1990) and has also been used in computational studies for MOFs (Skoulidas and Sholl, 2002).

The idea of Hermite splines can be explained in the one-dimensional case most easily and is as follows: Consider a segment on points, at x_0 and x_1 with their respective function values y_1 and y_2 called *knots*. Mapping the distance between x_1 and x_2 to a unit interval

$$x_r = \frac{x - x_1}{x_2 - x_1} \quad \text{with } x_2 > x_1 \text{ and } x_r \in [0, 1], \quad (4.2)$$

we can introduce a third order polynomial $\tilde{f}(x_r)$ which goes through $f(x_1)$ and $f(x_2)$ with the same derivatives $\partial_x f(x_{1,2})$ at $x_{1,2}$ (Schultz, 1973):

$$\begin{aligned} \tilde{f}(x_r) = & [2f(x_0) - 2f(x_1) + \partial_x f(x_0) + \partial_x f(x_1)] x_r^3 \\ & + [-3f(x_0) + 3f(x_1) - 2\partial_x f(x_0) - \partial_x f(x_1)] x_r^2 \\ & + \partial_x f(x_0)x_r + x_0, \end{aligned} \quad (4.3)$$

which can be rewritten in terms of helper functions $h_i^j(x_r)$,

$$\begin{aligned} h_0^1(x) &= x^2(3 - 2x) \\ h_0^0(x) &= (1 + 2x)(1 - x)^2 = h_0^1(1 - x) \\ h_1^1(x, d) &= dx^2(x - 1) \\ h_1^0(x, d) &= h_1^1(1 - x, -d) \end{aligned} \quad (4.4)$$

yielding

$$\begin{aligned} \tilde{f}(x) &= h_0^0(x_r)f(x_0) + h_1^0(x_r, \Delta x)\partial_x f(x_0) \\ &+ h_0^1(x_r)f(x_1) + h_1^1(x_r, \Delta x)\partial_x f(x_1) \\ &= \sum_{i=0}^1 h_0^i(x_r)f(x_i) + h_1^i(x_r, \Delta x)\partial_x f(x_i), \end{aligned} \quad (4.5)$$

where $\Delta x = x_2 - x_1$. By combining all intervals, one obtains a smooth continuous function, which is quite useful if one interpolates the potential energy, the first derivative (the force) will be continuous, too. The above scheme in Eq. (4.5) can be easily extended to two and three dimensions by subsequently application of the same interpolation into y and z direction. In two dimensions, there are then four nearest knots and the interpolated function $\tilde{f}(x, y)$ reads

$$\begin{aligned} \tilde{f}(x, y) &= \sum_{j=0}^1 \left(\left[\sum_{i=0}^1 h_0^i(x_r)f(x_i, y_j) + h_1^i(x_r, \Delta x)\partial_x f(x_i, y_j) \right] h_0^j(y_r) \right. \\ &+ \left. \left[\sum_{i=0}^1 \partial_y h_0^i(x_r)f(x_i, y_j) + \partial_y h_1^i(x_r, \Delta x)\partial_x f(x_i, y_j) \right] h_1^j(y_r, \Delta y) \right) \\ &= \sum_{j=0}^1 \sum_{i=0}^1 \left[h_0^i(x_r)h_0^j(y_r)f(x_i, y_j) + h_1^i(x_r, \Delta x)h_0^j(y_r)\partial_x f(x_i, y_j) \right. \\ &+ \left. h_0^i(x_r)h_1^j(y_r, \Delta y)\partial_y f(x_i, y_j) + h_1^i(x_r, \Delta x)h_1^j(y_r, \Delta y)\partial_x \partial_y f(x_i, y_j) \right]. \end{aligned} \quad (4.6)$$

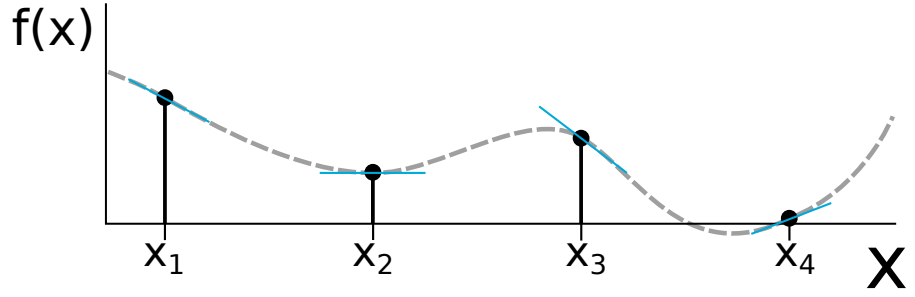


Figure 4.1: Illustration for one-dimensional Hermite-Splines. The function values and derivatives (indicated in blue) of two neighboring points (knots), x_1 and x_2 are used for a piecewise interpolation between these points. Repeating the procedure for all intervals gives an interpolation over the full range (dashed line).

In three dimensions, we 8 neighbors are required and interpolation equation includes 64 terms:

$$\begin{aligned}
 \tilde{f}(x, y, z) = & \sum_{k=0}^1 \sum_{j=0}^1 \sum_{i=0}^1 \left[h_0^i(z_r) h_0^i(x_r) h_0^j(y_r) h_0^k(z_r) f(x_i, y_j, z_k) \right. \\
 & + h_1^i(x_r, \Delta x) h_0^j(y_r) h_0^k(z_r) \partial_x f(x_i, y_j, z_k) \\
 & + h_0^i(x_r) h_1^j(y_r, \Delta y) h_0^k(z_r) \partial_y f(x_i, y_j, z_k) \\
 & + h_0^i(x_r) h_0^j(y_r) h_1^k(z_r, \Delta z) \partial_z f(x_i, y_j, z_k) \\
 & + h_1^i(x_r, \Delta x) h_1^j(y_r, \Delta y) h_0^k(z_r) \partial_x \partial_y f(x_i, y_j, z_k) \\
 & + h_1^i(x_r, \Delta x) h_0^j(y_r) h_1^k(z_r, \Delta z) \partial_x \partial_z f(x_i, y_j, z_k) \\
 & + h_0^i(x_r) h_1^j(y_r, \Delta y) h_1^k(z_r, \Delta z) \partial_y \partial_z f(x_i, y_j, z_k) \\
 & \left. + h_1^i(x_r, \Delta x) h_1^j(y_r, \Delta y) h_1^k(z_r, \Delta z) \partial_x \partial_y \partial_z f(x_i, y_j, z_k) \right]. \tag{4.7}
 \end{aligned}$$

In our computer simulations, where an interpolation of the potential energy landscape $U(\mathbf{r})$ of a methane particle with the MOF atoms is required, this spline interpolation scheme has the advantage of being constant in time, independent of the number of interacting particles, since those are hidden in the knots and its derivatives – which are calculated only once. In this work we use a periodic grid with a spacing of $\approx 3 \text{ \AA}$ between neighboring knots. In a three dimensional system, each knot requires 8 coefficients, thus for IRMOF-1 (with 130 knots on each edge) there are 1.75×10^7 coefficients. With double precision (8 Byte per value) the total memory required for holding the coefficients is $\approx 134 \text{ MB}$.

4.3 Monte Carlo simulations

3. As explained in [Metropolis, \(1987\)](#), Metropolis suggested the name because the uncle of Stanislaw Ulam, used to borrow money from his relatives, because he “had to go to Monte Carlo”.

Named after the casino in Monaco³, *Monte Carlo* simulations are generating a vast amount of random numbers and connecting these to physical variables in order to sample a large number of states in the thermodynamic system. Using sophisticated sampling techniques, it allows for accessing equilibrium properties of the analyzed model.

Probably the most used introductory example for Monte Carlo methods is the following: Consider the estimation of π using the area of a circle with radius d surrounded by a square with an edge length d , as shown in Figure 4.2. The ratio of both areas is given by

$$\frac{\text{area of circle}}{\text{area of square}} = \frac{\pi}{4} \quad (4.8)$$

and can be approximated numerically by choosing two random numbers of uniform distribution in the range of $[-d; d]$ defining a random point in the square. By counting all “hits” into the circle n_{circ} , the approximated value of π can be calculated by $4n_{\text{circ}}/n_{\text{trial}}$ after n_{trial} total tries. This rather intuitive strategy is called *direct sampling* and can be modified in the following manner: Instead of choosing a random position in each step, a displacement $\Delta = (\delta x, \delta y)$, is sampled using random numbers with $\delta x, \delta y = \text{rand}(-a, a)$, where $\text{rand}(-a, a)$ returns a random number in the range $[-a, a]$. Starting from an arbitrary position (this could be at the center of the circle), we propagate through the whole space and count the number of hits in the circle analogously to the previous method. As any n th step only depends on the previous step $n - 1$, this process is “memoryless”⁴, and the whole process becomes a *Markov chain*. However, this strategy has the following problem: What happens when the new position would leave the square (cf. step $(k) \rightarrow (k + 1)$ in Figure 4.3)?

Assuming the system is in equilibrium and the transition probability between two states $p(\cdot \rightarrow \cdot)$ is known, the following equation, *detailed balance*, holds⁵:

$$f(\text{old}) p(\text{old} \rightarrow \text{new}) = f(\text{new}) p(\text{new} \rightarrow \text{old}) , \quad (4.9)$$

where $f(\cdot)$ is the stationary (equilibrium) probability of finding the system in a certain state. It means that the probability of being in a state *old* and transitioning into another state *new*, must be equal to the stationary probability of *old* and moving to state *new*. In a Markov chain, $p(\text{old} \rightarrow \text{new})$ can be rewritten as

$$p(\text{old} \rightarrow \text{new}) = \mathcal{A}(\text{old} \rightarrow \text{new}) \text{acc}(\text{old} \rightarrow \text{new}) , \quad (4.10)$$

where $\text{acc}(\cdot, \cdot)$ is the acceptance probability and $\mathcal{A}(\text{old} \rightarrow \text{new})$ denotes the “a priori probability”.

Using Eq. (4.10) and assuming that \mathcal{A} is symmetrical, i.e. $\mathcal{A}(\text{old} \rightarrow \text{new}) = \mathcal{A}(\text{new} \rightarrow \text{old})$, the Metropolis criterion (see [Metropolis, Rosenbluth, et al., \(1953\)](#)) can be used to satisfy detailed balance⁶:

$$\text{acc}(\text{old} \rightarrow \text{new}) = \min \left(1, \frac{f(\text{new})}{f(\text{old})} \right) . \quad (4.11)$$

This rule for the acceptance probability can be used to determine whether consecutive steps will be accepted and a move takes place or if the step is rejected and the current value will be reused.

With this criterion it is possible to solve the above problem: If the new position is outside the allowed box, therefore the probability of being

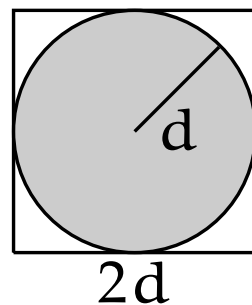


Figure 4.2: Illustration for the estimation of π : The ratio of the areas $A_{\text{circle}}/A_{\text{square}}$ is equal $\frac{\pi}{4}$. This ratio be estimated numerically by choosing n_{tot} random positions and counting how many of the total trials (n_{trial}) where in the circle (gray area). Then $\frac{4n_{\text{circ}}}{n_{\text{trial}}}$ gives an estimate for π .

4. Processes with no memory are processes where the future depends on the present, only – the history plays no role.

5. A derivation of detailed balance can be found in [Allen and Tildesley, \(1989\)](#).

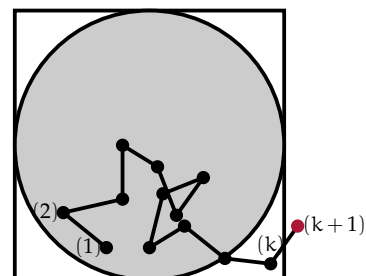


Figure 4.3: Modification for direct sampling: Markov chains. Consequent steps i only depend on the previous step $i - 1$, i.e. no “memory” is retained and a random walk takes place. For an explanation about the step $(k) \rightarrow (k + 1)$, see text.

6. The generalized case, where \mathcal{A} is asymmetrical, has been discussed by [Hastings, \(1970\)](#).

in that state is zero and $f(\text{new}) = 0$. Consequently, this displacement move is rejected, step (k) will be counted again and serves as a starting point for the next trial.

Now, if we extend the problem to the sampling in thermodynamic systems, we want to determine the average of a quantity A . In the canonical ensemble such an average reads

$$\langle A \rangle = \frac{\int d\mathbf{r}^N A(\mathbf{r}^N) \exp[-U(\mathbf{r}^N)/k_B T]}{\int d\mathbf{r}^N \exp(-U(\mathbf{r}^N)/k_B T)}, \quad (4.12)$$

where $\mathbf{r}^N = \{\mathbf{r}_1, \mathbf{r}_2, \dots, \mathbf{r}_N\}$ is a microscopic state of N particles at a given temperature T . $U(\mathbf{r}^N)$ is the inner energy at such state. The term $\exp[-U(\mathbf{r}^N)/k_B T]$ from Eq. (4.12) is an extremely sharp distribution where only an exponentially small fraction of states actually contribute to $\langle A \rangle$. Thus, with simple sampling, where the states are chosen homogeneously from the phase space, one would have mostly states from the tail of the distribution – which is very ineffective and determining an accurate value for $\langle A \rangle$ becomes impossible. Instead, we introduce a probability weight p to each phase space contribution, such that the exponential cancels out,

$$\langle A \rangle = \frac{\int d\mathbf{r}^N A(\mathbf{r}^N) \exp[-U(\mathbf{r}^N)/k_B T] / p(\mathbf{r}^N)}{\int d\mathbf{r}^N \exp(-U(\mathbf{r}^N)/k_B T) / p(\mathbf{r}^N)} \quad (4.13)$$

choosing $p(\mathbf{r}^N) = \exp(-U(\mathbf{r}^N)/k_B T)$ simplifies $\langle A \rangle$ to an arithmetic average:

$$\langle A \rangle = \frac{1}{N} \sum_{i=1}^N A_i(\mathbf{r}^N). \quad (4.14)$$

Obeying detailed balance from Eq. (4.9),

$$\begin{aligned} \frac{p(\text{old} \rightarrow \text{new})}{p(\text{new} \rightarrow \text{old})} &= \exp\left\{ \frac{[U(\mathbf{r}_{\text{new}}^N) - U(\mathbf{r}_{\text{old}}^N)]}{k_B T} \right\} \\ &\equiv \exp[-\Delta U / k_B T], \end{aligned} \quad (4.15)$$

the Metropolis criterion reads

$$\text{acc}(\text{old} \rightarrow \text{new}) = \min(1, \exp[-\Delta U / k_B T]). \quad (4.16)$$

This method is known as *importance sampling*, as states that contribute most are also weighted strongest. In practice this means that we will accept all trials where the potential energy decreases, otherwise we accept the new configuration only with a probability of $\exp[-\Delta U / k_B T]$.

As the main interest in this work is oriented towards the study of phase behavior in confinement, in particular the liquid–vapor phase transition, the “natural” ensemble to perform computer simulations in is the grand canonical (μVT) ensemble.⁷ This means that the order parameter $\rho = N/V$ is fluctuating, while the chemical potential μ , the volume V and the temperature T are kept constant. This can be achieved by coupling the thermodynamic system to an external basin of particles at the same temperature and chemical potential, but allow for particle and energy transfer between the systems.

7. See [Binder, \(1999\)](#), for example.

In equilibrium, the probability of finding the system in a configuration of N particles at their microscopic states \mathbf{r}^N (at given temperature T , volume V , and chemical potential μ) is given by

$$P(N, \mathbf{r}^N)_{\mu VT} = \frac{1}{\mathcal{Z}(\mu, V, T)} \frac{V^N}{\lambda(T)^{3N} N!} e^{-\beta U + \beta \mu N}, \quad (4.17)$$

where $\beta = 1/k_B T$, U is the internal energy of the system and $\lambda(T)$ is the de Broglie thermal wavelength. The grand partition function $\mathcal{Z}(\mu, V, T)$ is the sum over all possible state in the grand canonical ensemble, therefore normalizes $P(N, \mathbf{r}^N)$, such that $\int P(N, \mathbf{r}^N) = 1$. Integrating Eq. (4.17) over all states at a given N , we can determine the probability of finding the system at a specific particle number N :

$$P(N)_{\mu VT} \propto e^{\beta \mu N} \int d\mathbf{r}^N \frac{1}{\lambda(T)^{3N} N!} e^{-\beta U} \quad (4.18)$$

$$= e^{\beta \mu N} e^{-\beta F(N, V, T)}. \quad (4.19)$$

Note that in Eq. (4.18) the normalizing prefactors have been dropped, as we are not interested in the absolute probabilities, only relative probabilities to a reference state. $F(N, V, T)$ is the *Helmholtz free energy*.

Thus, keeping T and V constant and varying only the particle number, the free energy is a function of the order parameter only. This is especially useful as F is directly related to the probability $P(N)$ of a thermodynamic state, i.e. by measuring $P(N)$ one can obtain a free energy density $f = F(N)/N$,

$$f(N, V, T) = \frac{F(N, V, T)}{N} = -\frac{k_B T}{N} \ln P(N)_{\mu VT} + \text{const.} \quad (4.20)$$

Monte Carlo simulations can then be used to effectively compute a histogram of visited states as function of N by inserting and removing particles with a Metropolis algorithm in the grand canonical ensemble. After each insertion and removal trial N_c , where N_c is the current number of particles, displacement steps are performed. This histogram is used to compute the normalized probability in order to calculate the free energy as of Eq. (4.20).

4.3.1 Successive umbrella sampling

Given the considered system is in a grand canonical ensemble, the probability $P^{(c)}$ of finding the system in configuration c , scales with $P^{(c)} \propto \exp(-\beta F^{(c)})$ (see Eq. (4.20)), where $F^{(c)}$ is the free energy of the system. At system parameters above a critical temperature or outside a phase-separated region, the output probability distribution $P(N)$ will display a single Gaussian peak around the expected particle number N according to the set values of T , V , and μ . When lowering the temperature below the critical temperature T_c and setting coexistence conditions, the system can phase separate and instead of only a single Gaussian distribution around an average density, two peaks will appear – one for each bulk phase, see Figure 4.4a. However, using

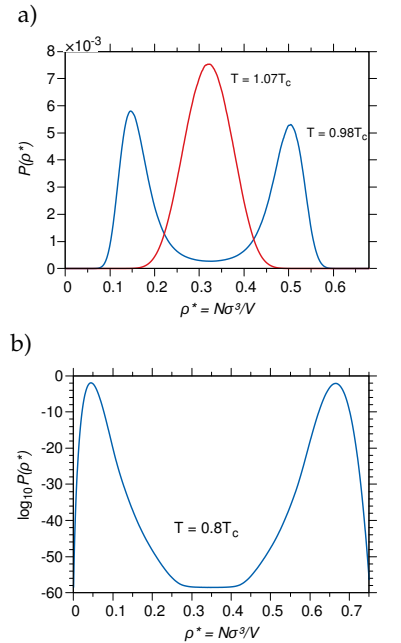


Figure 4.4: Probability distribution of a simple Lennard-Jones fluid at vapor-liquid phase coexistence. The probability $P(\rho^*)$ of visiting a state in the two-phase region at these conditions is ≈ 60 decades lower than for the pure vapor or liquid phases (with σ as the Lennard-Jones diameter of the particles).

direct sampling it will become impossible (especially for temperatures far below T_c) to sample states between these peaks and transition from one bulk phase into the other. Figure 4.4b illustrates this for a vapor–liquid transition at a temperature 20% below T_c : In that case sampling states in the two-phase region is approximately 60 orders of magnitude lower than purely gaseous or liquid states. The free energy cost between the probability maxima and minimum is associated with the creation of an interface between the coexisting phases.

To sample equilibrated states over the full range of the relevant order parameter, more sophisticated sampling schemes are required. Biased sampling methods for Monte Carlo simulations, such as Wang–Landau sampling⁸, transition matrix Monte Carlo⁹, or *successive umbrella sampling*, developed by **Virnau and M. Müller, (2004)**, are techniques trying to overcome such barriers by increasing the probability of visiting otherwise very improbable states (cf. Figure 4.4). The latter sampling method will be introduced in the following.

The main idea in successive umbrella sampling is to discretize the system into n small bins of the relevant order parameter η – e.g. for the liquid–vapor phase transition this could be the volume. Within such a window $[\eta_l, \eta_r]$ the free energy difference should be small, so the sampling probability is similar for all configurations. The system is then allowed to perform normal Monte Carlo moves according to the Metropolis algorithm. At the same time, a histogram of visited configurations as a function of η is recorded. To satisfy detailed balance (see Eq. (4.9)), the system is not allowed to leave the order parameter window. If a state at step k with $\eta^{(k)}$ outside the window is sampled, the move will be rejected, step $k - 1$ is counted once more and serves as starting point for the next Monte Carlo step. Note that this is analogous to the example outlined above for the estimation of π when a displacement leaves the square (see also Figure 4.3). The algorithm for successive umbrella sampling is also summarized in a flowchart in Figure 4.6.

Now, with the above algorithm, as one obtains n local histograms $H[0], \dots, H[n]$, covering the full order parameter range (see also Figure 4.5), containing the information for the complete probability distribution relative to the initial state $P[1]$:

$$\frac{P[n]}{P[1]} = \frac{H[1]_r}{H[1]_l} \cdot \underbrace{\frac{H[2]_l}{H[1]_r}}_{=w[1]} \cdot \frac{H[2]_r}{H[2]_l} \dots \frac{H[n]_r}{H[n]_l}, \quad (4.21)$$

where $H[i]_l, H[i]_r$ indicate the left and right boundary of the i -th window, respectively. If the boundaries of the windows are overlapping, the ratio $w[i] = H[i+1]_l/H[i]_r$ is 1, in non-overlapping scenarios $w[i]$ can be estimated by extrapolating $H[i]$ to $H[i+1]_l$ ¹⁰. **Virnau and M. Müller, (2004)** suggested a second order polynomial for the extrapolation of $w[i]$.

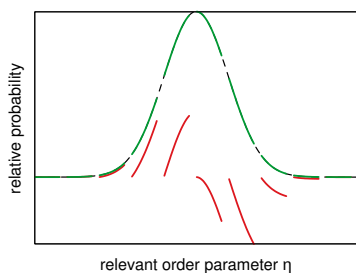


Figure 4.5: Principle of successive umbrella sampling: The full probability distribution (dashed) is reconstructed from smaller windows (red). Within each window, only the relative probability is known. The relative probability for each successive window is extrapolated from the previous. For details, see text.

10. It is also possible to include the information from more than just a single window.

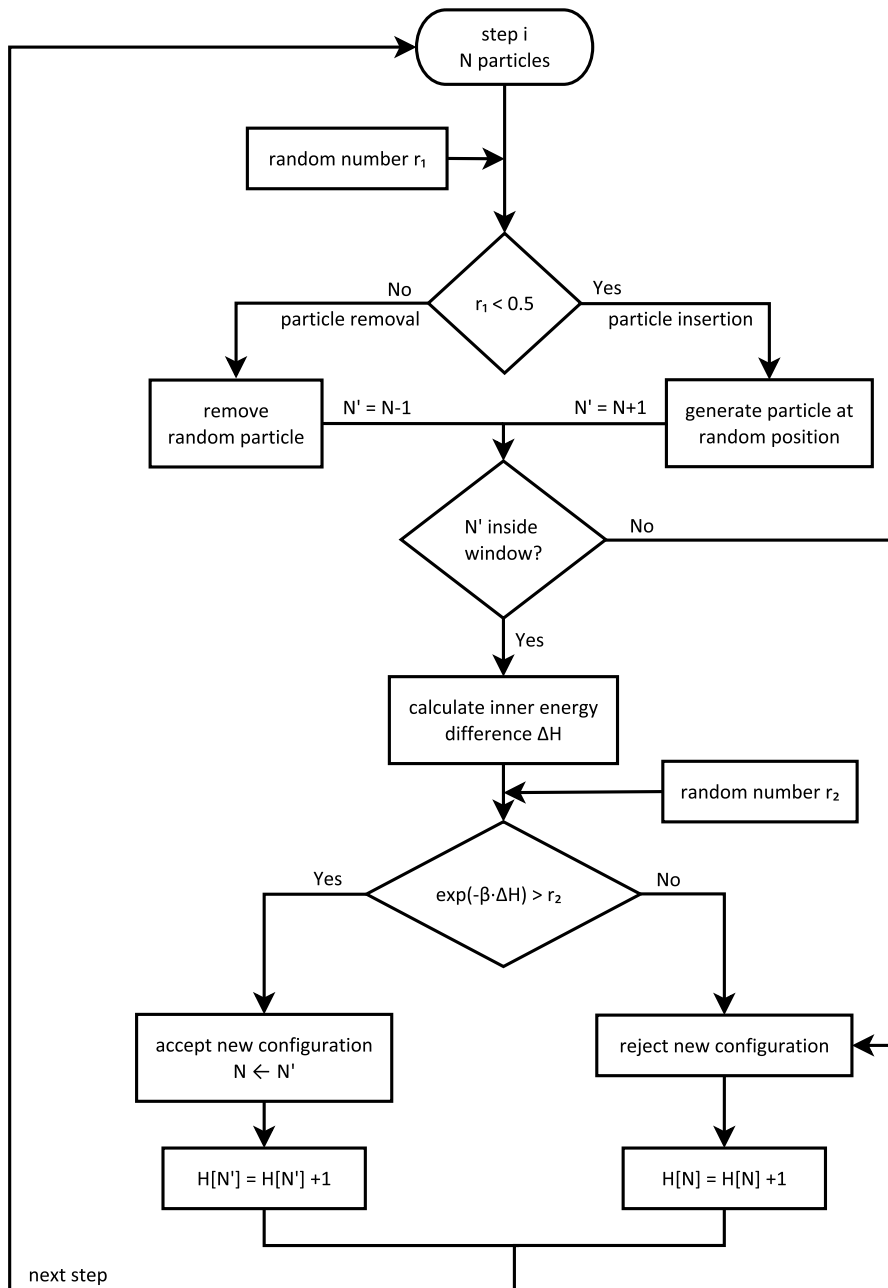


Figure 4.6: Flowchart for grand canonical particle insertion and removal trials using successive umbrella sampling. Random numbers r_1 and r_2 uniformly chosen from the range $[0; 1)$.

4.3.2 Histogram reweighting

Consider the probability function $P(N)_{\mu,VT}$ as in Equation (4.19): changes in μ are weighted exponentially in $P(N)$, and this makes it rather difficult to set the coexistence chemical potential μ_{coex} for a liquid–vapor phase transition – requiring that the bimodal probability distribution having the same weight for both peaks (Binder and D. P. Landau, 1984; Borgs and Kotecký, 1990), as shown in Figure 4.4a.

Histogram reweighting, developed by Ferrenberg and Swendsen, (1988), is a powerful technique for Monte Carlo simulations allowing

the exploration of large parameter ranges from a single simulation run. Applied on GCMC simulations, it can be used to solve the above problem: Consider the probability distributions $P(N)_{\mu'VT}$ and $P(N)_{\mu VT}$ of two ensembles differing in the chemical potential μ and μ' , only. According to Eq. (4.19) they are related via

$$P(N)_{\mu'VT} = e^{\beta(\mu-\mu')N} P(N)_{\mu VT}, \quad (4.22)$$

where $P(N)_{\mu'VT}$ needs to be normalized such that $\sum_{n=N_{\min}}^{N_{\max}} P(n) = 1$, where $[N_{\min}, N_{\max}]$ is the sampling range for the number of particles. The normalization is required to be able to compare the different probability distributions, as distinct simulation parameters (e.g. number of Monte Carlo sweeps, N_{\min}) can shift the free energy by an irrelevant constant value, which translates to a prefactor of $P(N)$.

4.3.3 Method applied in this work

To determine the probability distribution at a given temperature and chemical potential for methane in IRMOF-1, IRMOF-8 and IRMOF-16, we applied grand canonical Monte Carlo (GCMC) using successive umbrella sampling. Additionally, every 200 to 500 particle insertion and removal trials, a displacement move cycle is inserted. In this cycle, N trial displacements are applied to a configuration of N particles. The additional displacement steps allow the system to equilibrate locally after particle insertion (or removal), as new, more optimal positions can be found within the displacement range of a particle. Thus, fewer sampling trials are required overall to obtain equilibrium states. The maximum displacement Δ was set to 0.67 Å, which is $\approx 1/5$ th the diameter of CH_4 molecules. Δ is determined by maximizing the mean squared displacement (MSD) per cycle while trying to keep the acceptance rate high enough to sample the whole phase space.

Starting with very small systems (the MOF structure restricts the allowed system sizes to multiples of the unit cells) of a single MOF unit cell, allows for a first estimation of the coexistence chemical potential. These preliminary runs are also helpful as they give information about the density region a phase transition can occur, therefore effectively reducing the computational effort needed for larger systems. In a next step, system sizes are increased and running the simulation at (or close to) coexistence conditions. Running multiple independent simulations simultaneously (we use 5 to 10 independent runs) will reduce statistical errors in the measurement of observables. In each run the probability of the states as a function of the particle number $P(N)_{\mu}$ will be recorded. $P(N)_{\mu}$ is then subjected to histogram reweighting to calculate $P(N)_{\mu_c}$. At phase coexistence $P(N)$ will display two peaks, and each peak must contribute the same weight to the distribution function (Borgs and Kotecký, 1990; Binder and D. P. Landau, 1984). The first moment of each peak corresponds to the point on the binodal in the phase diagram.

4.4 Finite-Size scaling

Numerical studies of phase behavior are only able to consider finite-sized systems and this imposes a problem: Phase transitions require infinite systems, since the condition of a phase transition is a singularity. And true singularity requires some kind of sum over infinite elements. By observing thermodynamic quantities in system of different sizes, an extrapolation to the thermodynamic limit is possible in many cases.

Consider a cubic system of size $L \times L \times L$ with periodic boundary conditions in the two phase region of the liquid–gas transition. At densities away from of the bulk phases ρ_l , and ρ_g (e.g. around $\rho = (\rho_g + \rho_l)$ and far below the critical temperature) one will observe a region where changes of the density will not result in a change of free energy per volume, but only in a change of relative amounts of the coexisting phases (cf. Figure 4.4). This means the interfaces will be displaced, but its area is preserved (hence, the interface must be planar), as long as the free energy is a horizontal plateau. The associated surface tension $\gamma^{(L)}$ is then (Binder, 1982)

$$\gamma^{(L)} = L \frac{f^{(L)}(T, \rho)}{2}, \quad (4.23)$$

where $f^{(L)}$ is the interfacial free energy per volume of a system where the area of a single interface is $A = L^2$. Data for $\gamma^{(L)}$ versus $1/L$ is shown in Figure 4.7. The non-zero slope indicates that finite-size corrections $\propto 1/L$ are introduced and an extrapolation to $1/L \rightarrow 0$ is required to obtain the bulk value of the surface tension. These corrections are due to the excitation of long-wavelength capillary waves, which will be cut off at wavelengths in the order of L (Widom and Rowlinson, 1970). This is just one example where the finite size of the system introduces modifications to physical quantities – finite size scaling in the vicinity of the critical point becomes particularly important for the study of phase transitions.

4.4.1 Close to the critical point

At the critical point the phase transition is of second order, thus continuous. At this point the correlation length ξ diverges, which also affecting many other physical properties of the material. Following the correlation length, they show a power-law behavior, too (see § 3.1.1 (p. 20)).

However, in finite systems with a linear dimension L , correlations cannot exceed L and corrections compared to the infinite system are introduced. Figure 4.8 displays the behavior of susceptibility χ (or similar fluctuations of the order parameter, e.g. the compressibility in fluids) in the vicinity of the critical point. While in infinite systems ξ can grow indefinitely at T_c , in finite systems it is limited by L . Yet, by carefully observing the phase behavior with finite size scaling analysis, one can learn about the properties of the infinite system. The finite size scaling ansatz states that the singular term of the free energy F

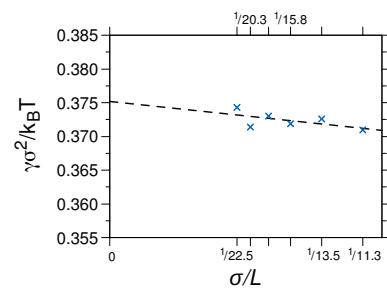


Figure 4.7: Finite-size scaling for the surface tension γ as a function of the system size L . Reprinted from Binder, Block, Virnau, and Tröster, (2012).

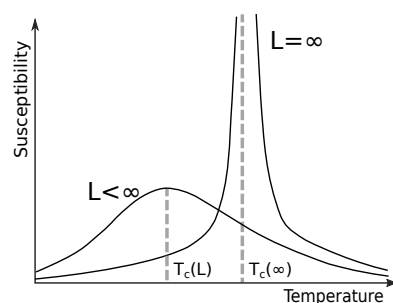


Figure 4.8: Illustration of the susceptibility in a system undergoing a continuous phase transition. In a system with a finite dimension L , the fluctuations are limited by the system size and the critical temperature can be shifted.

can be expressed by (Privman and Fisher, 1984; D. P. Landau and Binder, 2014)

$$F(L, T) = L^{-(2-\alpha)/\nu} \mathcal{F}(\epsilon L^{1/\nu}), \quad (4.24)$$

where $\epsilon = (T - T_c)/T_c$ is the relative distance to the critical temperature. The scaling of the form $\epsilon L^{1/\nu}$ is motivated by the fact that the correlation length is limited by the system size L , and diverges as $\xi \propto \epsilon^{-\nu}$. Note that the above ansatz require temperatures in the critical region and large enough L , otherwise corrections to this scaling must be taken into account. At the critical point $\epsilon = 0$ the above Equation (4.24) simplifies to

$$F(L, T_c) = L^{-(2-\alpha)/\nu} \mathcal{F}^0, \quad (4.25)$$

where \mathcal{F}^0 is a constant amplitude. Therefore, the partial derivatives of the free energy will have a very similar form. In the Ising model, the magnetization $m = -\partial F/\partial H$ exhibits a power-law behavior at T_c upon varying the system size L :

$$\langle m \rangle = -\frac{\partial F}{\partial H} = L^{-\beta/\nu} m^0. \quad (4.26)$$

with the amplitude m^0 .

Similar scaling functions can be found for the susceptibility χ or the specific heat, which can be useful determining ratios of universal exponents. With the analysis of higher-order moments of m and their finite size-scaling, Binder, (1981) has shown that the fourth-order cumulant can be written as

$$U_L = 1 - \frac{\langle m^4 \rangle_L}{3 \langle m^2 \rangle_L^2}, \quad (4.27)$$

where $\langle m^k \rangle_L$ is the k -th moment of the probability distribution $P_L(m)$ in a system with linear dimension L ,

$$\langle m^k \rangle_L = \int dm m^k P_L(m). \quad (4.28)$$

For a probability distribution of the order parameter that consists of two Gaussians $T < T_c$ (each corresponding the order parameter of one of the coexisting phases) $U_L \rightarrow 2/3$, and for a single Gaussian (above T_c) U_L will vanish. But $T = T_c$ for all system sizes U_L collapses into a common universal fixed point, U^* , as illustrated in Figure 4.9. The *Binder cumulant* U_L is quite useful, since it allows to determine the critical temperature accurately from computer simulations from the analysis of probability distributions (which are related to the free energy, see § 4.3 (p. 30)) of different system size. It also allows to identify the universality class of a phase transition as the intersection point U^* , but can vary also depending on the choice of boundary conditions or system geometry.

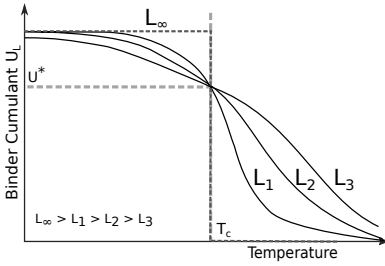


Figure 4.9: Sketch of the fourth-order cumulant U_L as a function of the temperature for different system sizes. In an infinite system (dashed line) it would become a step-function. The critical temperature can be determined from the fixed point U^* of the cumulants of different system sizes $U(L)$.

4.5 Molecular dynamics simulations

Molecular dynamics (MD) is one of the most widely used methods in order to simulate dynamical systems. The underlying principle is very fundamental: The idea is to solve Newton's equations of motion,

$$m_i \frac{d^2 \mathbf{r}_i}{dt^2} = \mathbf{F}_i \quad (4.29)$$

for each particle i with mass m_i and position \mathbf{r}_i on a time-discretized lattice. $\mathbf{F}_i(t)$ is the total force acting on the particle, which is related to the potential via

$$\mathbf{F}(\mathbf{r}(t)) = -\nabla_{\mathbf{r}} V(\mathbf{r}(t)) . \quad (4.30)$$

Thus, thermodynamic variables can be extracted directly from the particle configuration and time-evolution.

One of the most widely used methods to solve the equations of motion is the *velocity Verlet* integration scheme, which reads

$$\mathbf{r}_i(t + \delta t) = \mathbf{r}_i(t) + \mathbf{v}_i(t)\delta t + \frac{\mathbf{F}_i(t)}{2m_i} \delta t^2 + \mathcal{O}(\delta t^4) , \quad (4.31)$$

$$\mathbf{v}_i(t + \delta t) = \mathbf{v}_i(t) + \frac{\delta t}{2m_i} [\mathbf{F}_i(t) + \mathbf{F}_i(t + \delta t)] + \mathcal{O}(\delta t^2) , \quad (4.32)$$

where $\mathbf{r}_i(t)$ and $\mathbf{v}_i(t)$ are the position and velocity of particle i at time t , respectively. In the case of radially symmetric potentials $V(\mathbf{r}) = V(r)$ between particles, the total force on particle i can also be written as

$$\mathbf{F}_i(\mathbf{r}_i(t)) = - \sum_{j \neq i} \frac{\partial}{\partial \mathbf{r}} V(|\mathbf{r}_i(t) - \mathbf{r}_j(t)|) . \quad (4.33)$$

The total energy $E(t)$ at a time t is for Eqs. (4.31), (4.32) is given by

$$E_{\text{tot}}(t) = \frac{1}{2} \sum_i m_i \mathbf{v}_i^2(t) + \sum_i \sum_{j > i} V(|\mathbf{r}_i(t) - \mathbf{r}_j(t)|) . \quad (4.34)$$

The Verlet integration method is a time-reversible, symplectic algorithm. Hence, it is phase space conserving and has a very good long time stability in energy conservation. The energy oscillates with a term scaling with δt^2 around the initial energy

$$E_{\text{tot}}(t) = E_{\text{tot}}(0) + \mathcal{O}(\delta t^2) . \quad (4.35)$$

Therefore, with the above algorithm we conserve the number of particles, volume, and energy, meaning the statistical ensemble is micro-canonical.

4.5.1 Self-diffusion and interdiffusion

One of the very easily accessible transport coefficient from computer simulations is the self-diffusion coefficient D_s . It describes how fast a single particle can observe its surrounding on average. This means,

considering the time-evolution of the single-particle density $\rho_s = \rho_s(\mathbf{r}, t)$

$$\frac{\partial \rho_s}{\partial t} = D_s \nabla^2 \rho_s, \quad (4.36)$$

D_s is the constant measuring the mobility of a single particle. A similar property can be defined for collective behavior, i.e. by the means of a concentration gradients in a binary mixture of species A and B:

$$\frac{\partial c_A}{\partial t} = D_{AB} \nabla^2 c_A, \quad (4.37)$$

where c_A is the concentration of A-particles.

The self-diffusion coefficient D_s can be determined via the Einstein relation:

$$D_s = \lim_{t \rightarrow \infty} \frac{\langle [\mathbf{r}(t) - \mathbf{r}(0)]^2 \rangle}{2dt}, \quad (4.38)$$

where $\langle \cdot \rangle$ is the ensemble average over particles and time. $\langle [\mathbf{r}(t) - \mathbf{r}(0)]^2 \rangle$ is the average mean-squared displacement of a tagged particle. It is very easily measurable in molecular dynamics computer simulation and is typically displayed in a log-log plot (cf. Figure 4.10) as it allows to identify the different regimes from the involved exponents using a single plot. For very short times, particles behave ballistically, as in this short period not collisions with other atoms take place. In this regime the exponent of the time-dependence of the MSD is $\propto t^2$. However, for very long times, the tracer particle has had many collisions with other atoms and the mean-squared displacement is diffusive, and grows linearly with the slope related to D_s via Eq. (4.38), where test particles behave random-walk like with no preferred direction.

The intermediate cross-over regime between ballistic and diffusive time scales is quite complicated and its behavior depends strongly on the density, particle interaction, and so on.

Interdiffusion (also called mutual diffusion) describes processes where concentration gradients are involved and is connected to collective motions like electrical conductivity in ionic liquids. For collective diffusion very similar relations can be established. Whereas for single particle diffusion the displacement of tracer particle positions is considered, for interdiffusion the relevant mean-squared displacement is determined from the center of mass \mathbf{r}_{cm} of a component α :

$$\mathbf{r}_{cm}(t) = \frac{1}{N_\alpha} \sum_{i=1}^{N_\alpha} \mathbf{r}_i^{(\alpha)}(t) \quad (4.39)$$

and the interdiffusion coefficient D_{AB} in a binary mixture with A and B components then can be computed in computer simulation with a relation similar to the Einstein relation above (Horbach, Das, et al., 2007),

$$D_{AB} = \lim_{t \rightarrow \infty} \left(1 + \frac{m_A c_A}{m_B c_B} \right)^2 \phi \frac{N c_A c_B}{6t} \langle [\mathbf{r}_{cm}(t) - \mathbf{r}_{cm}(0)]^2 \rangle, \quad (4.40)$$

where c_α ($\alpha = A, B$) are the respective concentration of the species in the system, m_α the particle mass. ϕ is the thermodynamic factor

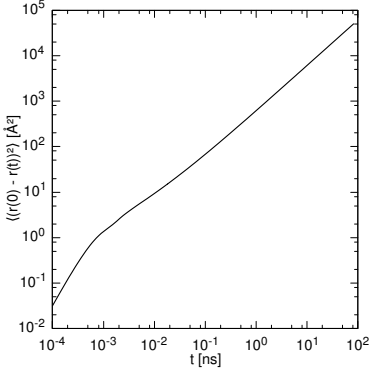


Figure 4.10: Mean squared displacement (MSD) as a function of time in a fluid. For very short time ($t < 3 \times 10^{-4}$ ns) this data shows a ballistic regime (MSD $\propto t^2$), while for very long times $t > 1$ ns the mean squared displacement becomes linear with a slope of D_s , the self-diffusion coefficient.

related to the second derivative of the Gibbs free energy density g ,

$$\phi = \frac{c_A c_B}{k_B T} \frac{\partial^2 g}{\partial c_A \partial c_B}. \quad (4.41)$$

In very dilute systems where no cross-correlations between the particles occur, the collective diffusion coefficient simplifies to a linear combination of the self-diffusion coefficients of both species,

$$D_{AB} = \phi(c_B D_A + c_A D_B), \quad (4.42)$$

which is the Darken equation (Darken, 1949).

4.5.2 Parallelization using GPUs

One of the advantages of the Verlet algorithm is that it is very easy to parallelize since every new configuration at time $t + \delta t$ is dependent on the particle positions ensemble \mathbf{r}^N at the previous time step t . This means one can calculate each particle propagation step independent from the others, thus in parallel. This makes the Velocity-Verlet integration scheme ideally suited for computation on GPGPU¹¹ which are based on massive parallelization of relatively weak microprocessors exploiting the architecture of graphics cards for scientific computation. Such a parallelization does not come without constraints: A graphics processing unit (GPU) has a hierarchical memory model: Very fast local memory (registers), but its scope is restricted to a single thread (processor) and the number of registers is limited. Shared memory, as the name indicated is shared between threads that belong to the same *thread block* (usually 32 threads), it can be used fastest if each thread accesses are synchronized, otherwise a significant slowdown may be observable. It also allows (limited) communication between the threads. The slowest memory type on the GPU is the global memory, it is accessible by all threads and the slowest type of memory (access times approximately 100 times slower than shared memory) but also the largest in capacity. Global memory access should also be executed in a *coalesced* manner, i.e. reads and write should be in parallel and on sequential locations on the memory to make proper use of the available bandwidth in the GPU.

Note that this is a simplified picture of the architecture in GPUs¹², but it should give a general overview about the challenges related to programming on GPGPUs, compared to classic codes for single CPU, where everything is processed serially. Speedups with factors 70 to 100 times faster compared to single CPU cores are not unusual. This enables the computation of systems with more particles, time-steps, but requires more careful programming to maintain the performance advantage. As the programming models and algorithms for serial and parallel computation are very different in many cases, instead of extending available programs written for running on CPUs, HALMD (Colberg and Höfling, 2011) has been written from the ground up for computation on GPGPUs using a modular design both for both the processor architecture and extensibility with regard to numerical algorithms.

11. GPGPU = General Purpose Computation on Graphics Processing Unit

12. A more sophisticated documentation about CUDA programming can be found in *CUDA C Programming Guide v8.0* by Nvidia, (2016).

4.6 Cell- and Verlet neighbor lists

In computer simulations the biggest computational effort is the calculation of the interactions between particles. An optimization of the involved routines and algorithms is compelling, as a speedup there will allow for a simulation of larger systems with more particles or time steps in the same amount of time.

In the worst case, one would have to compute the interaction of each particle with every other particle – in such cases the number of required iterations for the energy or force calculation is of the order N^2 , where N is the total number of particles. But if the interaction range r_c is short, in most of the cases the distance r between the particles will be larger than r_c and not contribute to the particle movement or total potential energy. To improve the efficiency in systems with short-range interaction a widely used technique is to subdivide the simulation box into smaller *cells* as shown in Figure 4.11a. The regular grid allows to calculate the associated cell from a particle position very quickly. With all particles assigned to cells, only pairs of particles in neighboring cells have to be considered (red region in Figure 4.11a). If the cell edge length is equal or larger than r_c , in a three dimensional system one has to consider 27 cells, independent of the total system size, thus reducing the number of iterations required to $\mathcal{O}(N)$. Because there is some computational overhead to the assigning particles to cells and list updates (occurring at each particle removal and insertion), cell lists are only effective for larger system sizes and depending on the cut-off radius r_c . If the cells are too big, neighboring cells may already include most of the particles in the system and the advantage will be gone. In our studies, systems more than 200 CH_4 molecules in the simulated density ranges have proven to be more effective than a naive implementation, as long as there are more than three cells in any linear dimension.

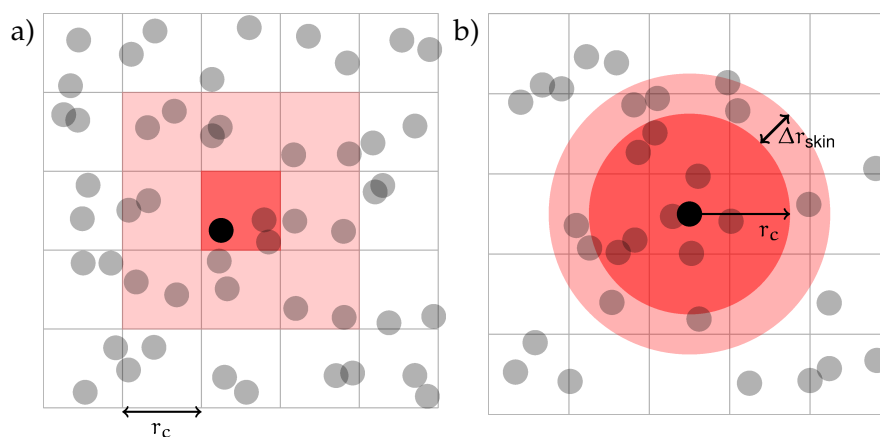


Figure 4.11: a) Sorting particles into *cells*, which can be easily calculated from their position. Particles interacting with the reference particle (black), must be in the neighboring cells (red). b) With Verlet lists each particle maintains its own neighbor list, reducing the number of particles tested for interaction with the reference particle.

The above idea of maintaining a list of particles associated to a

position can be improved further, by modifying the list such that each particle maintains its own list of neighboring particles. Neighbors within the cut-off distance plus a skin, Δr_{skin} are stored in an array as indicated in Figure 4.11b. In this way, one introduces a “grace time”, as an update of all neighbor lists is required only if a particle moves more than $\Delta r_{\text{skin}}/2$ since the last neighbor list update¹³. However, these *Verlet lists* are not applicable in grand canonical particle insertion and removals; in such cases cell lists are required. Yet, for displacement moves or in molecular dynamics simulations, where the particle number is constant, Verlet lists are usually faster than cell lists. If possible, both methods should be combined: The cell lists can be used to look up neighboring particles when the neighbor list needs to be updated.

13. The factor 1/2 in the maximum displacement comes from the fact that both the reference and another particle could move towards each other.

RESULTS

5.1 Evidence for two critical points

The results of this section have been published in Höft and Horbach, (2015) and will be reviewed in this section. Phase behavior in confinement has been extensively studied for a wide range of geometries, such as in confined walls, thin films or cylindrical pores. Metal-organic frameworks, on the other hand, form an ordered, porous network opening the possibility of new classes of phase transitions. Experimental and computer simulation studies¹ have shown that the arrangement of guest particles in MOFs can change for different pressures: At very low densities, the guest particles preferably occupy sites close to the metallic clusters. When increasing the pressure, the adsorbed molecules form a wetting layer on the whole surface of the porous medium. For even higher densities, pores can be filled completely with molecules. This poses the question whether the above structural changes are connected to phase transitions (and therefore coexistence of different macroscopic bulk phases separated by an interface) and critical points. It is not obvious how the heterogeneous structure affects phase behavior.

In fact, we find two lines of first-order phase transitions of CH₄ in IRMOF-1, the IS (IRMOF-surface) and ILG (IRMOF-liquid-gas) transitions, both ending in a critical point. The location and structure of these phase transitions have been determined by using grand canonical Monte Carlo (GCMC) computer simulations in combination with successive umbrella sampling (see also § 4.3 (p. 30)). The details of the applied particle model of the MOF and CH₄ can be found in § 4.2 (p. 27). The presented results are collected from averages over 10 independent runs using 2×10^7 trial removals and insertions in each histogram window. After every 400 insertion and removal, a displacement cycle is applied to a given configuration of N particles, consisting of N trial displacements of a random particle with a maximal displacement of 0.67 Å. The cubic unit cell of IRMOF-1 is shown in Figure 5.1 and has an edge length of $L_{\text{unit}} = 26.669$ Å and the considered system size edge lengths L are multiples of the unit cells, ranging from $L = 2L_{\text{unit}}$ to $4L_{\text{unit}}$.

Fixing the volume V, temperature T and the chemical potential μ , and allowing the particle number N to fluctuate, a result we obtain from GCMC simulations is the probability distribution P(N) as a function of N (which is related to the free energy F(N) of the system, see Eq. (4.20)). A first-order phase transition requires a bimodal

5

1. Rowsell, Spencer, et al., 2005; Rosi, Eckert, et al., 2003; Yildirim and Hartman, 2005; Siberio-Pérez, Wong-Foy, Yaghi, and Matzger, 2007; Uzun and Keskin, 2014; Mueller and Ceder, 2005; Walton, Millward, et al., 2008; Dubbeldam, Frost, Walton, and Snurr, 2007; B. Liu, Q. Yang, et al., 2008; Fairen-Jimenez, Seaton, and Düren, 2010

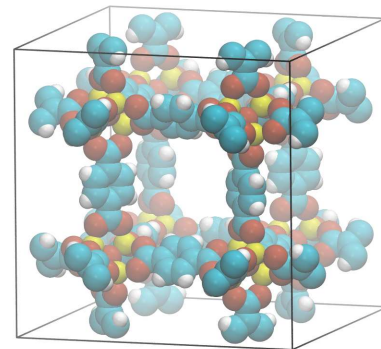


Figure 5.1: Unit cell of IRMOF-1 crystal. Spheres represent different atoms, the color of the sphere indicates the element: C (turquoise), O (red), H (white) and Zn (yellow). From Höft and Horbach, (2015).

2. See Ferrenberg and Swendsen, (1988) and Binder and D. P. Landau, (1984).

distribution in $P(N)$ with both peaks having equal weights². Each peak then corresponds to one of the coexisting densities at $\rho_{\text{low}} = N_{\text{low}}/V$ and $\rho_{\text{high}} = N_{\text{high}}/V$, respectively. The coexistence chemical potential is estimated in preliminary runs and then accurately set to μ_{coex} via histogram reweighting, such that the area under both peaks around ρ_{low} and ρ_{high} becomes equal, meaning that both phases have the same free energy (see also § 4.3.2 (p. 35)). In Figure 5.2 the logarithm of $P(N)$ is displayed for the two observed phase transitions under coexistence conditions for different temperatures below the critical temperature T_c .

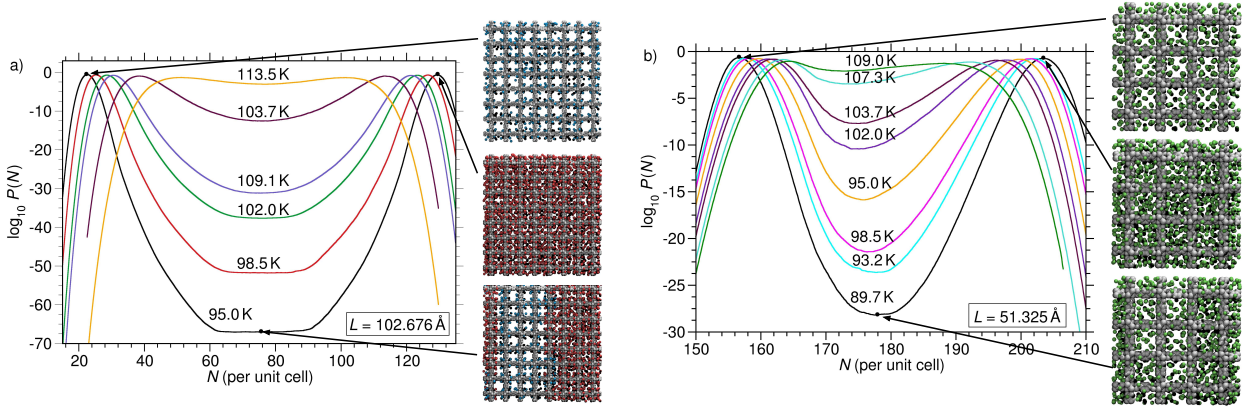


Figure 5.2: Probability distributions for (a) IS and (b) ILG phase transitions at different temperatures at coexistence chemical potential. Data from system sizes $L = 4L_{\text{unit}}$ (IS) and $L = 2L_{\text{unit}}$ (ILG) is shown. From Höft and Horbach, (2015).

Snapshots of pure phases at $T = 95.0\text{K}$ for the IS and at $T = 89.7\text{K}$ already indicate that the IS transition is a transition between configurations of different wetting layers on the framework, while in the ILG transition the difference in coexisting phases lies in the filling of pores. In both transitions, the configurations in the two-phase regions also suggest planar, two-dimensional interfaces separating the coexisting phases from each other. The probability distributions as in Figure 5.2 are directly related to the phase diagram in the density–temperature plane, as the maxima in $P(N)$ are points of the binodal. Figure 5.4 shows the binodals of the IS and ILG phase transitions as a function of the CH_4 mass density $\rho_m = NM_{\text{CH}_4}$, with $M_{\text{CH}_4} = 26.63 \times 10^{-24}\text{g}$. For reference, the figure also includes the binodal of the liquid–gas phase transition of bulk CH_4 , with a critical temperature at 190 K. Using finite-size scaling of the Binder cumulant, U_L in the IS transition yields a critical temperature of $T_c^{\text{IS}} = 114.5\text{K}$. The critical temperature of the ILG is estimated via the scaling relationship of the coexistence diameter

$$\Delta\rho \equiv \rho_h - \rho_l = A_{\text{op}} \left(\frac{T_c - T}{T_c} \right)^\beta, \quad (5.1)$$

where A_{op} is a critical amplitude and ρ_l and ρ_h are the densities of the dilute and dense phases, respectively. Assuming 3D Ising universality, i.e. setting $\beta = 0.326$ (Pelissetto and Vicari, 2002), fits of Eq. (5.1) for

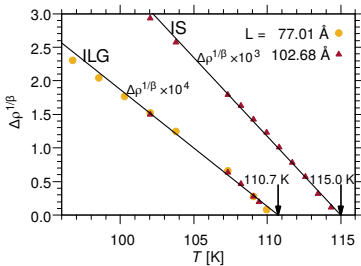


Figure 5.3: Rectification plots of the order parameter scaling laws as a function of temperature for IS and ILG phase transitions in IRMOF-1 assuming 3D Ising universality ($\beta = 0.326$). $\Delta\rho$ is measured in units of g cm^{-3} .

the two transitions can be found in the inset of Figure 5.4a. The critical density ρ_c can be estimated by a coexistence diameter law (Widom and Rowlinson, 1970) for $\delta \equiv (\rho_{\text{low}} - \rho_{\text{high}})/2$ via

$$\delta \propto (T - T_c)^{1-\alpha}, \quad (5.2)$$

with $\alpha = 0.113$ (Pelissetto and Vicari, 2002). Due to the smallness of α , Eq. (5.2) is treated as linear instead (i.e. $\alpha = 0$). The fits of the coexistence diameter laws can be found as solid lines in Figure 5.4a.

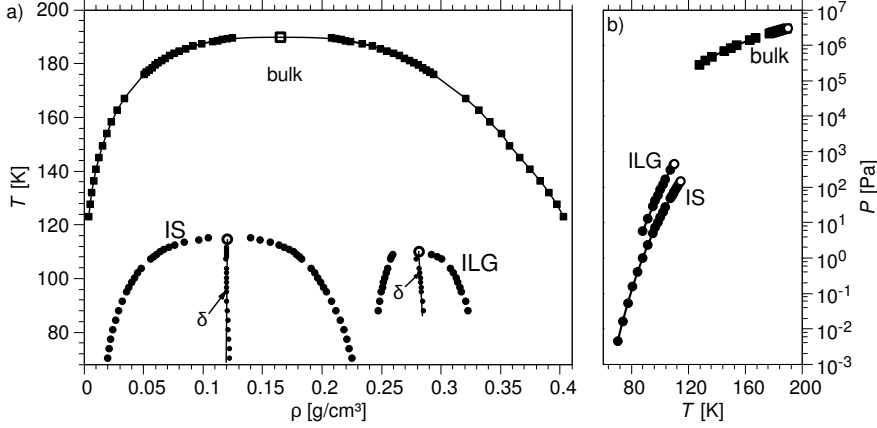


Figure 5.4: Phase diagram in the a) density-temperature and b) temperature-pressure plane for the IS and ILG phase transition of CH₄ in IRMOF-1. Critical points are shown as open symbols. The coexistence diameter $\delta \equiv (\rho_{\text{high}} - \rho_{\text{low}})/2$ is shown with fits to the coexistence diameter law (cf. Eq. (5.2)). From Höft and Horbach, (2015).

Note that the coexistence chemical potentials (and therefore also pressures) for IS and ILG transitions are at different values. In Figure 5.4b the coexistence lines are displayed in the temperature-pressure plane and it reveals that the critical pressures are 3 to 4 orders of magnitudes lower than the bulk critical pressure.

We also use a finite-size study of the IS phase behavior using Binder's cumulant U_L introduced in Binder, (1981) to determine T_c and the universality class accurately. This fourth order cumulant is defined as

$$U_L = 1 - \frac{\langle \rho_M^4 \rangle}{3 \langle \rho_M^2 \rangle^2}, \quad (5.3)$$

where $\langle \rho_M^n \rangle$ is the n th moment of the probability distribution $P(\rho_M)$, thus $\langle \rho_M^n \rangle = \int d\rho_M^n P(\rho_M)$. For different system sizes curves of $U_L(T)$ are expected to intersect at an universal value U_L^* . The intersection point determines the critical temperature and its value is dependent on the universality class of the system. For 2D-Ising universality it is found to be $U_L^* = 0.61069$, and for 3D-Ising universality classes $U_L^* = 0.4655$.³ In Figure 5.5 the Binder cumulant is shown for three system sizes. The intersection point at $T = 114.52$ K, gives U_L^* very close to the universal value of 3D universality and let us conclude that the IS transition is in fact compatible with 3D Ising universality. Due to the finite size of the system, small corrections to $U_L^* = 0.4655$ are expected.

3. The universal value of U_L^* for 2D Ising universality can be found in Kamieniarz and Blote, (1993), while the cited value for 3D Ising was reported by Luijten, Fisher, and Panagiotopoulos, (2002).

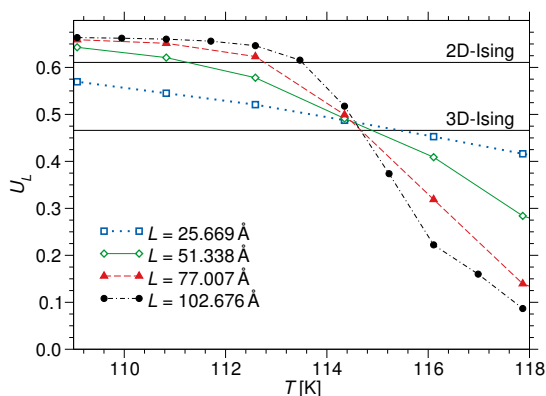


Figure 5.5: Temperature dependence of Binder cumulant, U_L , for different system sizes, as indicated. Horizontal lines indicate the universal values of U_L , as expected for the 2D and 3D Ising universality class.

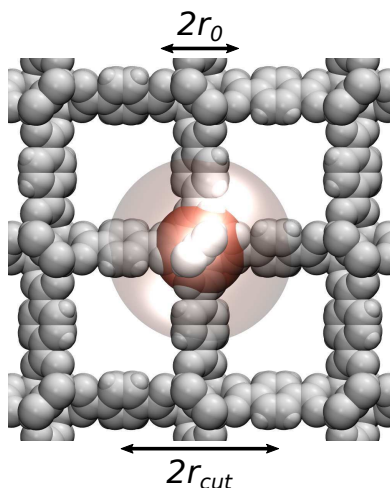


Figure 5.6: Illustration for the calculation of the coordination parameter z around the metallic clusters. Only particles within in the shell $r_0 < r < r_{\text{cut}}$ contribute to coordination z . From Höft and Horbach, (2015).

The structure of the IRMOF–liquid–gas transition is, as its name suggests, related to the liquid–gas transition of the bulk fluid, with the difference this transition takes place in the pores of the system: On the one hand almost empty pores (particles are mostly on the surface of the framework) which can be in coexistence with pores filled very densely with a liquid phase of CH_4 (cf. snapshots in Figure 5.2b). The IS phase transition is compared to the ILG transition very different: In the IS dilute phase, molecules preferably arrange only around metallic clusters and in the dense phase a wetting layer covering the whole IRMOF-framework. We quantify the change of ordering by introducing a radial distribution function g_{met} with respect the Oxygen atom located in the center of the metallic cluster, as illustrated in Figure 5.6. $g_{\text{met}}(r)$ measures the probability of finding CH_4 molecules at a distance r , relative to the ideal gas at the same bulk density.

Figure 5.7 displays $g_{\text{met}}(r)$ for 96.7, 107.3 and 113.5 K and the curves for the low- and high density IS phases show very distinctive behavior. As the atoms of the metallic cluster occupy space by themselves and are repulsive at short distances, no methane particles can be found for $r \leq 4 \text{ \AA}$. Then, remarkably, in the low density phase g_{met} exhibits a double-peak structure. In this phase methane molecules prefer adsorption sites very close to the metallic cluster, but some of them are a little further away. As the snapshot in Figure 5.6 indicates, the shoulder originates from particles adsorbed on the organic linkers, close to the metallic center. However, in the high density IS phase the double-peak is mirrored; while the first peak is practically absent, the second peak more pronounced. Thus, in the dense phase methane is covering all the inner framework surface, forming a wetting layer on the MOF surface. In the pores $4.0 < r < 7.0 \text{ \AA}$ essentially no molecules are present, which we have confirmed by explicitly counting the atoms. The second two-peak structure around $r \approx 10 \text{ \AA}$ corresponds to particles around the next metallic center.

While at low temperatures the two phases are very distinct, at temperatures closer to T_c they become more similar and are barely distinguishable from each other and the two phases become identical

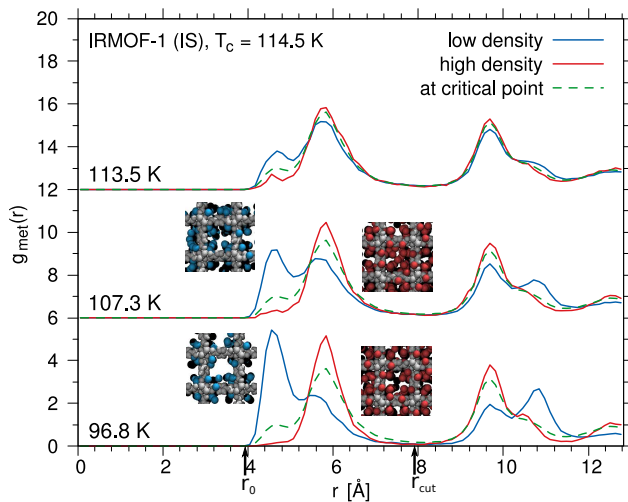


Figure 5.7: Radial distribution function $g_{\text{met}}(r)$ for the coexisting phases in the IS phase transition at $T = 96.8, 107.3$ and 113.5 K. The radial particle distribution around the metallic clusters at the critical point is shown in dashed lines. Snapshots on the left correspond to the low density phase, snapshots on the right to the high density phase. For clarity, $g_{\text{met}}(r)$ for higher temperatures have been shifted by multiples of +6 on the ordinate. From Höft and Horbach, (2015) with additional data for 113.5 K.

at the critical point, as expected.

The strong differences between $g_{\text{met}}(r)$ allow for introducing a local order parameter: Namely the number of particles z around a metallic center within a distance $r < r_{\text{cut}} = 7.995 \text{ \AA}$, as indicated in Figure 5.6 and Figure 5.7. To confirm the validity of z as an appropriate choice as order parameter, we mapped z to the binodal of the IS transition (cf. Figure 5.8), which shows strong agreement that (at least close to the critical point) z can be mapped to the particle density and it is a reasonable choice to distinguish between the two phases locally. The resulting critical coordination number is $z_{\text{cr}} = 9.58$. The identification of the local phase in a single configuration via z is applied by determining z around each $\text{Zn}_4\text{-O}$ cluster, and if $z_{\text{local}} < z_{\text{cr}}$ then all particles are assigned to the dilute phase. All remaining CH_4 molecules must be in the dense phase of the IS transition. An example snapshot is where this scheme is applied to a configuration in the two-phase region is shown in Figure 5.9 and allows for an identification of the location of the planar interfaces, separating the coexisting phases. A detailed study of the interfaces can be found in § 5.3 (p. 64).

5.1.1 Conclusion

We have successfully applied grand canonical Monte Carlo simulations with successive umbrella sampling to investigate the phase behavior of methane within IRMOF-1. Remarkably, in addition to a condensation transition in the free volume of the pores we find a novel phase transition on the inner surface of the MOF, the IS transition. Both of the first-order phase transitions end in a critical point and we have shown they belong to 3D Ising universality. This IS condensation

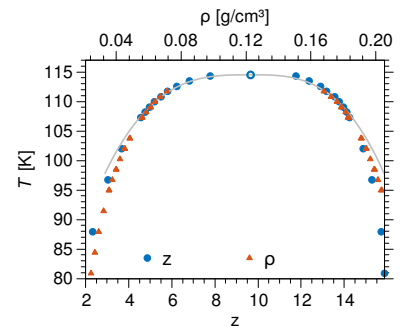


Figure 5.8: Coexistence temperatures as a function of coordination around metallic clusters, z , and methane density in IRMOF-1, ρ . The critical point is shown as open symbol.

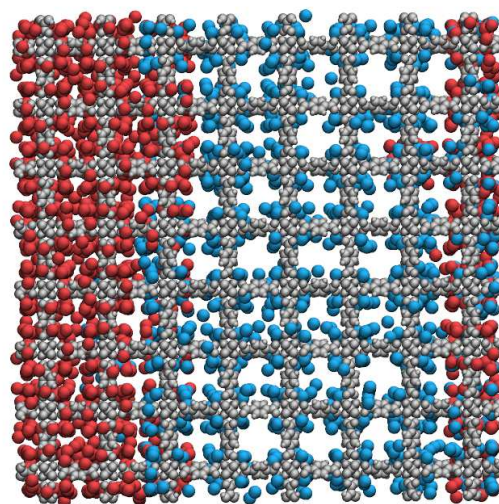


Figure 5.9: Snapshot of CH_4 in IRMOF-1 at coexistence conditions at 70 K of the IS phase transition. Colors indicate the local phase of CH_4 , low density (blue) and high density (red) are determined from the local order parameter z . IRMOF-1 atoms are shown in grey color.

transition occurs in a pressure region $1.0 < P < 10 \times 10^3 \text{ P}$ at temperatures around 100 K and is characterized by the coexistence of two heterogeneous bulk phases. Other IRMOFs are expected to show a very similar phase behavior, as they only differ in the linker and the heterogeneity of the framework is still in place there. The available linker surface area and pore volume varies of course and will influence the exact parameters of the transitions. Utilizing the same methods as for IRMOF-1, in the next section we will present the phase behavior of methane in two other IRMOFs, IRMOF-8 and -16. With the same topology as IRMOF, the aim is to study the interplay between pore size, linker length and the heterogeneous interaction with its guest molecules on the phase behavior in IRMOFs.

5.2 Dependence on pore size

In the previous chapter we analyzed the phase behavior and structure of these phases of Methane in IRMOF-1. One of the advantages of MOFs is the tailorable framework architecture and in the following we study the phase behavior of methane in other IRMOFs: IRMOF-8, and IRMOF-16 and compare these with the results of CH₄ in IRMOF-1.

The studied MOF materials are very similar with respect to their geometry and atomic structure. They have an identical symmetry of the cubic framework, where the corners of the structure built by Zn₄O clusters. By replacing the “connection” (i.e. the ligands) between the corners, we get a new MOF with different chemical and physical properties. To understand the influence of the pore size on the phase behavior, we chose ligands that are structurally very similar to those in IRMOF-1. This allows to concentrate the study on the influence of the pore size to the phase behavior only. The structural formulas for each linker can be found in Figure 5.10. The edge lengths of a single pore as determined from Eddaoudi, Kim, et al., (2002) are $L = 6.88 \text{ \AA}$ (IRMOF-1), 8.09 \AA (IRMOF-8) and 11.52 \AA (IRMOF-16). The unit cells of these IRMOFs are displayed in Figure 2.6 (p. 11). To visualize the differences between the IRMOFs in the potential

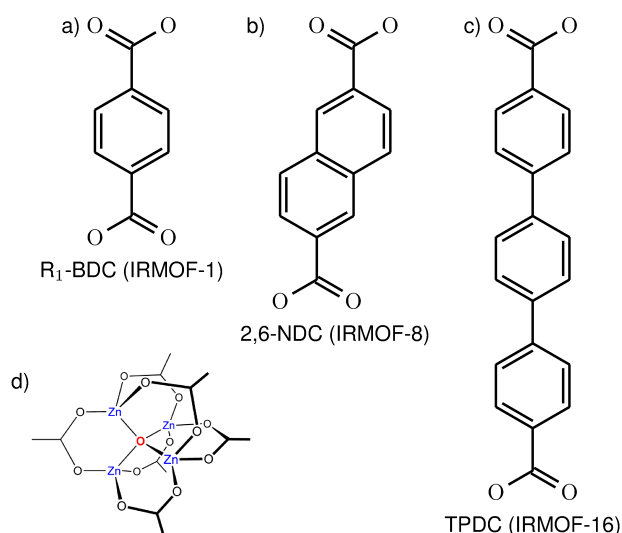


Figure 5.10: The different ligands for a) IRMOF-1 (1,4-benzenedicarboxylate, BDC), b) IRMOF-8 (naphthalenedicarboxylate, NDC), and c) IRMOF-16 (terphenyldicarboxylate, TPDC). The ligands connect the metallic Zn₄O- clusters (d) at the corner of the framework and define the porosity of the medium. Source for d): <https://commons.wikimedia.org/wiki/File:BasicZnAcetate.png>.

energy, we have determined the interaction energy exerted from the MOF atoms on a single methane molecule. A slice of this energy map in the layer of the linkers (i.e. in the strongest confinement) is shown in Figure 5.11.⁴ In this figure, white regions indicate regions with a very low probability to find methane particles, which includes everything outside the pore, as the repulsive part of the Lennard-Jones interactions with the framework becomes dominant. The dark blue

4. The coordinates in the potential energy map correspond to the center of a single methane molecule. The diameter of CH₄ in our model is 3.73 \AA .

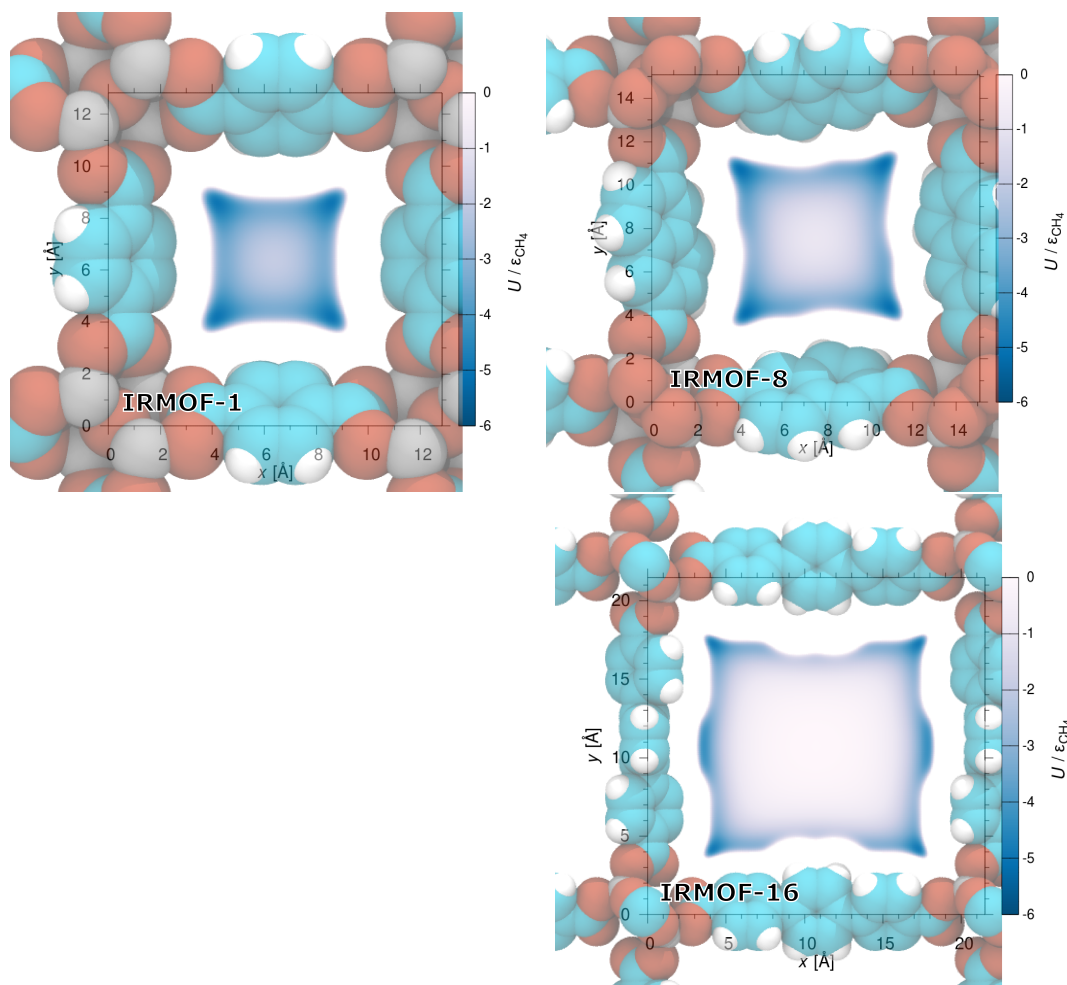


Figure 5.11: Slice in the potential energy in the layer of the metallic clusters. The landscape is showing only energies $U < 0$. Approximate positions of framework yatoms added for orientation. The white regions outside the pore corresponds to potential energies > 0 and very unlike/forbidden regions to find methane particles.

regions indicate locations with a low potential energy. Entropic effects aside (i.e. at zero temperature), in these regions it is more likely to find methane particles. This is only a very rough estimate, though. Still, in accordance to our finding in the previous section, we find potential minima at the corners of the framework. Also, with larger the pore sizes the attraction of the framework will reach less into the pore, as indicated by the larger white regions in the center of IRMOF-8 and -16. Therefore, we can expect the guest particles to get into the pores less likely, upon increasing the linker size. On the other hand, as the free pore volume increases, the ILG transition will be more dominant because the relative volume of low-energy pockets compared to the pores decreases.

5.2.1 Results

As in the study of phase transitions in IRMOF-1, the central output of the GCMC simulation are the probability distributions $P(N)$ as a

function of the density (or equivalently, number of adsorbed particles per unit cell) at coexistence conditions. In Figure 5.12 for the largest simulated system sizes, the $P(N)$'s are shown for the IS and ILG transition for IRMOF-1, -8, and -16. Note that these plots do not include all measured histograms, those which were very close to the critical temperature have been left out for clarity.

Probability distributions First, let's consider the IS transition: In IRMOF-1 and -8 the densities of the phases are quite similar, even though in the denser phase IRMOF-8 is able to adsorb more particles due to its larger surface area. IRMOF-16, however, seems to be able to adsorb a *much* larger amount of molecules, which could be caused by the much larger inner surface area (per unit cell) and the very low temperatures at which we find the phase transition. Due to this large number of particles, and the required computational effort, probability distributions at even lower temperatures have not been computed. If the temperature is far enough away from T_c , a plateau in $P(N)$ can be observed. In this region planar interfaces separate coexisting phases. The structure of the interface is analyzed in detail in § 5.3 (p. 64), which also includes a discussion of the oscillations in the probability distribution as seen in the IS transition of IRMOF-8 (Figure 5.12b). In the same histogram we also observe a slight tilt of the expected plateau regime. This is an artifact from Monte Carlo sampling that is not perfectly equilibrated, since acceptance rates of particle insertion and removal sweeps drop with temperature. Note that, if the histogram was reweighted such that the plateau was planar, the maximum at higher densities is shifted only marginally.

Due to the high densities of the ILG phases, which decrease the acceptance rate even further, the investigation concentrates on the region closer to the critical point. As the thermal fluctuations are larger, a plateau in the histogram indicating a planar interface is not directly observable, except for IRMOF-16. There, we find similar oscillations of the free energy barrier (visible for 102.0 and 112.6 K in Figure 5.12c) which is associated to the shape of the interface, and its alignment to the framework structure. Compared to the IS distributions, the ILG transitions seem to be more asymmetric with respect to the critical density ρ_c , the dilute phase is typically closer to the critical density, especially in IRMOF-1.

Binodal curves Figure 5.13 shows the binodals of all the found phase transitions in the studied IRMOFs, the exact values of the critical values of temperature, density and pressure are summarized in Table 5.1. The points of the binodal lines have been directly obtained from the probability distributions above. The first moment of each peak in the histograms corresponds to a point on the coexistence lines in the density–temperature phase diagram.

One can observe different behavior for the widths and critical temperatures of the IS and ILG binodals depending on the MOF – and therefore the porosity. Both the width and the critical temperatures of

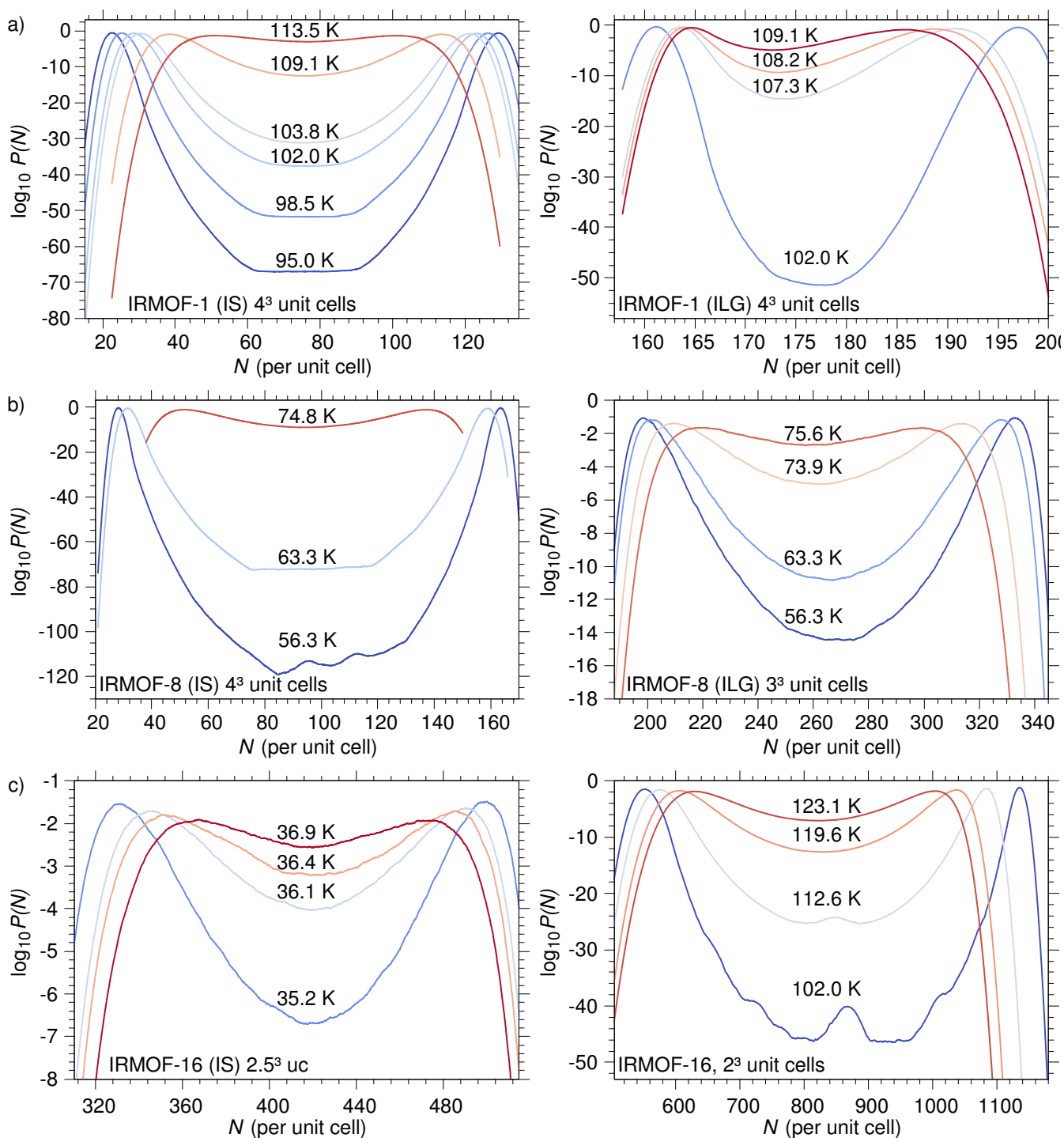


Figure 5.12: Semilogarithmic plots of the probability distribution $P(N)$ as a function of number of particles per unit cell N at coexistence conditions for the IS (left panel) and ILG (right panel) phase transitions for the largest available system sizes.

ILG transition are increasing with pore size, as seen in Figure 5.13b. This effect is caused by an increase free volume and decreasing interaction of the framework with the methane molecules. With larger pore size the low density branch of the ILG transition will shift to lower

densities, because the number of adsorbed particles per unit volume will decrease (in the dilute ILG phase almost all particles are located on the surface of the framework) and the liquid branch will allow higher densities per volume as the excess free volume also increases. A more “bulk-like” with larger linker size is reasonable, as in the limit of infinite pore size the phase behavior must become identical to the bulk liquid–vapor transition. As seen in Figure 5.13a for the IS transition the inverse occurs, the critical temperature is lowered significantly with increasing pore size. This indicates that thermal fluctuations can inhibit the IS phase transition if the metallic centers are very far apart from each other – even though the accessible surface area for the molecules increases.

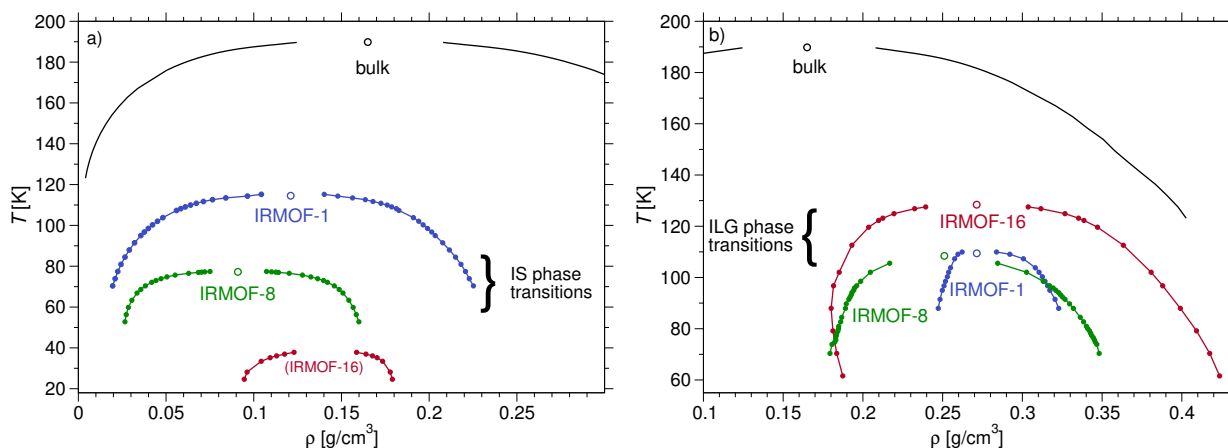


Figure 5.13: Coexistence curves of a) IS phases and b) ILG phase transitions of CH₄ in IRMOF-1 (blue), IRMOF-8 (green) and IRMOF-16 (red). Critical points are shown as open symbols, bulk CH₄ liquid–vapor binodal (black line) added for reference.

Determining a direct relation between linker size and critical density of the two-phase region from Figure 5.13 is not obvious. While ρ_c in the IS transitions from IRMOF-1 to IRMOF-8 shifts to lower densities, in IRMOF-16 it increases again. This could be related to the large inner surface area accessible to the gas atoms. It could also imply that the structure of the coexisting phases is qualitatively different. The ILG coexistence regions become broader with linker size and the but the critical temperature is almost identical for IRMOF-1 and -8 (110.7 K and 108.4 K, respectively). It appears plausible that the larger inner surface area compared to the length of the organic linkers in IRMOF-8 (see Figure 5.10) yields a stronger influence to gas particle in the pores, thus reducing the free pore volume and the critical temperature. This claim is supported by the fact that the dense ILG phases of IRMOF-1 and -8 have very similar particle densities.

Further, at lowest measured temperatures the dense phase of the IS and the dilute phase of the ILG transition have very similar densities. These phases are closely related to each other and it is possible that they may, at very low temperatures, become identical. Consequently, at such a triple point, three phases could be in coexistence: (i) The

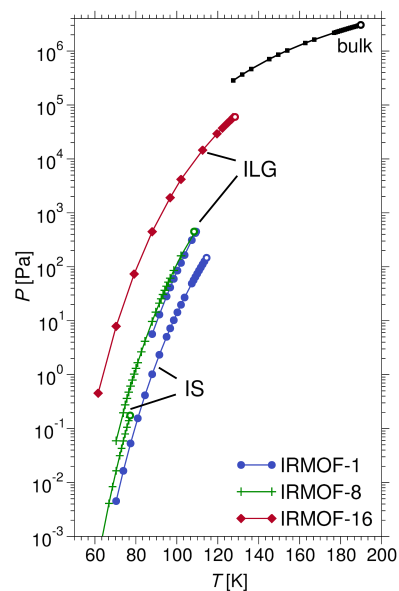


Figure 5.14: Coexistence pressure lines for IS and ILG phase transitions for IRMOF-1 (blue), -8 (green) and -16 (red, without IS phase). Critical points are shown as open symbols.

dilute IS phase, (ii) the dense ILG liquid phase where all particles are liquefied in the MOF, and (iii) the phase where the whole framework is covered by methane molecule. For a clearer picture, in Figure 5.15 the IS and ILG transitions are shown in a common phase diagram. The phase diagram suggests a triple point for IRMOF-1 at temperatures < 50 K. Still, it is quite speculative, since crystallization of methane can occur as well (and has been reported by Magdysyuk, Denysenko, et al., (2014) for Argon in the MOF MFU-4l) and a simple extrapolation is not very safe, anyway.

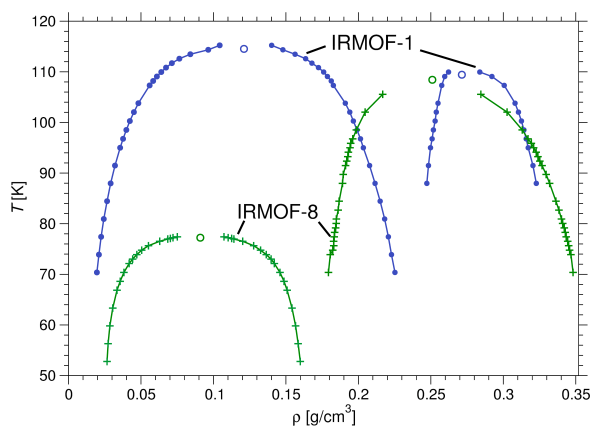


Figure 5.15: Binodal coexistence curves for IS and ILG phases in IRMOF-1 (blue) and -8 (green). At very low temperatures a triple point could exist.

| | T_c (K) | ρ_c (g/cm ³) | P_c (Pa) |
|-----------------|-----------|-------------------------------|------------------------|
| IS transitions | | | |
| IRMOF-1 | 114.5 | 0.120 | 1.466×10^2 |
| IRMOF-8 | 77.2 | 0.091 | 1.748×10^{-1} |
| IRMOF-16 | (36) | (0.14) | – |
| ILG transitions | | | |
| IRMOF-1 | 110.7 | 0.281 | 4.509×10^2 |
| IRMOF-8 | 108.4 | 0.251 | 4.497×10^2 |
| IRMOF-16 | 128.4 | 0.528 | 5.995×10^4 |

Table 5.1: Critical values for the IS and ILG transition of methane in IRMOF-1, -8 and -16.

Binder cumulants and scaling close to T_c The Binder cumulants U_L for the IS phase transitions are shown in Figure 5.16. From the intersection of U_L for different system sizes $L \times L \times L$ (where the cubic system size is always in multiples of the unit cell of the IRMOF), we determine the critical temperature and universality class of the phase transition in the same way as done in § 5.1 (p. 45). We find that in IRMOF-8 the intersection point of the Binder cumulants of different system sizes U_L is slightly larger than for IRMOF-1 at similar number of unit cells. Since U_L^* converges towards the universal value for the

3D Ising universality, we can conclude that this is due to corrections caused by the finite size of the system. These corrections are due to the larger pore size of IRMOF-8, compared to IRMOF-1. The phase transition for IRMOF-16 at low densities on the other hand is qualitatively different in the behavior of the cumulant: For all system sizes, U_L^* is much closer to the universal value of the 2D Ising behavior with $U_L^* = 0.61069$ (Kamieniarz and Blote, 1993); it is not obvious why an apparent change in the universal behavior should occur. It is possible that this transition is associated with a second layer of methane molecules around the metallic clusters and on the framework surface. Simulating system sizes larger than $5 \times 5 \times 5$ unit cells was not possible in this case, as the number of required particles increases significantly and thus the computational effort.

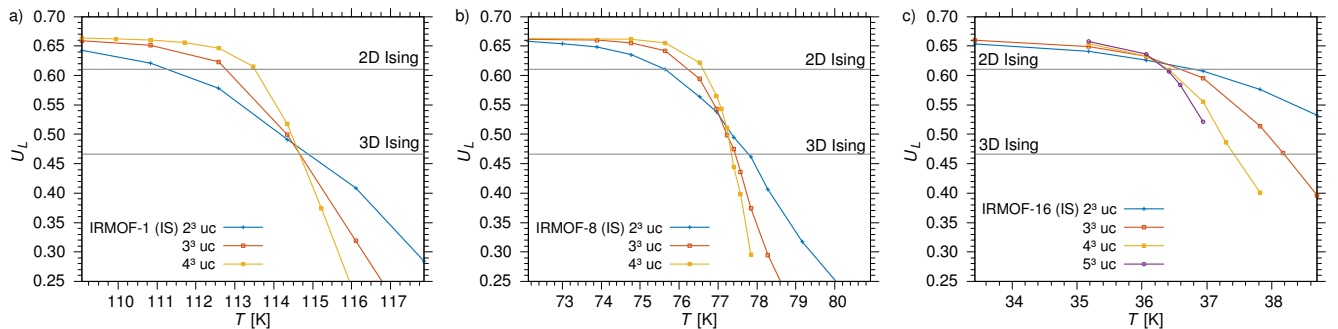


Figure 5.16: Finite-size behavior of the Binder Cumulant $U_L(T)$ for the IS phase transitions in the IRMOF systems (a) IRMOF-1, b) IRMOF-8, and c) IRMOF-16) for different system sizes (given in multiples of unit cells).

For the ILG transitions, on the other hand, we assumed 3D Ising universal behavior and then plotted $\Delta\rho^{1/\beta}$, where

$$\Delta\rho \equiv \rho_h - \rho_l = A_{op} \left(\frac{T_c - T}{T_c} \right)^\beta, \quad (5.4)$$

as a function of the temperature. The points of $\Delta\rho$ should then collapse on a single line with the slope $A_{op}^{1/\beta}$ and the intersection with the abscissa then gives the critical temperature. Figure 5.17 displays these rectification plots for all simulated MOFs.

Structure of phases As the IS phase transition is caused by the heterogeneous interaction of methane molecule with the metallic clusters and organic linkers, we utilize the radial distribution g_{met} of methane particles as a function of distance r to the central Oxygen atom in the metallic cluster to characterize the phases, as explained in § 5.1 (p. 45). Figure 5.19 displays $g_{met}(r)$ for the studied MOFs for temperatures below and close to T_c .

We find qualitative similarities in the IS phases of IRMOF-1 and -8. In the dilute phase almost all methane particles can be found in the vicinity of the metallic clusters at distances $4.0 < r < 7.0 \text{ \AA}$ from the central Oxygen atom in the metallic site. This is in good agreement

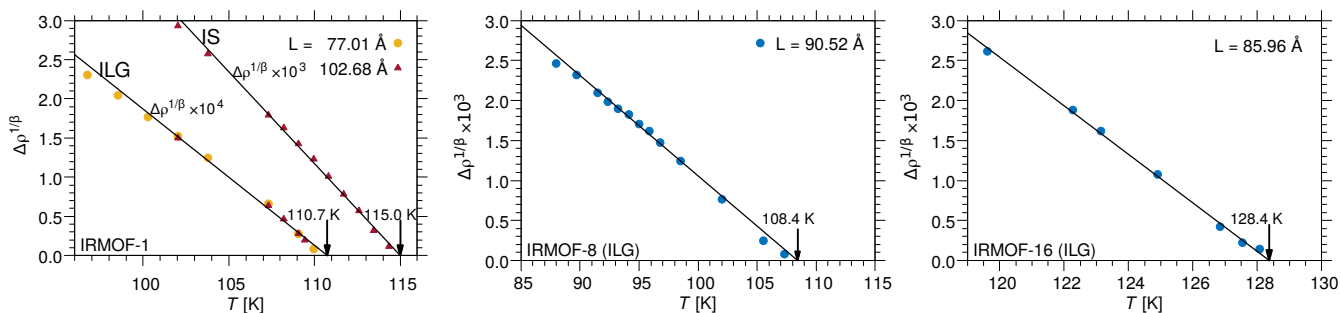
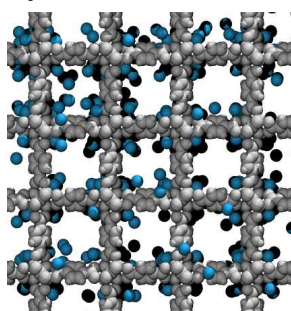
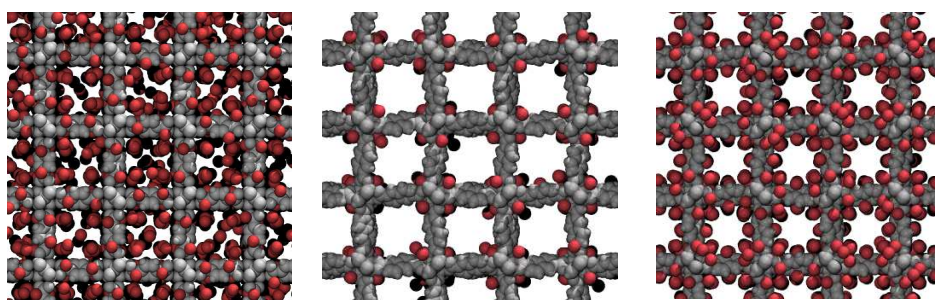


Figure 5.17: Order parameter scaling close to the critical points for the ILG phase transitions assuming 3D Ising universal scaling. The intersection with the abscissa determines the critical temperature.

a) IRMOF-1, 95K



b) IRMOF-8, 56K



c) IRMOF-16, 25K

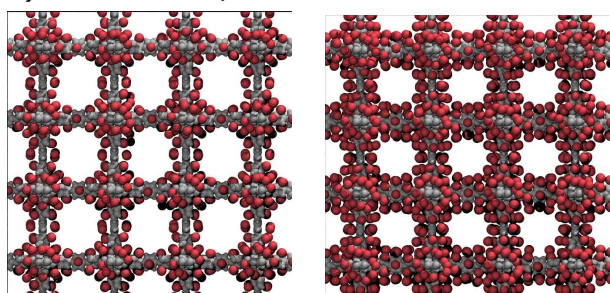


Figure 5.18: Snapshots of coexisting IS phases from a $4 \times 4 \times 4$ unit cells system at a) $N = 23$ and 130 (95.0 K) b) $N = 28$ and 163 (56.3 K) and c) $N = 281$ and 535 (24.6 K) methane particles per unit cell.

with the potential energy surface displayed in Figure 5.11, showing very deep potential energy “pockets” at these corners. In both MOFs this is connected with the first peak at distances 4 to 5 Å, visible the best at the lowest shown temperatures.

In the dense phase, methane covers the whole framework structure while leaving the pores mostly empty. While in IRMOF-1 a few particles⁵ can be found in the pore itself, in IRMOF-8 the pores are always empty in the dense IS phase – a result of the larger pores. Also, in IRMOF-8 the 2,6-NDC linkers (cf Figure 5.10) have a larger surface area allowing particles to form a wetting layer of larger area on the framework. The snapshots of the coexisting phases in Figure 5.18

5. In the dense IS phase there are ≈ 15 methane molecules around the metallic center at 95 K. The particle density per pore is $\approx 130/8 = 16.25$, thus finding particles outside the cutoff for the local order parameter z is very rare.

confirm these differences. In IRMOF-8 we also find an increased probability of finding methane particles at intermediate distances $8 < r < 9 \text{ \AA}$, which shows as a small peak in $g_{\text{met}}(r)$ in the dense phase, see Figure 5.19b.

At the critical point the coexisting phases must become identical, where the first peak is located at $4 < r < 5 \text{ \AA}$ in $g_{\text{met}}(r)$ and almost vanishes when approaching T_c . The second shoulder more pronounced making the $g_{\text{met}}(r)$ of the dilute phase more identical to the dense phase. Similarly, the peak in IRMOF-8 at $8 < r < 9 \text{ \AA}$ grows with higher temperatures in the dilute phase, while in the dense phase it becomes slightly smaller and both curves eventually follow the $g_{\text{met}}(r)$ which can be observed at the critical point (dashed green line in Figure 5.19a-b). In the case of the low-density phase transition in IRMOF-16 this picture is not as clear, as in the IS transitions of IRMOF-1 and -8: Since the density differences between the phases are very low, one can expect only very small differences in $g_{\text{met}}(r)$, as displayed in Figure 5.19c. Also, the very low temperatures of the transition cause a very high ordering of adsorbed molecules on the surface, as seen in Figure 5.18c. Whether these phases are crystalline and if there are even more transitions at higher densities has not been examined. While in the presented transition it seems that an additional layering around the metallic cluster of methane particles occurs in this transition, a more detailed analysis with larger system sizes would be required.

The local order parameter z introduced in the IS phase analysis in IRMOF-1, can be applied in the IRMOF-8 phases as well. There, we have chosen $r_{\text{cut}} = 7.0 \text{ \AA}$ as indicated in Figure 5.19., which is slightly smaller than for IRMOF-1, where $r_{\text{cut}} = 7.995 \text{ \AA}$. Therefore, the additional particles on the linkers at distances around $7.8 < r < 9.1 \text{ \AA}$ do not contribute to the local order parameter. Figure 5.20 proves that the local density can be mapped very well to the coordination of molecules around the corners of the framework, even though small corrections are expected, as a small amount of molecules present in the MOF do not contribute to z . The critical coordination number for IRMOF-8 is $z_c = 9.29$, very close to the value determined in IRMOF-1 with $z_c = 9.64$.

Adsorption isotherms From the probability distributions as shown in Figure 5.12 we determine adsorption isotherms as a function of the pressure. To do so, we reweight the histograms from coexistence conditions to a different chemical potential. We assume that the corrections to an ideal gas at these densities are small, and relate the chemical potential directly to the pressure of an ideal gas. In the work of [W. Zhou, Wu, Hartman, and Yildirim, \(2007\)](#) it was shown that the deviations in this pressure and temperature range are negligible. These equilibrium adsorption isotherms give predictions where to expect the phase transition in experiment. The first-order phase transitions are indicated by jumps in the adsorption isotherm if one plots the number of adsorbed particles as a function of pressure. Figures 5.21, 5.22 and 5.23 display this type of adsorption isotherm for IRMOF-1, -8, and -16,

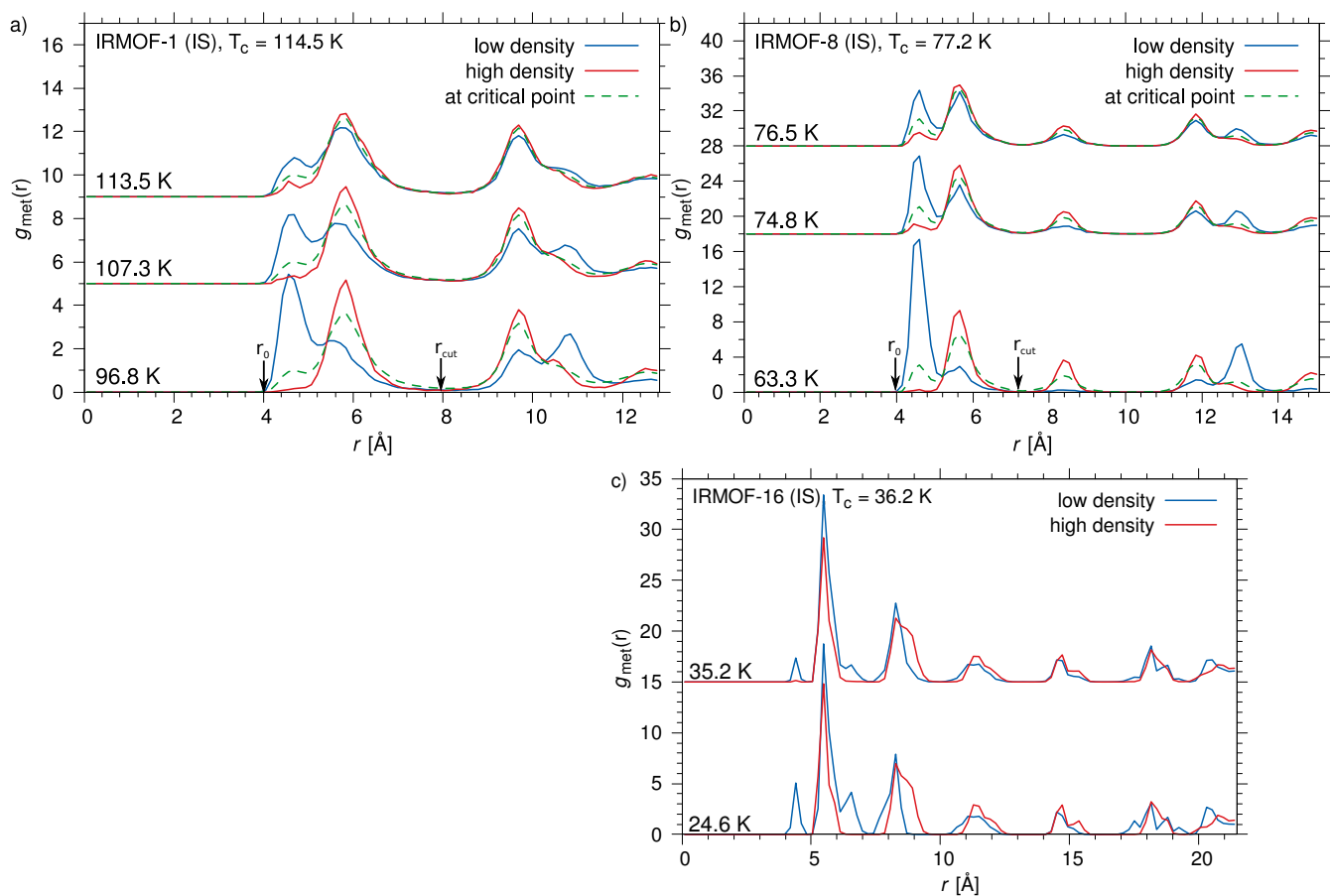


Figure 5.19: Radial distribution functions g_{met} for the IS transition of CH_4 in different IRMOFs. With increasing temperatures the ordering of methane molecules around the metallic clusters becomes more and more similar of the two phases.

respectively. While the information shown is very similar to that given from the coexistence lines in Figure 5.14, the adsorption isotherms are a typical property determined to characterize adsorption behavior in porous media in general. Different types of shapes are usually associated with the porous structure of the material, e.g. a two-step behavior is classified as an IUPAC *type IV* isotherm, see Chapter 1 (p. 1) which occurs in porous media with heterogeneous pore sizes which are filled with guest molecules at different pressures ranges. But here the double-step form of the adsorption isotherms is caused by the phase transitions instead – a very different phenomenon.

While in principle experimental adsorption isotherms can be determined also at very low pressures, they are often measured at standard conditions for temperature and pressure (STP, 273.15 K and 100 kPa)⁶, finding the IS and ILG phase transitions requires low pressures and temperatures, e.g. $P < 1 \times 10^2$ Pa and $T < 115$ K in the case of IRMOF-1 in order to observe the IS phase transitions. For IRMOF-8, these values are even lower and in IRMOF-16 it is unclear whether the IS transition exists at all (and thus the data is not shown in Figure 5.23).

6. Also, slight variations are common, too. E.g. normal temperature and pressure (NTP) with a temperature of 293.15 K and at a pressure of 1 atm = 101.325 kPa.

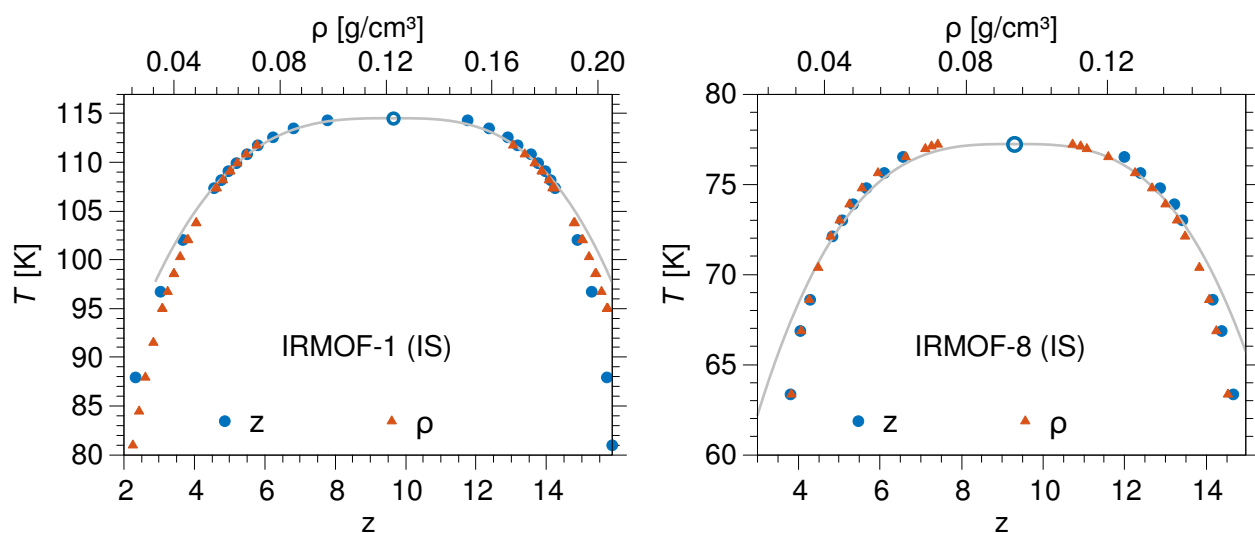


Figure 5.20: Coexistence lines of the IS transitions in the coordination–temperature plane. Grey line fits the data to the 3D Ising power-law behavior $\Delta\rho^\beta$.

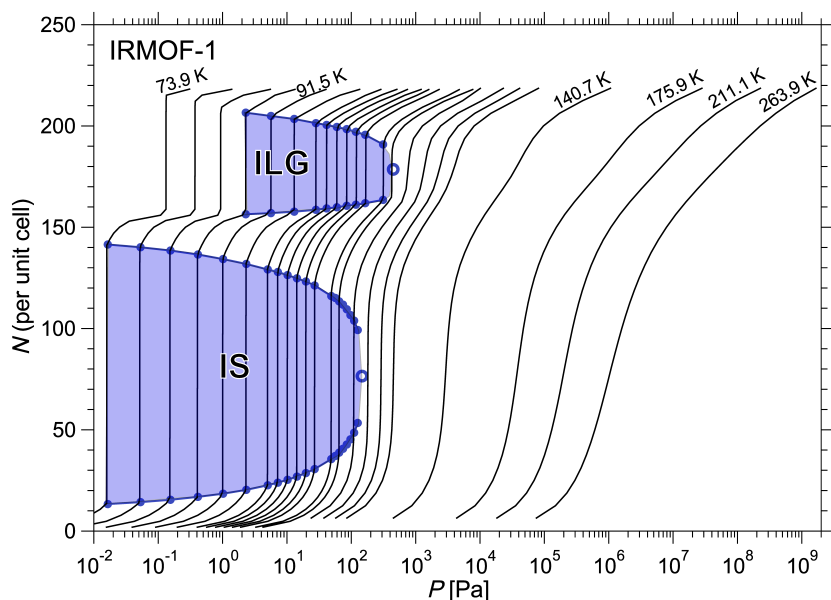


Figure 5.21: Equilibrium Adsorption isotherms for IRMOF-1 as a function of pressure from GCMC simulations for IRMOF-1. Colored areas indicate the two-phase regions of the phase transitions, critical points are shown as open symbols.

5.2.2 Conclusion

We have extended our study of the phase behavior of methane using grand canonical Monte Carlo simulation of a single MOF system, IRMOF-1, to two more representatives of the IRMOF-class: IRMOF-8 and -16. Both MOFs have larger pores than IRMOF-1 and tune the critical point of both condensation transitions. While the IS transition temperature is lowered with increasing pore size, for the ILG transition the critical temperature rises. Similar behavior is found

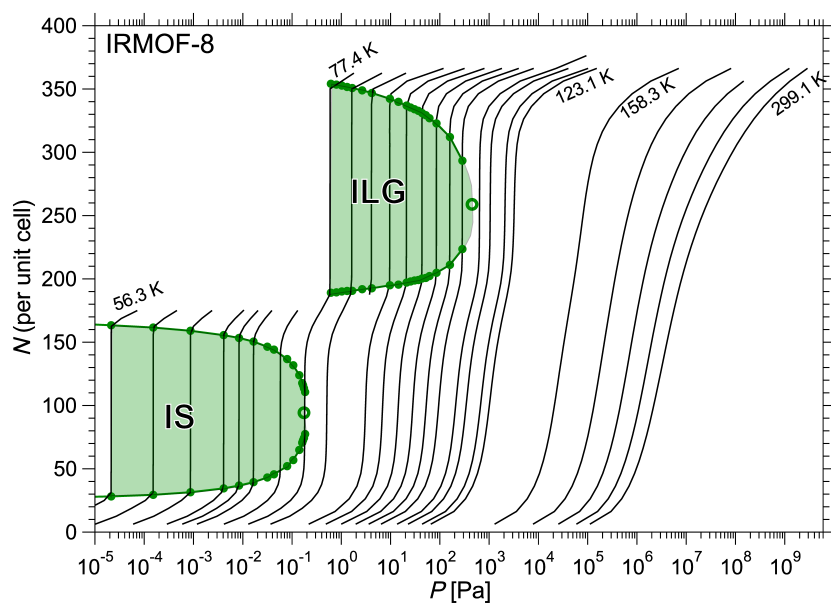


Figure 5.22: Adsorption isotherms as a function of pressure from for IRMOF-8 as determined by histogram reweighting of from probability distributions at coexistence conditions. Regions of phase coexistence are colored.

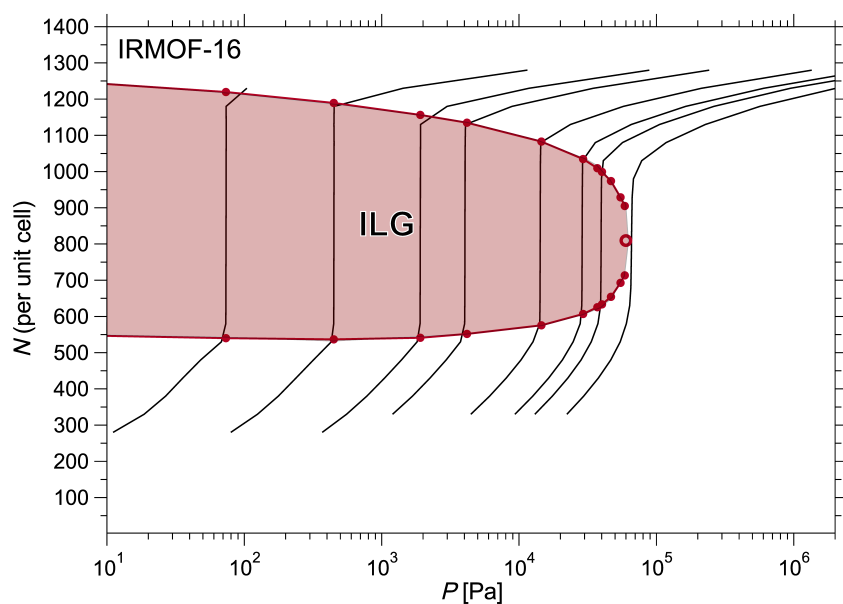


Figure 5.23: Adsorption isotherms as a function of pressure from equilibrium simulations for IRMOF-16 at coexistence conditions. Only ILG phase transition is shown, as the nature of the IS transition is unclear at this point.

for the coexistence density range. It becomes broader with increased pore volume for the ILG transition, and narrower for the IS transition. Consequently, the parameter range of the coexistence lines of both transitions diverges in MOFs with large free volume for the guest molecules. In IRMOF-1 the critical temperatures were only ≈ 4 K apart from each other, in IRMOF-8 the difference is 31 K. The appar-

ent critical temperature of the IS transition in IRMOF-16 is so low that we obtain crystalline-like condensation on the inner surface and further study is required to resolve the nature of the IS transition in IRMOF-16.

The IS phases of IRMOF-1 and -8 are very similar, allowing to apply the local order parameter introduced for the IRMOF-1 IS transition also for IRMOF-8. In both MOFs we can map the bulk density of the phases to a local coordination of particles around a metallic center.

Our analysis of the scaling behavior close to the critical points gives evidence that the universal behavior is unchanged and all phase transitions belong to the 3D Ising universality class – with the exception of the IS transition in IRMOF-16. We predict equilibrium adsorption isotherms for temperatures above the phase transitions and below. Both can be used to compare them to future experimental results. As we show in § 5.5 (p. 79) such experiments will require a careful sample preparation and measurement.

5.3 Structure and thermodynamic properties of interfaces

In § 5.1 (p. 45) the interface separating coexisting phases of the IS phase transition in IRMOF-1 has been identified as being two-dimensional and planar, and in this chapter interface properties of the IS phase transition in CH_4 IRMOF-1 and IRMOF-8 are discussed, particularly with regard to capillary wave theory. The simulations in this section have been performed by Mojtaba Eshraghi as part of his master thesis (Eshraghi, 2015).

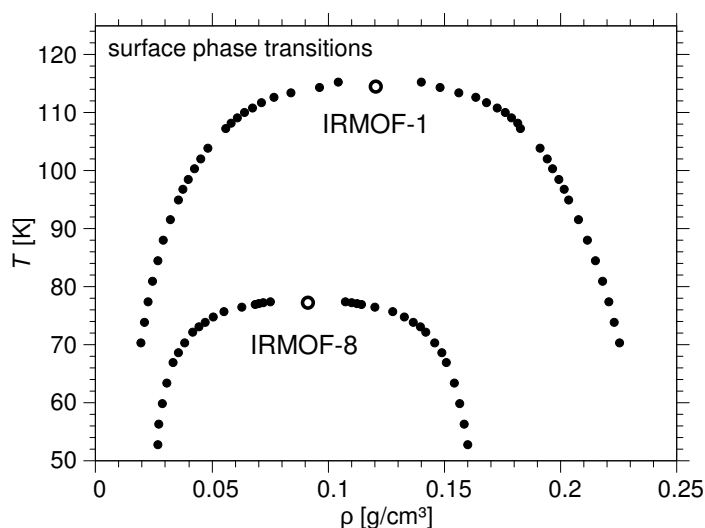


Figure 5.24: Coexistence temperatures of the IS transition of CH_4 in IRMOF-1 and IRMOF-8 as a function of the density. Critical points are shown as open symbols.

5.3.1 Methods

The simulation setup follows what has been done before to study the phase behavior of CH_4 in IRMOF-1: grand canonical Monte Carlo where temperature T , volume V and chemical potential μ are fixed, and the number of particles N is allowed to fluctuate. The phase diagram in Figure 5.24 displays the coexistence temperatures and density range of the IS phase transition.

Successive umbrella sampling allows for sampling equilibrium states in the two phase region where an interface is separating the two bulk phases. The access to equilibrium configurations in the two-phase region is crucial to study interface properties. However, instead of cubic simulation boxes, the geometry is of the form $L \times L \times L_z$ with $L_z > L$ and L, L_z being multiples of the unit cell edge length $L_{\text{IRMOF-1}}$ or $L_{\text{IRMOF-8}}$, with periodic boundary conditions applied in all spatial directions. This setup will create two interfaces perpendicular to the z direction, as the area of the interface will be minimized to minimize the free energy. Compared to cubic geometries, this has also the advantage that the interfaces are further apart and interactions between them can be avoided. Typical snapshots from such a simula-

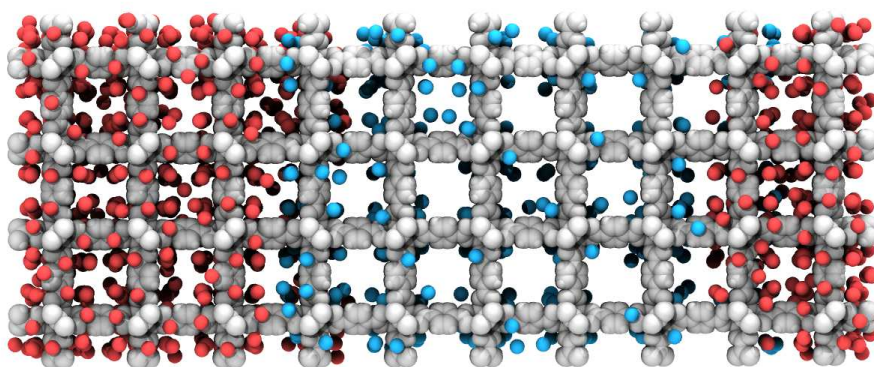


Figure 5.25: Snapshot of CH_4 in IRMOF-1 at coexistence conditions at 98.5 K with a density of 75 particles per unit cell of the IS phase transition. Colors determine the local phase of CH_4 , low density (blue) and high density (red) are determined from the local order parameter z .

tion are shown in Figure 5.25 (IRMOF-1) and Figure 5.28 (IRMOF-8). At temperatures below the critical temperature T_c , one will observe an interface separating the two bulk phases. The free energy cost ΔF to create the interface between two bulk phases is related to the interfacial tension γ via (Binder, 1982)

$$\gamma = \frac{\Delta F}{2A}, \quad (5.5)$$

where A is the area of the interface, hence in a system with periodic boundary conditions, two interfaces will form. ΔF can be obtained directly from the probability distribution (cf. Figure 5.26) by calculating the difference between the maxima (corresponding to the bulk phases) and minima (in the coexistence region) of the probability distribution $P(N)$, thus $\Delta F = \ln(P_{\min}) - \ln(P_{\max})$, see also Equation (4.20). Close to the critical point the interfacial tension is expected to scale with

$$\gamma \propto (T - T_c)^{2\nu}, \quad (5.6)$$

where the exponent $2\nu = 1.26$ corresponds to the 3D Ising behavior (cf. Table 3.1 (p. 22)). In § 5.1 (p. 45) we have already shown that the IS transition in fact belongs to this universality class.

5.3.2 Results

Using the scaling relation in Eq. (5.6) we can compare the critical temperatures determined from finite size scaling of Binder's cumulant (see § 5.1 (p. 45) and § 5.2 (p. 51)) of IRMOF-1 and IRMOF-8 to the scaling behavior of the interface tension γ . By plotting $\gamma^{1/2\nu}$ versus T , we obtain a straight line and the intersection of the extrapolated line with the abscissa yields T_c . The data presented in Figure 5.27 shows an excellent agreement with 3D Ising scaling for all tested system sizes and the critical points differ only $\approx 0.6\%$ for both IRMOF-1 and IRMOF-8⁷.

Since we have access to equilibrium configurations in phase separated states, in the following we can analyze the interface in detail.

7. For comparison, the critical temperatures for the IS transition as determined from finite size scaling are 114.5 K and 77.2 K for IRMOF-1 and -8, respectively.

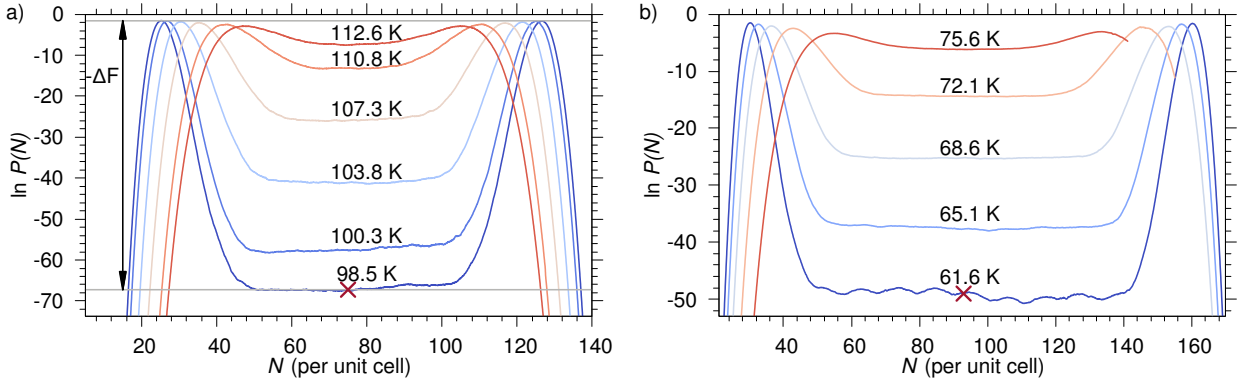


Figure 5.26: Logarithm of probability distributions for CH_4 in (a) IRMOF-1 and (b) IRMOF-8 for different temperatures at coexistence chemical potential of the IS phase transition as a function of the number of particles per unit cell N . Data from system sizes $3 \times 3 \times 6$ unit cells (IRMOF-1) and $2 \times 2 \times 6$ unit cells (IRMOF-8) is shown. As indicated by the arrow, the difference between the minimum plateau and the two maxima is related to the free energy cost for the interface $\Delta F = \ln(P_{\min}) - \ln(P_{\max})$.

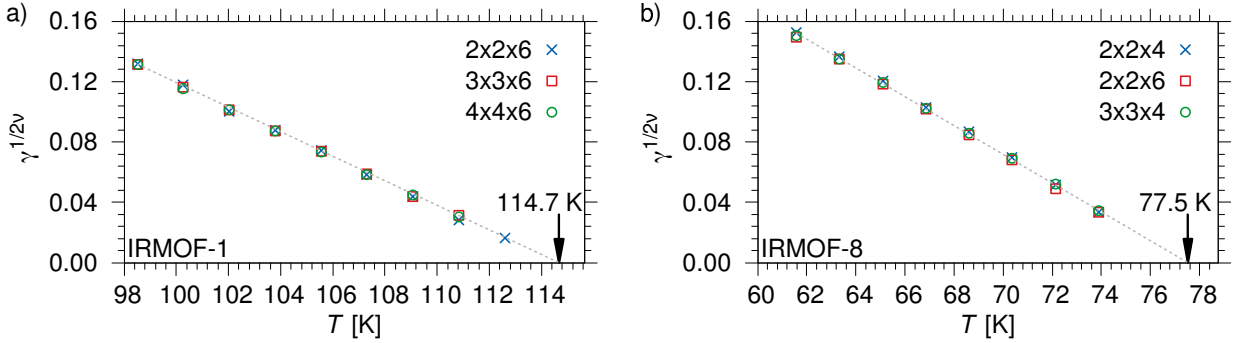


Figure 5.27: Scaling behavior of the interface tension γ close to the critical points of a) IRMOF-1 and b) IRMOF-8 for different system sizes (given in multiples of unit cells). A extrapolated linear fit yields the critical point for vanishing interface tension.

To do so, we chose a density where approximately half of the system volume is in the dilute phase and the other half is in the high density phase. This ensures that the two interfaces are separated by the largest possible distance and therefore minimizes interactions between interfaces. The selected densities are also tagged in the probability distribution in Figure 5.26. We average over 50 independent runs and align the interfaces by minimizing the correlation of the CH_4 density profiles $\rho(z)$. As the local methane density fluctuates strongly since the both phases form an inhomogeneous wetting layer on the framework surface, we apply a kernel density with a Gaussian kernel:

$$\rho(z) = \frac{1}{\sqrt{2\pi\sigma^2}} \sum_i \exp\left[-\frac{(z-z_i)^2}{2\sigma^2}\right], \quad (5.7)$$

where \sum_i denotes the sum over all particles i with their respective

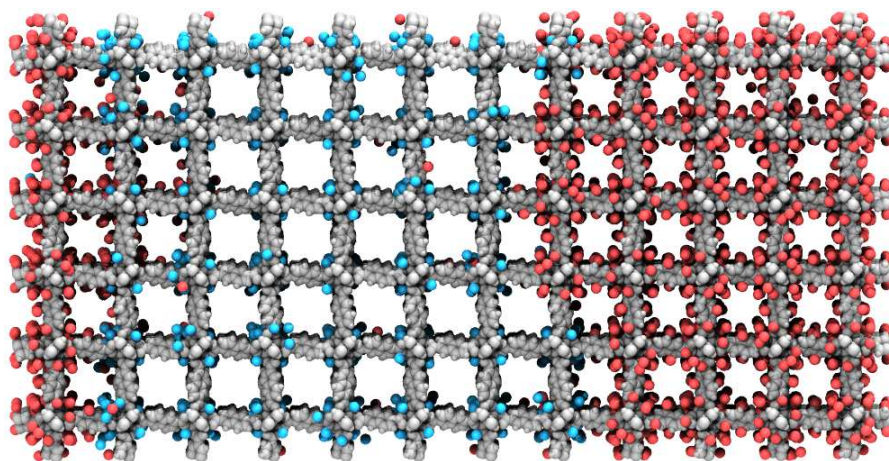


Figure 5.28: Snapshot of CH_4 in IRMOF-8 at coexistence conditions at 61.6 K with an average density of 93 particles per unit cell of the IS phase transition. Colors determine the local phase of CH_4 , low density (blue) and high density (red) are determined from the local order parameter z .

z -coordinate z_i ; the range parameter σ is chosen to be 1.37 \AA .

From the density profile one can assign a width w of the associated interface which is perpendicular to the z direction, by approximating the measured $\rho(z)$ to a hyperbolic tangent:

$$\hat{\rho}(z) = \frac{1}{2} \left[(\rho_h + \rho_l) + (\rho_h - \rho_l) \tanh \left(\frac{z - z_0}{2w} \right) \right], \quad (5.8)$$

where ρ_l and ρ_h are the densities of the dilute (l) and dense (h) phases on the binodal, respectively. The parameters ρ_l , ρ_h , z_0 and w are fitted by means of least squares. Eq. (5.8) originates from the result from the interface profile as found by mean-field theory (Gelfand and Fisher, 1990), where w is the intrinsic width. Even though this result is only valid very close to the critical point, the description of the interface shape works fairly well to assign a width to the interface even far away from criticality (Rozas and Horbach, 2011).

The density profile and the associated tanh-fit are displayed in Figure 5.29 and while for IRMOF-1 the fit shows excellent agreement with the measured density (ρ_l and ρ_h are in good agreement with the binodal of the phase diagram (cf. Figure 5.24 (p. 64)) and allows for a proper definition of the interface width, as expected. The density profile in IRMOF-8, as shown in Figure 5.29b illustrates the much stronger heterogeneity of the phases: The local density $\rho(z)$ oscillates much stronger in both bulk phases – even with the Gaussian kernel smoothing. The density maxima correspond to an increased probability of finding a metallic cluster at this distance to the interface, while minima indicate the presence of organic ligands. This behavior makes locating the interface more difficult and a hyperbolic tangent approximation is less sensitive as it is less clear whether a change in density is caused by the structure of the phase or by the presence of the interface. Also, the interface width is quite small, as coexistence temperatures are quite low, thus suppressing thermal fluctuations. Still, the bulk densities, as determined from Eq. (5.8), are in good agreement with

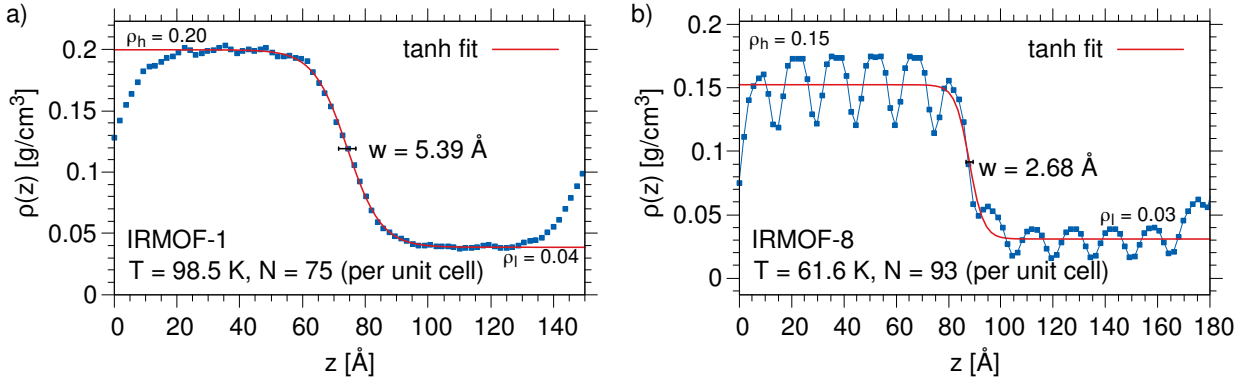


Figure 5.29: Averaged density profile for a) IRMOF-1 and b) IRMOF-8 as obtained from 75 independent runs in systems of $3 \times 3 \times 6$ unit cells. Periodic boundary conditions imply a second interface, which appears around $z = 0$ and $z = L_z$. The densities of the bulk phases ρ_l and ρ_h can be read off directly from the fit, as indicated in a).

8. The lever rule states that the fractions of each phase $x_\alpha = N_\alpha/N$ (N_α is the number of particles in phase α) are inversely proportional to the volumes they occupy:

$$\frac{x_1}{x_2} = \frac{V_2 - V}{V - V_1}. \quad (5.9)$$

the binodal of the IRMOF-8 IS transition. Further, the presence of these oscillations in the density profile also proves that the interface location is also partially imprinted from the external potential and cannot emerge on arbitrary locations.

With the lever rule (L. D. Landau and Lifshitz, 1980)⁸ we can also understand why oscillations occur in the probability distributions of IRMOF-8 at low temperatures (see Figure 5.26b) and certain states cost less free energy than others, depending on the density. Configurations with lower free energy cost ΔF are states where the interface is aligned with the framework, i.e. located in a plane where metallic centers are, too. The organic linkers occupy space (they are parallel to the interface), thus reducing the interface area and the free energy cost. When an interface is located in the whole pore, the linkers are perpendicular to the interface and therefore it must have a larger area and ΔF increases, too. With increasing system size we expect this effect to vanish, as this it is quite small and fluctuations in the interface will screen these oscillations.

For the local order parameter z_c , as defined in § 5.1 (p. 45), measuring the coordination around the metallic clusters of the IRMOF, shows a very similar behavior as the density profile $\rho(z)$ as shown in Figure 5.30a, yielding excellent agreement between the interface width from the density profile (5.39 Å from $\rho(z)$ vs. 5.46 Å from $z_c(z)$).

Similarly, to the power-law scaling of the interfacial tension in Eq. (5.6), we can test the scaling of the interfacial width as determined from the density and order parameter profiles, since w should be related to the correlation length ξ and diverge at T_c :

$$w(T) = w_0 \left(\frac{T}{T_c} - 1 \right)^{-\nu}, \quad \nu \approx 0.630, \quad (5.10)$$

with w_0 being a critical amplitude. If $w^{-1/\nu}$ is plotted versus the temperature, the dependence should become linear with $w^{-1/\nu}$ and vanish at T_c . We find indeed agreement with this scaling hypothesis

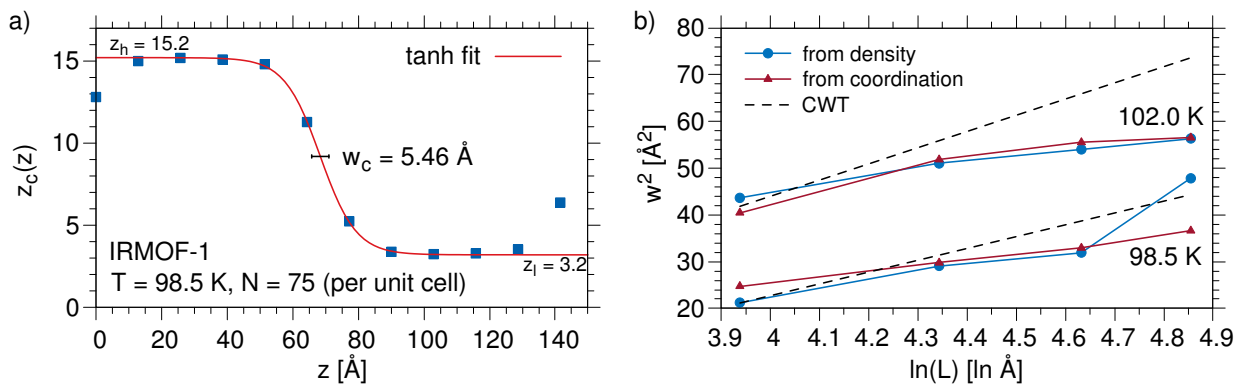


Figure 5.30: a) Averaged coordination number profile along the z axis for IRMOF-1 in a system of $3 \times 3 \times 6$ unit cells. Interface width broadening is shown in b), as determined from the coordination number (triangles) and density (circles) profiles and compared to the prediction of capillary wave theory (CWT, solid line). For visual clarity, data points for 102.0 K has been shifted by $+15 \text{ \AA}^2$ on the ordinate.

as shown in Figure 5.31. The critical temperatures are overestimated slightly, but inaccuracies are expected as this scaling is valid only very close to the critical point and for lower temperatures capillary wave fluctuations are large enough to screen the power-law scaling of the critical fluctuations.

In the IRMOF-8 system, on the other hand, the scaling works well even at lower temperatures, as thermal capillary fluctuations are more suppressed by the stronger interaction with the framework. Thus, the interface broadening is caused by the correlation length increase solely.

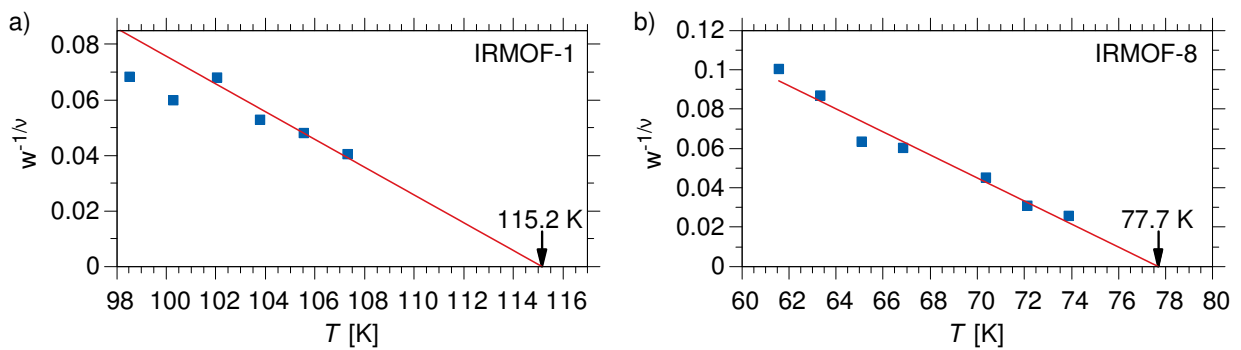


Figure 5.31: Interface width power-law behavior as a function of the temperatures for a) IRMOF-1 and b) IRMOF-8. For IRMOF-1, only temperatures above 101 K are taken into account for the fit, whereas for IRMOF-8 all displayed data points are used.

In the absence of external fields capillary wave theory (CWT) predicts a broadening of the interface width w with increasing lateral system size L (see also § 3.1 (p. 16) and [Brézin and Zinn-Justin, \(1985\)](#)

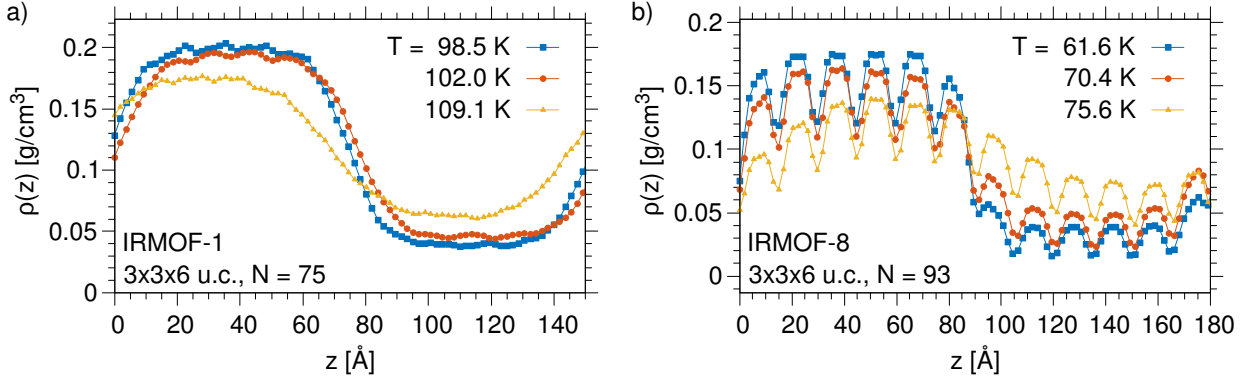


Figure 5.32: Density profiles $\rho(z)$ for different temperatures, but with same system size for a) IRMOF-1 and b) IRMOF-8.

and [Jasnow, \(1984\)](#)):

$$w^2 = w_0^2 + \frac{k_B T}{4\gamma} \ln L, \quad (5.11)$$

where γ is the interfacial tension and w_0^2 a squared intrinsic width. However, in the presence of an external field (e.g. gravitation), thermal fluctuation in the long-wave limit will be suppressed and w becomes finite in the thermodynamic limit ([Weeks, 1977](#); [Bedeaux and Weeks, 1985](#)). To understand whether interface broadening is inhibited by the presence of IRMOF, we plot w^2 as a function of the logarithm of the system size L in Figure 5.30b. For both temperatures, the broadening of the interfacial width is below the prediction of CWT as of Eq. (5.11), from which we conclude that the external field (i.e. the MOF) is suppressing thermal fluctuations. This is supported by the observation that in IRMOF-8 the interface width was not increasing with system size significantly (cf. Figure 5.33). In fact, for the two largest system sizes ($4 \times 4 \times 6$ and $5 \times 5 \times 6$ unit cells) no differences in the interface profiles are visible. Note that data for largest L in Figure 5.30b should be considered with caution, as in such systems the two interfaces in the system may interact with each other.

Further, the data in Figure 5.30a shows that both the width calculation using the density and from the local order parameter z_c , measuring the coordination of particles around metallic clusters, yield almost the same result, validating the choice of z_c as a suitable order parameter for the IS phase transition.

5.3.3 Conclusion

In conclusion, with the analysis of the interfaces in the IS phase transition we find an excellent agreement with 3D-Ising universal behavior by testing the scaling laws of the interfacial tension and interfacial width in the vicinity of the critical point – both in IRMOF-1 and IRMOF-8. We find an oscillation of the interfacial free energy in the parameter range where planar interfaces can be observed – a unique property related to the specific geometry and pore size

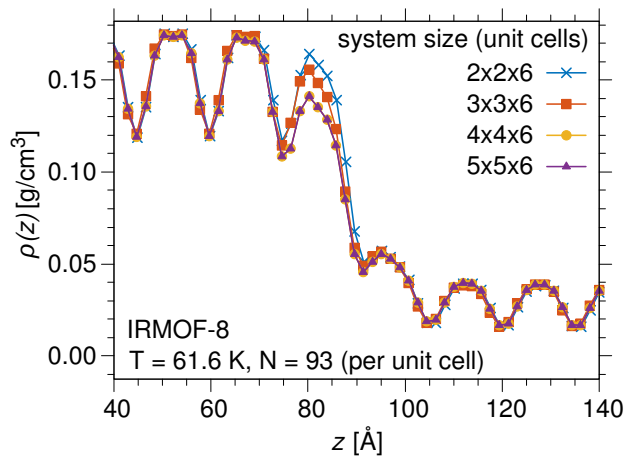


Figure 5.33: Density profiles for IRMOF for different interface areas, but with identical lateral sizes.

of IRMOF-8, and likely in others, too. The finite-size study of the interface width shows a suppression of capillary waves in IRMOF-1. In IRMOF-8, the interface broadening was almost completely absent, due to the low temperatures and high interfacial tensions in the IS transition.

5.4 Ising model for gas condensation in MOFs

5.4.1 Motivation and Model

In the previous sections, we analyzed the phase transitions of fluids in MOFs in detail, but computer simulations for large MOFs are still quite difficult, as it requires large particle numbers. Equilibration of the IRMOF systems with $4 \times 4 \times 4$ unit cells is about the upper bound in size that is viable to perform computations in a reasonable amount of time. Consequently, finite-size scaling analysis is limited to 4 system sizes at most (1^3 to 4^3 unit cells) – and for the smallest systems, strong corrections to finite-size scaling are expected (see § 4.4 (p. 37)).

Therefore, we seek a minimal model that is able to reproduce the phase transitions in IRMOFs, while reducing the computational load. Such a model should show the same scaling behavior and similar structures of the phases as those observed in IRMOFs. The Ising model we propose here, fulfills these requirements with respect to the ILG transition. The IS transition, however, is not included in this Ising model, yet. The computer simulations of the Ising model have been performed by Beatriz Seoane.

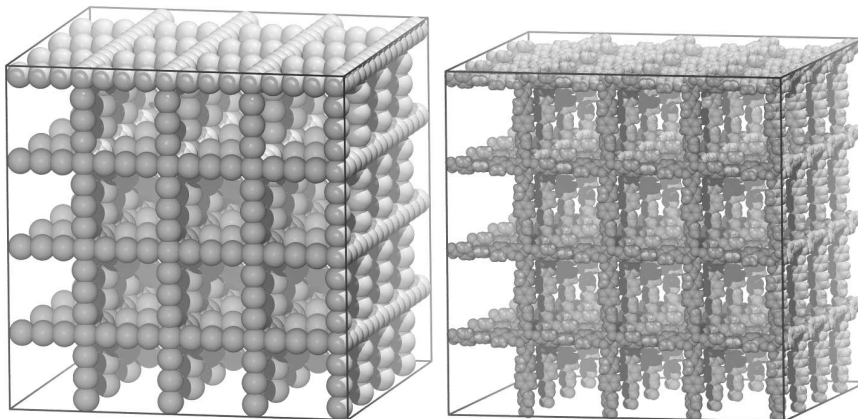


Figure 5.34: Porous networks of a) the Ising system showing the fixed spins only and b) IRMOF-16, the details of its structure can be found in § 5.2 (p. 51). A pore of the Ising model consists of 10 fixed spins, the IRMOF-16 framework pore has 113 atoms.

We consider an Ising system of N spins, with each spin i having the possible orientation $\sigma_i = \pm 1$, placed on a regular cubic lattice in a linear dimension L_{Is} with periodic boundary conditions applied in all spatial directions. We distinguish between two types of spins: free and fixed. While free spins can change their orientation, fixed spins are frozen into $\sigma = +1$ forming a framework structure mimicking the porous network of IRMOF, see Figure 5.34. Each spin is interacting with its nearest neighbors and with the externally applied magnetic field, H , described by the interaction strength h . Thus, the Hamiltonian of the Ising model reads

$$\mathcal{H} = -J \sum_{\langle i,j \rangle} \sigma_i \sigma_j - h \sum_{i=1}^N \sigma_i, \quad (5.12)$$

where $\sum_{\langle i,j \rangle}$ denotes the sum over all nearest neighbors pairs, where both fixed and free spins contribute to and J denotes the interaction strength between the spins. Therefore, the average magnetization over all spins m_{tot} can be written as

$$\begin{aligned} m_{\text{tot}} &= \frac{1}{N} \sum_{i=1}^N \sigma_i \\ &= \frac{1}{N_{\text{fixed}}} \sum_{\text{fixed}} \sigma_i + \underbrace{\frac{1}{N_{\text{free}}} \sum_{\text{free}} \sigma_i}_{\equiv m}, \end{aligned} \quad (5.13)$$

and thus it will always include a constant contribution from the fixed spins. Thus, in the following m determines the average magnetization of the free spins. The Ising model is simulated in the canonical ensemble at fixed temperature $k_B T = 1/\beta$, number of spins N and the volume V of the system. In a similar fashion to successive umbrella sampling (Virnao and M. Müller, 2004), we apply a biased sampling method, *tethered umbrella sampling*⁹, which allows for sampling states in the two-phase region far below the critical temperature, which are associated with large free energy barriers and therefore very low probabilities to visit such states using unbiased sampling schemes. The output of this simulation is very similar to the GCMC computer simulations of the IRMOF-system: We get a probability distribution $P(m)$ as a function of the magnetization of the free spins m . In the following, we consider only system with a pore size (periodicity) of the fixed spin framework of $p = 4$, i.e. every fourth spin we insert a parallel lines of fixed spins (cf. Figure 5.34a), resulting in 54 free spins per pore.

5.4.2 Results

Figure 5.36a displays the probability distribution at coexistence conditions for the Ising-MOF model. For values of magnetization between -0.2 to $+0.2$ we observe a flat plateau developing ripples for very low temperatures ($T \lesssim 3.23k_B J$). While a flat region in the free energy usually indicates a planar interface between the two phases, oscillations in ΔF suggest that the external field (and therefore the pores) influences the interface in a very similar fashion as observed in the IS transition as discussed in § 5.3 (p. 64).

For comparison, the probability distribution $P(N)$ of the ILG transition of CH_4 in IRMOF-16 as shown in Figure 5.36b show the same qualitative behavior as described above. Due to the smaller system size¹⁰ of the atomistic model the amplitude of the oscillations in the free energy is more pronounced as the increase of the interface area by misalignment to the framework structure has a larger contribution in smaller systems. To support this claim, in Figure 5.37 we plotted the probability distribution as a function of the order parameter at temperatures far away from the critical point for different system sizes. We have scaled the histograms with the area of the interface, L^2 (where L is L_{IS} or L_{IS} , depending on the system). We see two things in the

9. A detailed description of tethered umbrella sampling can be found in Fernandez, Martin-Mayor, and Yllanes, (2009), Martin-Mayor, Seoane, and Yllanes, (2011), and Fernandez, Martin-Mayor, Seoane, and Verrocchio, (2012).

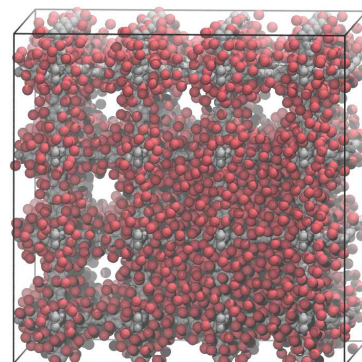


Figure 5.35: Liquid-gas coexistence of CH_4 in IRMOF-16, the interface aligns on the the framework structure preferably.

10. The largest IRMOF-16 system consists of $2 \times 2 \times 2$ unit cells, equating 64 pores, whereas in the largest Ising-MOF there are 64^3 pores.

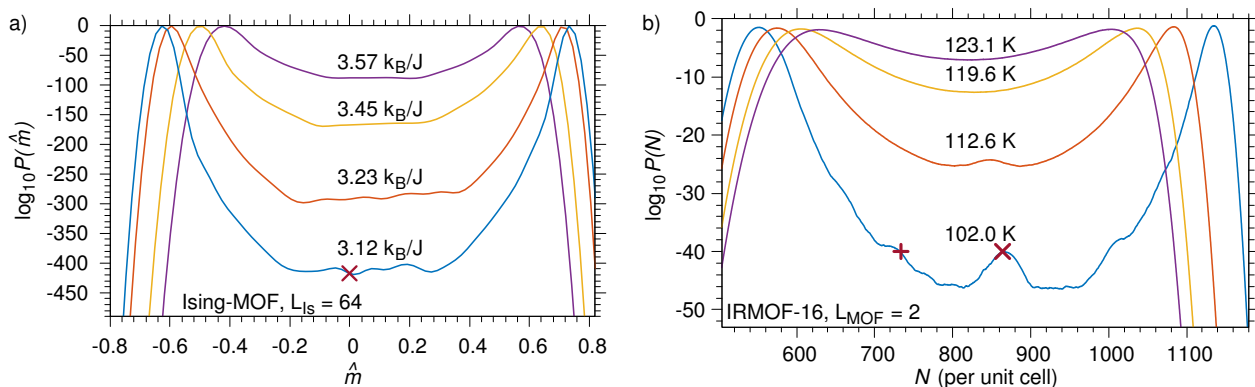


Figure 5.36: Probability distributions for a) Ising-MOF model and b) in IRMOF-16 model as determined from the largest available systems, as indicated by the edge lengths of cubic system sizes, L_{Is} and L_{MOF} . Red crosses (x) refer to the snapshots in Figure 5.38, the plus (+) symbol to the snapshot in Figure 5.35.

11. $\Delta F = \log(P_{\text{max}}) - \log(P_{\text{min}})$
the logarithmic difference between the maxima and minimum in the probability distribution

Ising and in the MOF models: a) The amplitude of the oscillations in interfacial tension $\gamma = \frac{\Delta F}{L^2}$ ¹¹ decrease with increasing system size. However, the number of maxima in the plateau of $P(m)$ increases. b) The scaling with the interfacial area works quite well. However, extrapolating a value for γ in the thermodynamic limit, γ_{∞} , is not possible in IRMOF-16, as $P(N)$ is subjected to too much noise. Nevertheless, in the Ising model we observe an increase in γ with L_{Is} . However, whether this rise in the interface tension is due to capillary waves should be examined in forthcoming studies.

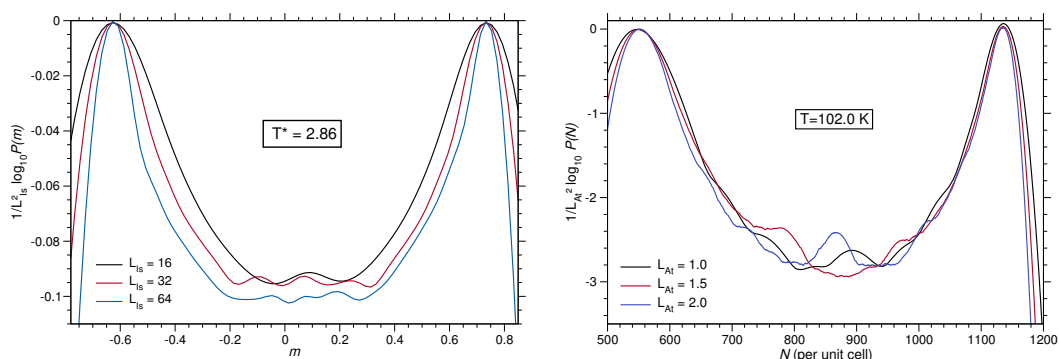


Figure 5.37: Semilogarithmic plots of the probability distributions for different system sizes scaled with $1/A$, with A being the area of the planar interface.

From the probability distributions one can directly extract the binodal of the phase transition – the first moment of each respective peak corresponds to the coexistence density. The phase diagrams in the magnetization–temperature plane – and density–temperature plane in the case of the atomistic model are shown in Figure 5.39. In this kind of framework confinement, both systems exhibit a very similar behavior, namely both critical temperatures are lowered with respect to the bulk phase behavior. Note that the critical temperature of the Ising system could potentially be tuned to match the behavior of bulk methane compared to methane in IRMOF-16. This could be accomplished by

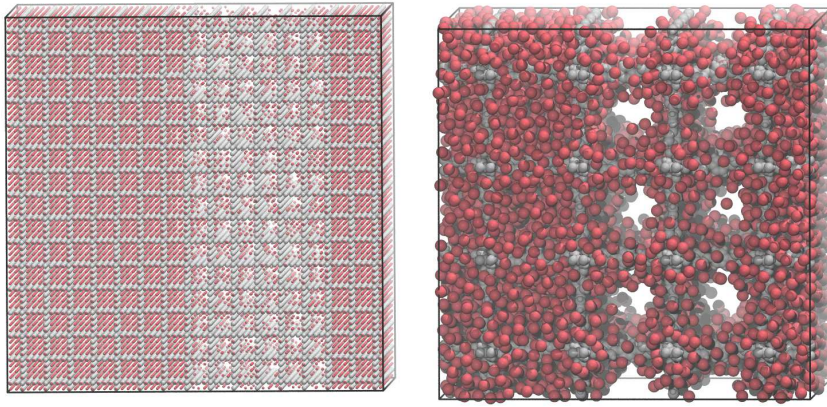


Figure 5.38: Configuration snapshots at coexistence conditions at for a) the Ising-MOF model at $T = 3.12k_B/J$, no magnetization ($m = 0$) showing spins with $\sigma = 1$ only (free spins in red, fixed framework spins in gray); and b) the IRMOF-16 model, at $T = 102.0$ K with $N = 864$ per unit cell. Red and gray spheres represent CH_4 molecules and framework atoms, respectively.

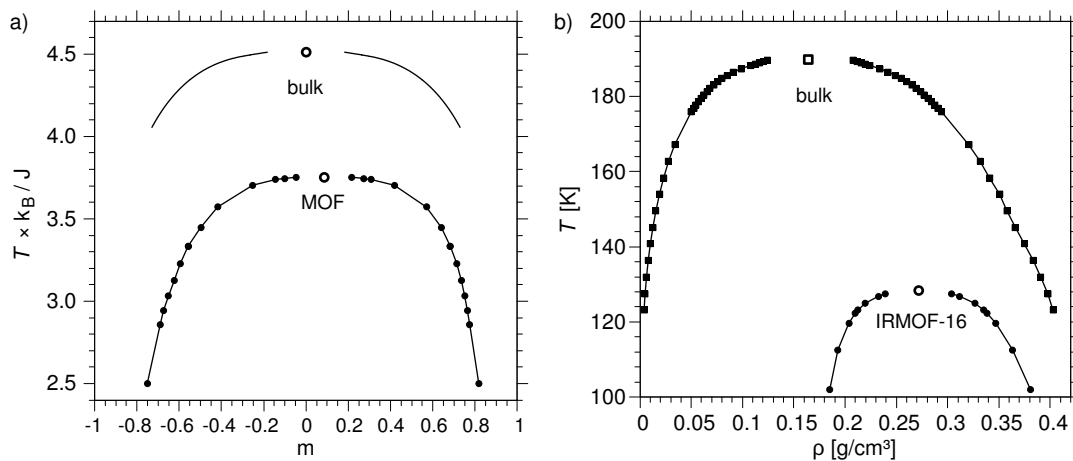


Figure 5.39: Phase diagram showing binodal lines of the a) the MOF-model in the Ising system and b) CH_4 in IRMOF-16, showing the ILG phase transition, each in comparison to the bulk phase behavior. Critical points are shown as open symbols.

varying the interaction of the free spins with the framework spins, by increasing its interaction range or -strength. The lowering of T_c is also known from other confinements, for example thin film systems (Fisher and Nakanishi, 1981). The shift of the critical point towards larger magnetization and higher densities can be easily explained by the attractiveness of the framework structure: In the Ising system (see also snapshots in Figure 5.38) free spins interacting with framework spins likely align to the framework spins, thus lowering the average free energy per spin, decreasing T_c and shifting the critical magnetization m_c . In the atomistic system the argument analogous, but there we have a shift in the critical density instead of a magnetization.

The two-phase region is also narrower with the presence of the framework structure, also being in accordance found in thin films

confinements. However, in thin films a crossover from 3D to 2D-Ising scaling behavior close to the critical point is observed (Nakanishi and Fisher, 1982). Such a cross-over is absent, as finite-size scaling of the Binder cumulant U_L – displayed in Figure 5.40 – shows. For all measured system sizes no indication of a cross-over in the universality has been observed, both in the Ising spin and in the atomistic IRMOF system. Due to the large computational effort of the GCMC simulation of the IRMOF-system the Ising model aids by allowing to determine a much higher accuracy of critical exponents, as finite-size scaling can span a much larger range of system sizes. The list of calculated exponents and critical values can be found in Table 5.2.

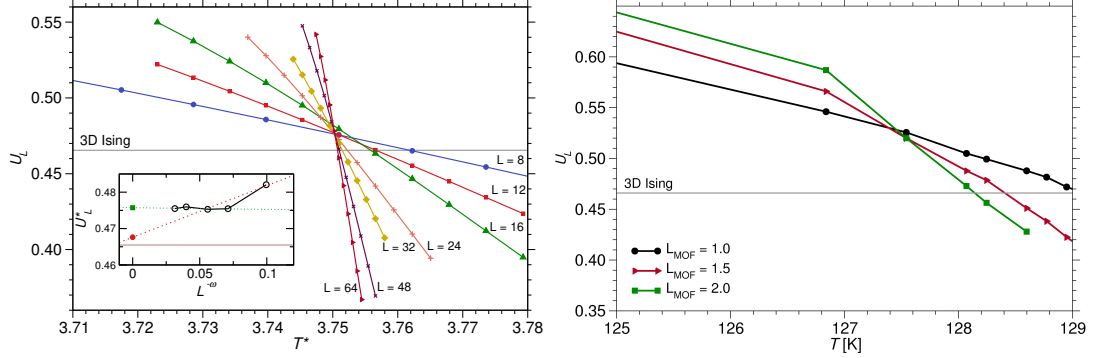


Figure 5.40: a) Binder's cumulant U_L for the Ising-MOF system for different system sizes L close to the critical temperature. The inset shows the intersection value of U_L , U_L^* , as a function of system size and fits extrapolating U_L to $L \rightarrow \infty$ using a linear function (red) and a constant (green). The figure in b) shows the same cumulant for IRMOF-16. 3D Ising universal values of $U_L^* \approx 0.465$ are included as indicated.

| | bulk | Ising framework model | | |
|----------------------|---------------|-----------------------|----------------|------------------|
| | | $J = 1, P = 4$ | $J = 1, P = 8$ | $J = 0.1, P = 4$ |
| β_{sim} | | 0.2666 | 0.2339 | 0.2564 |
| β_c | 0.22165463(8) | 0.266 642(7) | 0.233 961(6) | 0.256 359(5) |
| h_c | 0 | -0.563 515(2) | -0.114 187(5) | -0.056 657 2(7) |
| ν | 0.63002(10) | 0.629(9) | 0.629(5) | 0.628(5) |
| η | 0.03627(10) | 0.027(14) | 0.03(3) | 0.04(7) |
| $(\Sigma L^2)^*$ | — | 1.57(3) | 1.58(8) | 1.600(19) |
| U_L^* | 0.465477(3) | 0.468(3) | 0.4673(19) | 0.471(6) |

Table 5.2: Extrapolation of the critical points and exponents to the thermodynamical limit for the three models studied. The L -dependent value $\beta_c^{(L)}$ and $(\Sigma L^2)^{(L)}$ are obtained from the crossing point between the curves $\Sigma L^2(\beta)$ for L and $2L$, $\nu^{(L)}$ and $\eta^{(L)}$ from the derivatives of $\Sigma L^2(\beta)$ and $\Delta m(\beta)$ with respect to β at that point. $U_L^{(L)}$ and $h_c^{(L)}$ are interpolated from each respective curves with β at $\beta_c^{(L)}$. For the extrapolations $L \rightarrow \infty$, we consider a linear function $a + bx$ where $x = L^{-\omega}$ for ν , η , $(\Sigma L^2)^*$ and U_L^* ; $x = L^{-\omega+1/\nu}$ for β_c ; $x = L^{-\beta/\nu-D}$ for h_c , using the exponents ω, ν, β taken from Hasenbusch, (2010).

As corrections due to the finite system size are expected and we

have access to a larger number of system sizes in the Ising model, we can extrapolate U_L^* to the thermodynamic limit $L \rightarrow \infty$. Plotting $U_{L_i}^*$, as a function of $L^{-\omega}$ and extrapolating this using a linear approximation via $U_L^*(x = L^{-\omega}) = mx + c$ by fitting the parameters m and c . Such extrapolation can be found in the inset of Figure 5.40a, also including an extrapolation using a constant, as it appears to work equally well. In both cases we observe a deviation to U_L^* as obtained by [Hasenbusch, \(2010\)](#) for the 3D Ising universality class, which allows us to conclude the external framework potential introduces (small) corrections to U_L^* compared to the bulk system.

In addition to the main model we presented, we calculated the critical values and exponents for modified versions of the Ising-MOF model, one with doubled periodicity P and with decreased spin-spin coupling constant J . The results are also shown in Table 5.2. As expected, in both cases the phase behavior becomes more bulk-like with respect to the critical temperature shift and the external field at the critical point, h_c .

5.4.3 Conclusion

In conclusion, we have found a minimal model reproducing the phase behavior of the ILG transition as found in IRMOF-systems. The proposed Ising model finds a heterogeneous phase corresponding to the low-density (gas-like) phase of the IRMOF-system, which can be in coexistence with a homogeneous phase – which is the analogue to the liquid phase from the atomistic model. Further, our Ising-framework model is able to mimic scaling behavior, the universality class, and effects of the interface behavior caused by geometric constraints as found in IRMOF-16. On the other hand, the Ising-framework model can be refined in order to include the IS-phase transition by tuning the interaction with the framework spins. The introduction of heterogeneity in the surface of the framework would be one possibility – as it is the case in IRMOF-systems, see Figure 5.41. Further, the interaction range of the framework spins could be increased to enhance the effect of the framework while maintaining the pore size.

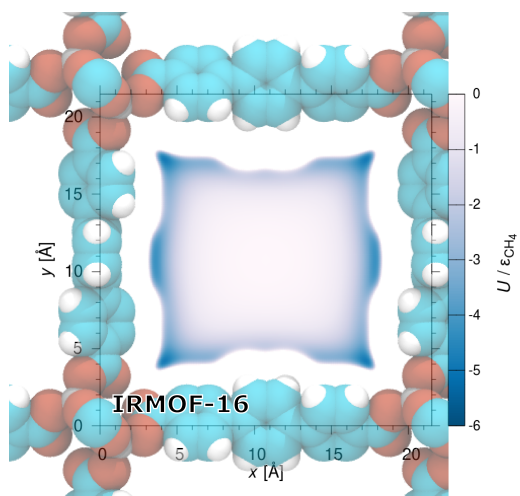


Figure 5.41: Potential energy as a function of the position in the plane of linkers and metallic centers in a single pore of IRMOF-16. Negative values of the potential energy U correspond to attractive interactions, potential energies ≥ 0 are shown in white. Approximate framework atoms positions as indicated.

5.5 Adsorption kinetics and diffusion dynamics

With the exploration of the phase behavior of Methane in IRMOFs it seems natural to expand the question from static, in-crystal behavior to an understanding of kinetics of light gases in presence of metal–organic frameworks: How are the gas particle adsorbed and which mechanics are important for an effective gas storage and is the heterogeneity of the framework affecting transport processes inside the porous structure? Understanding the kinetics in MOFs is also relevant in order to understand charging and uncharging processes for effective gas storage. Further, the mobility of particles plays an important role in the separation of gas mixtures (Wesselingh and Krishna, 2000; J.-R. Li, Kuppler, and H.-C. Zhou, 2009). A number of computational studies have been conducted on the kinetic behavior of gases in metal–organic frameworks (e.g. Skoulidas and Sholl, (2005) and Kundu, Pascal, Prendergast, and Whitelam, (2016)). However, in these studies the effect of phase transitions of the fluid on the kinetics was not considered, as they were unknown and measured at temperatures and densities far away from the phase transitions.

To investigate the effect of the IS transition on the kinetics, we applied molecular dynamics simulations to the same IRMOF model that is used in the grand canonical Monte Carlo simulations (Sections 5.1–5.4). In the second part of this section we study the influence of liquid–gas transition on the adsorption behavior

5.5.1 Transport in “pure phases”

Transport properties of light gases in MOFs have been studied already previously (e.g. by Skoulidas and Sholl, (2005)), but were typically determined at temperatures around room temperature. With the knowledge about the IS and ILG phase transitions in IRMOF-1 as shown in § 5.1 (p. 45), it is unclear if the coexisting phases show different transport properties. With the finding of new critical points in IRMOF-1, critical dynamical behavior (e.g. critical slowing down) can be studied using molecular dynamics computer simulations.

Methods

The start configurations for the molecular dynamics (MD) simulations were generated from GCMC simulations at the required point in the phase diagram (i.e. with a fixed density and temperature T). We use 10 independent configurations for subsequent thermalisation in MD simulations. The average internal energy of all configurations in the thermalisation is then used as initial total energy for subsequent microcanonical measurement runs. Two sets of measurements are applied, both exploring the kinetic behavior of the IS phases of CH_4 in IRMOF-1. One part is to compare diffusivities along the low- and high-density branches of the binodal in the IS transition (cf. Figure 5.4 (p. 47)). Additionally, we determine the kinetic behavior of in the vicinity of the critical point. Here, at the critical point with $\rho = \rho_c^{\text{IS}}$

12. τ is the natural time unit for Lennard-Jones interactions and is given by $\tau = \sqrt{m\sigma^2/\epsilon}$. For CH_4
 $\tau = 3.0314 \times 10^{-12}$ s.

and $T = T_c^{\text{IS}}$ starting configurations will be generated from GCMC and thermalised within MD simulations at temperatures $T \in [1.0 \times T_c^{\text{IS}}, 1.1 \times T_c^{\text{IS}}]$ for system sizes of $4 \times 4 \times 4$ and $6 \times 6 \times 6$ IRMOF-1 unit cells, followed by measurements up to $5000\tau^{12}$. In both cases we have set the density to the critical density $\rho_c = 0.12 \text{ g/cm}^3$, corresponding to $N = 4896$ and 16522 methane particles in the system, respectively.

To accelerate computer simulations for large systems and improve statistics of the measurements, MD simulations have been computed using GPU code with the HALMD simulation package by Colberg and Höfling, (2011) and available on <http://halmd.org>. Compared to the GCMC simulations, the MD simulations do not interpolate the MOF-guest interaction. Our benchmarks have shown that the GPU code is much faster in calculating the interaction of methane molecules with the IRMOF atoms (which are fixed in position) during the simulation. To verify, that both methods do sample equivalent equilibrium states, we have compared the radial distribution of methane particles around the metallic clusters, $g_{\text{met}}(r)$. For 70 K the comparison of $g_{\text{met}}(r)$ from GCMC and MD simulations is shown in Figure 5.42. In the low density phase there are only small deviations between MD and GCMC simulations and at the high density phase the structure is virtually identical, validating that both methods yield the same phases. In the

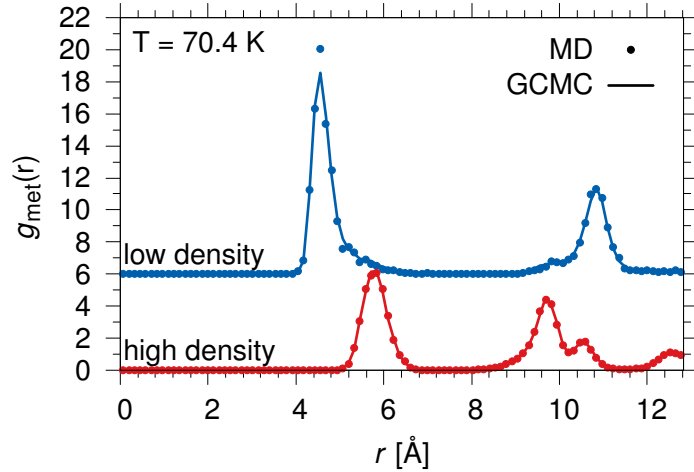


Figure 5.42: Radial distribution functions of methane particles as a function of the distance to the center of metallic cluster in IRMOF-1 of the coexisting IS phase at 70.4 K. The differences in the obtained equilibrium configurations, determined molecular dynamics (MD) and grand canonical Monte Carlo computer simulations are almost identical.

MOF one can define an interdiffusion coefficient, describing the mass transport of methane relative to the framework atoms.

Analogous to the interdiffusion in a binary mixture as outlined in § 4.5.1 (p. 39), we can determine the interdiffusion coefficient D_{int} for the sorbate particles similar as outlined in Maginn, Bell, and Theodorou, (1993) for interdiffusion in zeolites,

$$D_{\text{int}} = \lim_{t \rightarrow \infty} \phi \frac{N}{6t} \langle [\mathbf{r}_{\text{cm}}(t) - \mathbf{r}_{\text{cm}}(0)]^2 \rangle, \quad (5.14)$$

where $\mathbf{r}_{\text{cm}}(t)$ is the center of mass of the methane molecules at time t , N the total number of sorbate atoms, and ϕ a temperature-dependent thermodynamic factor. In binary mixtures, theories predict a power-law behavior of the interdiffusion coefficient close to the critical point of demixing T_c (Bhattacharjee and Ferrell, 1981),

$$D_{\text{int}} \propto \left(\frac{T - T_c}{T_c} \right)^{\chi_{\text{eff}}}, \quad (5.15)$$

with the effective exponent χ_{eff} . A similar behavior as been found in computer simulations (Das, Horbach, et al., 2006; Roy, Dietrich, and Höfling, 2016). Note that the measurement of D_{int} from computer simulations is rather noisy compared to the self diffusion constant D_s , as in a single system there is no averaging over independent particles in D_{int} .

Results

The mean-squared displacement (MSD) determined from our simulations are shown in Figure 5.43a and they show that the single-particle motion is ballistic for very short times and become diffusive around 10 ns. While the motion in the low density phase is slightly faster, its diffusion coefficients D are very similar to the denser phase where the wetting layer covers the whole framework, as shown in Figure 5.43b. But a remarkable difference between the kinetic behavior is in the intermediate time regime of 10^{-3} to 10^{-2} ns, especially at lower temperatures: In the high density phase small oscillations appear within that time regime the MSD is constant or increasing only very little. This can be interpreted as a kind of caging and back scattering (a lowering of the MSD means the particle comes back to its original position again) at time scales where particles have traveled approximately 1.0 \AA (the diameter of a Methane molecule is 3.73 \AA). This could be understood by the following picture: Particles are distributed almost on the surface only – and in fact quite densely. When the particle diffuses away from a location on the framework, it will do so on the inner surface of the framework (the pores are mostly empty in the IS high density states) and scatter back and forth until the particle escapes this cage. For long times, a diffusive behavior is obtained again. At higher temperatures the caging effect smears out as particles can diffuse more easily into the pores and therefore may avoid further collisions with other particles.

Additionally, we have also measured diffusion and interdiffusion coefficients close to the critical point of the IS transition. To determine a possible size-dependent diffusion behavior, we tested two system sizes, $4 \times 4 \times 4$ and $6 \times 6 \times 6$ unit cells. Equilibrium configurations have been generated in the same manner as explained above.

Due to the small temperature differences, the mean-squared displacements are very similar both for interdiffusion and single-particle diffusion (cf. Figure 5.45a). However, the associated inter- and self-diffusion coefficients $D(T)$ increase (as expected) with temperature, finite size effects are absent, also close to the critical point. This is

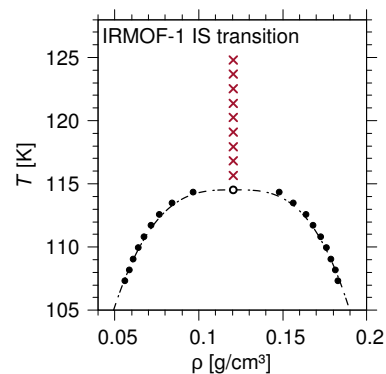


Figure 5.44: The coexistence line (dashed line fits the data points according to 3D Ising universality) of the IRMOF-1 IS transition including the points of diffusion and interdiffusion measurements (red crosses).

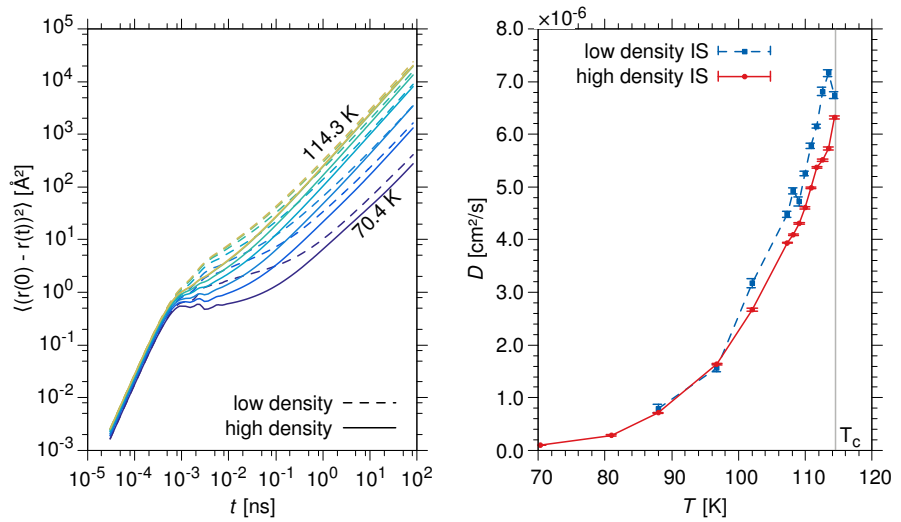


Figure 5.43: Mean-squared displacement (left) and diffusion coefficients (right) for Methane in $4 \times 4 \times 4$ unit cells of IRMOF-1 along the bindoal of the IS phase transition. Low density curves are shown as dashed lines, high density states are solid lines.

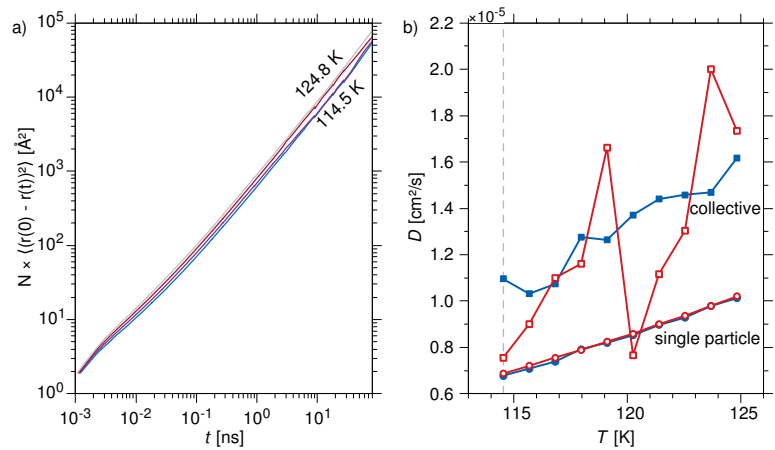


Figure 5.45: a) Mean-squared displacement of the diffusion of the center of mass for temperatures above the critical point. b) Diffusion coefficients for single particle diffusion (circles) and the diffusion of the center of mass (squares) in IRMOF-1 for temperatures close to the critical point of the IRMOF-1 IS phase transition with $T_c = 114.5$ K and $\rho_c = 0.12$ g/cm³. Open symbols with data from systems with $6 \times 6 \times 6$ unit cells, filled symbols from $4 \times 4 \times 4$ unit cells.

consistent with results obtained in previous simulation studies at the critical point in binary mixtures (Das, Horbach, et al., 2006). Yet, the behavior of the interdiffusion coefficient close to T_c is subject to large noise, which increases for the larger system, inhibiting a study of power-law behavior of the interdiffusion coefficients.

The numerical values for D are lower compared to the values determined from pulsed field gradient NMR experiments where $D = 1.9 \times 10^{-3}$ cm²/s at 173 K was reported (Stallmach, Gröger, et al., 2006). This discrepancy might be caused by the higher temperature in the experiment and by the different loading of methane particles in the MOF. Additionally, in the experiment intercrystalline diffu-

sion of molecules is taken into account, too. It is also unclear if the measurements have been realized at equilibrium conditions, as the adsorption kinetics into the MOF can be slowed down by nucleation effect significantly, as shown in the next section.

5.5.2 Adsorption kinetics

As the phase diagram in Figure 5.4 (p. 47) shows, the temperature and pressures of the IS and ILG two-phase regions are below the liquid–gas coexistence regions of bulk CH_4 . This is important to know for a full understanding of the adsorption kinetics and the interpretation of results from adsorption measurements in experiments. The phase behavior of the bulk gas which is supposed to be adsorbed by the MOF may play a crucial role for charging and uncharging kinetics of MOFs.

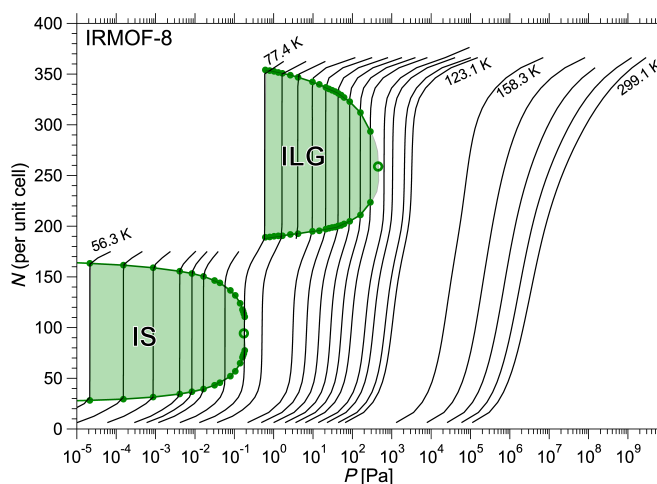


Figure 5.46: Equilibrium Adsorption isotherms of CH_4 in IRMOF-8 from computer simulations.

In cooperation with the Chemical Department at the Heinrich-Heine-University in Düsseldorf, we have determined the adsorption isotherms of methane in IRMOF-8 from volumetric adsorption experiments at room temperature and temperatures around as well as below the critical temperature of bulk methane (190 K). The prediction for the equilibrium sorption isotherms from GCMC simulations at these temperatures are do not show peculiar behavior (see also Figure 5.46). However, in the experiment, we observe a strong hysteresis for $T < T_c$ between adsorption and desorption, see Figure 5.47a, which is more pronounced, the lower the temperature becomes. The pressure region where we this hysteresis is obtained about two orders of magnitude lower than the pressure of the coexistence line. For reference, the pressure is marked in Figure 5.47b. The temperature region is far above the IS and ILG phase transition, thus the hysteresis must originate from other effects. Also, the adsorption curve is above the desorption curve – different from what is usually measured in MOFs, where particles are stuck in the pores and desorption becomes a very slow process. The experimental data lacks microscopic information for an interpretation of the presented data. In this section we study the adsorption kinetics of gas particles with computer simulations by placing a single IRMOF-1 grain and surround it by methane. By compressing and expanding the system (excluding the grain) we are able to study the

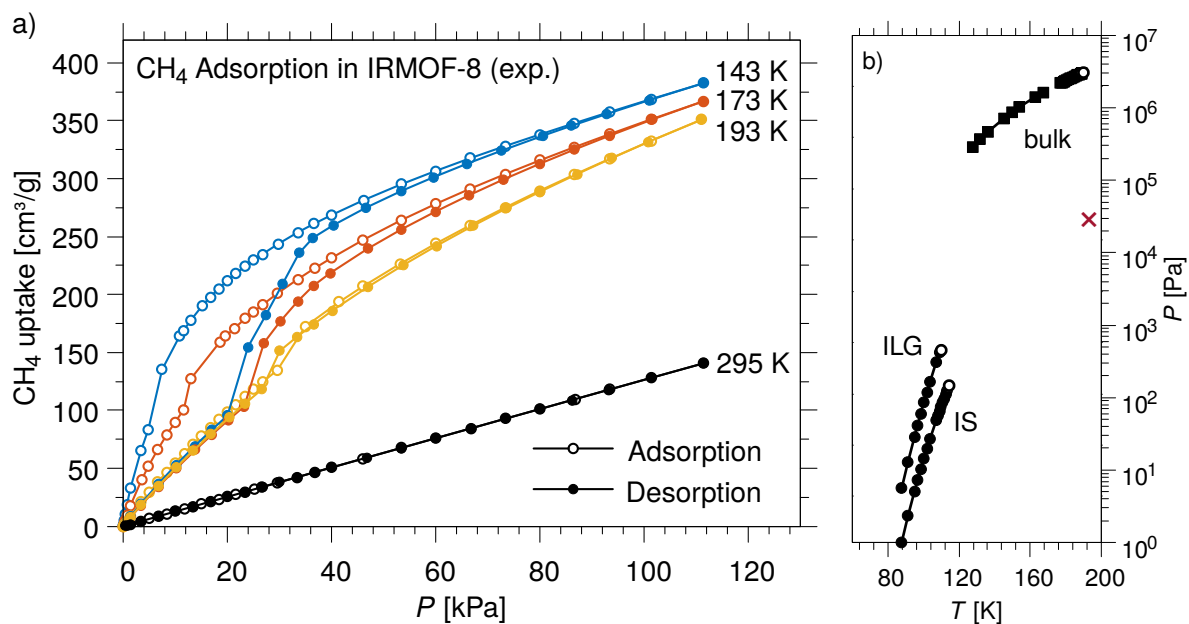


Figure 5.47: a) Experimental data from adsorption experiments of methane in IRMOF-8. The point where the hysteresis is observed at 193 K, ≈ 32 kPa, is marked in the phase diagram of IRMOF-1 and bulk CH_4 (b) with a cross.

adsorption behavior as a function of pressure and with the analysis of equilibrium configurations we expect to understand the inverse hysteresis effect that are observed in experiment.

Computational methods

The simulation samples are prepared as follows and illustrated in Figure 5.49: We place a IRMOF-1 seed of the size $3 \times 3 \times 3$ unit cells in the center of the simulation domain. The simulation box itself is larger than the MOF and the free volume outside the MOF is filled with methane particles using GCMC insertions and removal trials. Molecular dynamics simulations are then used to equilibrate the outer part with the MOF seed until the number of particles and pressure stabilize both inside and outside the MOF. The temperature is kept constant throughout the simulation by resampling velocities according to a Boltzmann distribution yielding the targeted temperature every n_B time steps. Temperatures chosen for the simulations were 263.9, 189.8 and 167.1 K, the first one being close to the bulk critical point of methane (190.0 K), the latter temperature is far below the critical point and the influence of bulk condensation should play an important role. Finding the pressure of a system the presence of an arbitrary external field is not easily possible in computer simulations (see also [Varnik, Baschnagel, and Binder, \(2000\)](#)), the pressure is determined from the particles outside the MOF, since equilibrium requires the intensive variables to be equal in the whole system. The bulk pressure P is determined from computer simulations via the relation ([Hansen and](#)

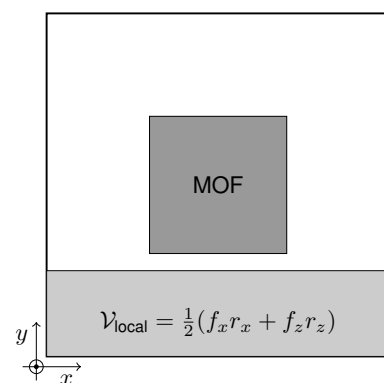


Figure 5.48: Pressure calculation from molecular dynamics in the presence of a MOF grain (dark gray). The local virial average $\mathcal{V}_{\text{local}}$ is restricted to particles within the light gray domain.

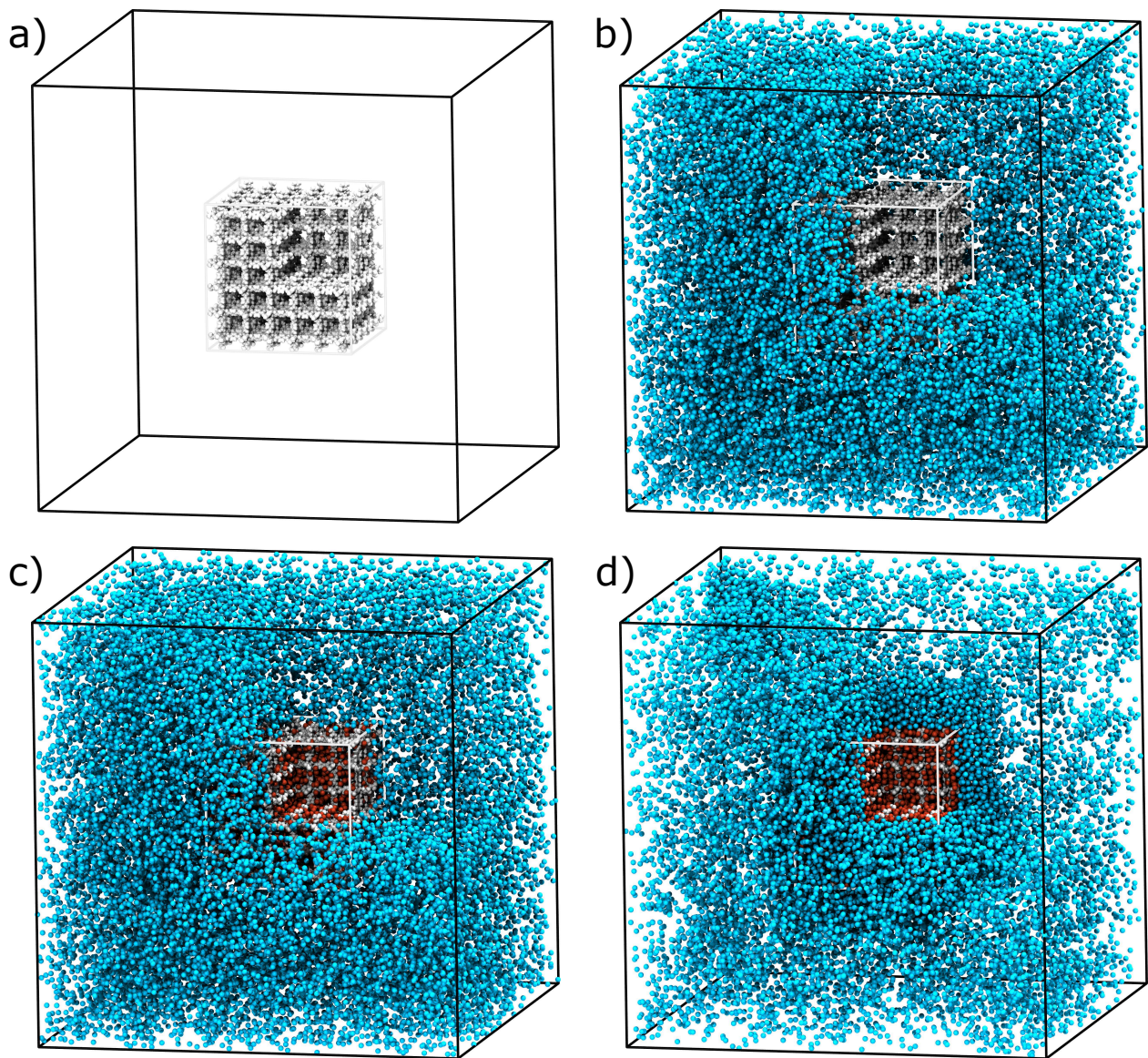


Figure 5.49: Sample preparation for molecular dynamics simulations of the adsorption kinetics. After placing the single MOF grain (in white) in the center of the cubic simulation box with linear dimension $L = 223.8 \text{ K}$ (a), methane particles are placed outside the grain (b). After certain simulation time, particles will be adsorbed (adsorbed particles are colored in red) and depending on the temperature, different equilibrium states are obtained (c) and (d) for 263.9 and 167.1 K , respectively. For clarity, the top-front-right octant has been cut out of the snapshot.

(McDonald, 2006)

$$P = \rho k_B T + \frac{1}{3V} \left\langle \sum_{i < j} \mathbf{f}(\mathbf{r}_{ij}) \cdot \mathbf{r}_{ij} \right\rangle, \quad (5.16)$$

where ρ is the particle density, k_B the Boltzmann constant and T the temperature. $\mathbf{f}(\mathbf{r}_{ij})$ is the force between particles with index i and j with distance $\mathbf{r}_{ij} = \mathbf{r}_i - \mathbf{r}_j$.

Selecting slabs spanning the whole system in two spatial directions but restricting in the other, modifies the second term in the above

equation such that

$$P = \rho k_B T + \frac{1}{2V} \left\langle \sum_{i < j} (f_\alpha r_\alpha + f_\beta r_\beta) \right\rangle, \quad (5.17)$$

where α, β are the dimensions of the domain where particles are not directly affected by the MOF and span the full system; in the above example as shown in Figure 5.50 these are x and z . To explore different pressure regions, the total system size is tuned, while leaving the MOF grain unchanged. To allow a selection of particles in the simulation on the GPU with CUDA, HALMD has been extended to support selecting particles within a certain sub-volume of the simulation domain. For the particle selection a stream compaction algorithm is used based on parallel prefix sums (Horn, 2005; Harris, Sengupta, and Owens, 2007). In total, we have seven regions, six slabs outside the MOF grain and a region inside the MOF, for counting the number of particles adsorbed. After equilibration, the lateral pressure tensor elements are then averaged over all slabs to calculate the pressure according to Eq. (5.16).

To characterize the density profile in this inhomogeneous system by calculating a cubic distribution function $g_c(r)$ around the center of the MOF grain. It is very similar to the radial distribution function, but instead of using spherical shells, cuboidal shells are used, taking the symmetry of the MOF into account.

Results and Discussion

We observe very different adsorption behavior between $T = 189.8$ and 167.1 K. At temperatures close to and above the bulk critical temperature of methane a homogeneous fluid phase both in- and outside the MOF forms. While the particle density is higher in the MOF, the influence of the MOF itself is in the range of a few Ångström and quickly reaches its bulk value (see Figure 5.52b). The Methane density inside IRMOF-1 increases steadily with compression, a saturation of the adsorption is not visible in the tested parameter range.

For lower temperatures, the MOF grain acts as a condensation center, i.e. liquid droplets form only inside and around the MOF – similar to heterogeneous nucleation, but it will always be around the IRMOF-1 grain. At smaller system sizes, when the total pressure is below the coexistence pressure of vapor–liquid phase transition of this system, the MOF gets filled homogeneously and only further compression of the simulation box causes liquid droplet to grow beyond the MOF boundaries (cf. Figure 5.50). To test if this is the vapor–liquid coexistence we compared the densities outside the MOF with coexistence densities of bulk methane at 167.1 K: The density of the gas phase outside has been determined as $\rho_v = 0.031$ g/cm³ and liquid density of $\rho_l = 0.305$ g/cm³ which is in good agreement to the coexistence densities found in the CH₄ bulk phase diagram $\rho_v^{\text{bulk}} = 0.034$ g/cm³ and $\rho_l^{\text{bulk}} = 0.32$ g/cm³, (see also Figure 5.51 (p. 88)). This effect can also be seen in Figure 5.53b, where the local

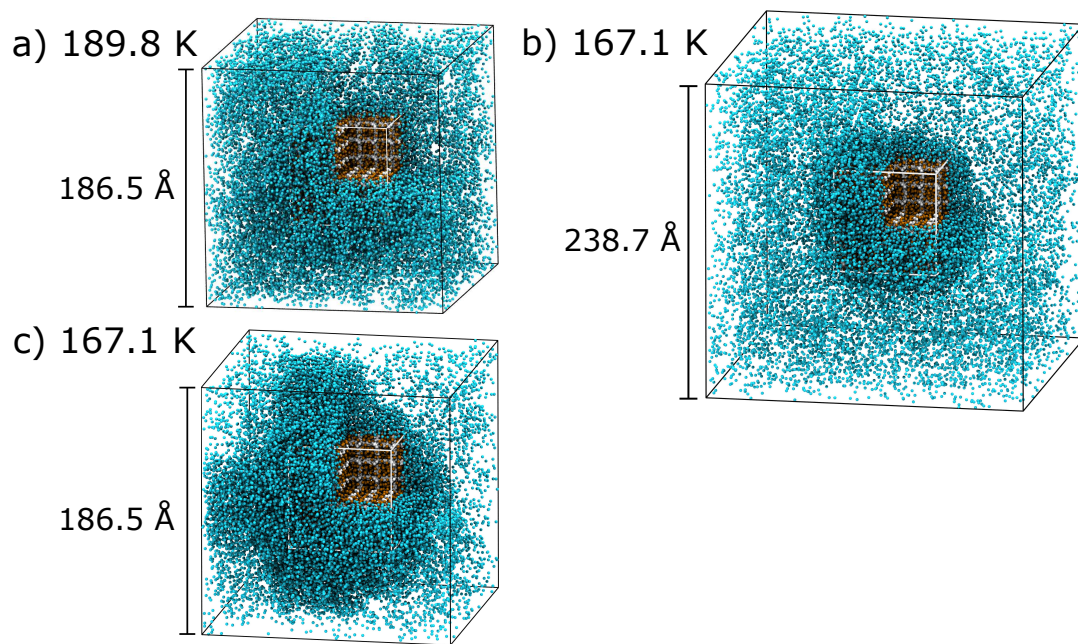


Figure 5.50: Cuts through equilibrium configurations for 3×10^5 methane particles with $3 \times 3 \times 3$ unit cells of IRMOF-1 in a cubic system with periodic boundary conditions. To make the inside visible the system is cut open, adsorbed methane in white, methane outside the MOF is turquoise, MOF atoms are white. a) At a temperature of 189.8 K, the system is homogeneous both inside and outside the MOF grain. b), c): For 167.1 K, a liquid droplet of methane forms around the grain, surrounded by a gaseous phase. At higher pressures (or smaller system size), the liquid droplet grows outside the extents of the grain with a liquid–vapor interface.

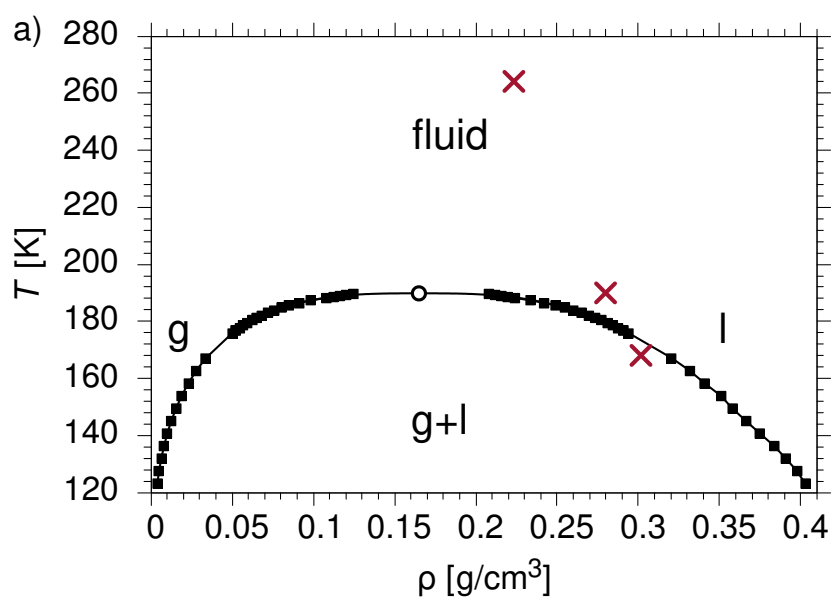


Figure 5.51: Bulk phase diagram of the liquid–gas transition with marked position corresponding to the densities in the MOF grain. The marks refer to the methane densities in the snapshot at 167.1, 189.8 and 263.9 K in Figure 5.49d, Figure 5.50a-c.

fluid density outside the grain has been determined by dividing the outer volume into sub-volumes. The formation of the liquid nucleus

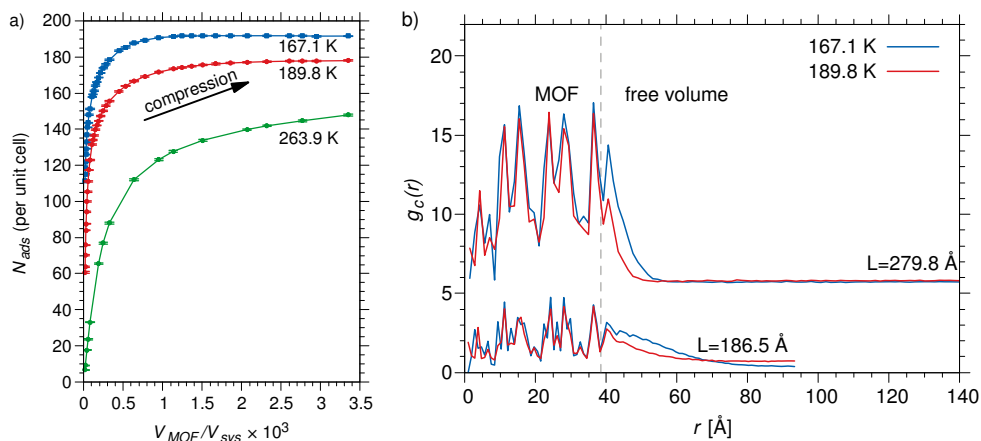


Figure 5.52: (a) Number of particles per unit cell in the MOF grain as a function of the ratio of volume of the MOF, V_{MOF} , and the volume of the total system V_{sys} . For the lower temperature, the adsorption saturates and the fluid starts to liquefy around the MOF (see also Figure 5.50). (b) Cubic distribution $g_c(r)$ of methane particles as a function of the distance to the MOF center. For clarity, the larger system is shifted by +5 on the ordinate.

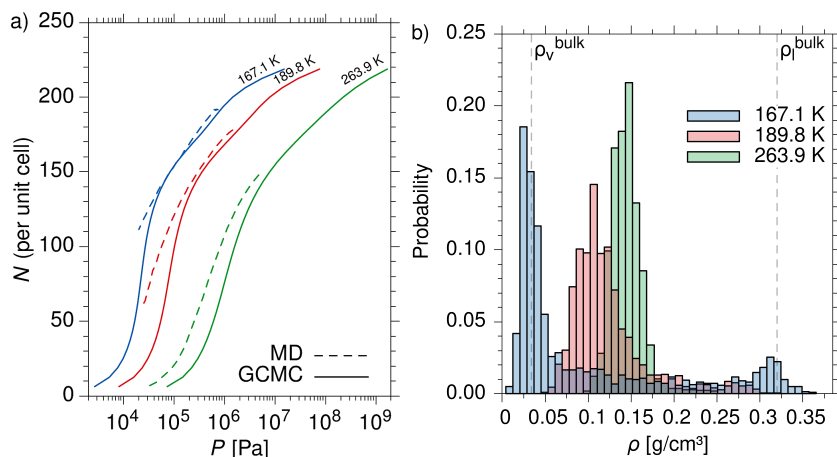


Figure 5.53: (a) Number of adsorbed particles N per unit cell as a function of pressure from Molecular Dynamics (MD) and grand-canonical Monte Carlo (GCMC) simulations. (b) Distribution of methane density in the free volume as determined from molecular dynamics simulations in a cubic system with edge length 171.6 Å. For temperatures below T_c , the distribution becomes bimodal. ρ_l^{bulk} and ρ_v^{bulk} the bulk liquid and vapor densities at 167.1 K, respectively.

inhibits further adsorption of gas molecules and saturates at ≈ 191 molecules per unit cell. To increase the loading beyond saturation will require a liquefaction of all guest particles. In practice IRMOF-1 is in powder form consisting of single crystals with diameters of a few μm (see Figure 2.8 (p. 12)) which allows formation of liquid bridges between single crystals (and has been observed in computer simulations, where a fluid bridge between periodic images arises).

This is an experimental challenge as under bulk coexistence conditions adsorption behavior is not governed by the properties of the porous material but mostly by the bulk liquid–gas phase transition.

Formation of macroscopic liquid bridges between single crystals can slow down evaporation and condensation kinetics.

CONCLUSIONS & OUTLOOK

In this work we have conducted a detailed analysis of the phase behavior of methane in three IRMOFs – IRMOF-1, -8, and -16. Caused by the heterogeneous interaction with the framework we found two novel phase transitions where (locally) heterogeneous phases can coexist with each other and investigated the structure of these phases. In IRMOFs we identify three different regions where particles can be adsorbed: First, there are the pores with their void volume, where the guest particles feel almost no interaction with the MOF and high pressures are required to fill the void space with guest molecules. Then, the weakly attractive organic linkers, such that a condensation with the formation of a wetting layer will occur at lower pressures. Third, the metallic clusters at the corners of the framework, yielding a strong attraction with the guest molecules. They are centers of adsorption at lowest pressures and a wetting layer on the metallic centers can be observed consequently. At high temperatures there is a gradual transition between these three phases, but at temperatures below ≈ 120 K one or two (depending on the MOF) first-order phase transitions can be observed in computer simulations. These two transitions are the IRMOF-surface (IS) and the IRMOF-liquid-gas (ILG) transition. In both transitions inhomogeneous bulk phases coexist with each other. While IS transition is associated with the heterogeneous interaction of the framework with the gas particles, the ILG transition is related to a filling of the pore space.

We have shown that the framework – in stark contrast to confinements in thin films – does not modify the universality class compared to bulk phase behavior and no cross-over or rounding from three- to two dimensional universal scaling occurs. The most important difference of MOFs is, that in fact the confinement does not introduce a length scale limiting the growth of the correlation length in any spatial dimension.

With our methods we predict the temperature and pressure range where these phase transitions would be expected, including how adsorption isotherms in these regimes would look like. Experimental verification of these results, however, is still pending, and the literature is quite sparse for adsorption isotherms at very low pressures and temperatures in which we expect the IS and ILG phase transitions.

Extending our study to MOFs of different pore sizes revealed that the interplay between pore size, organic linkers and metallic centers influence the coexistence regions and critical points significantly. In MOFs with small pore diameters where the inner surface is large

6

compared to the free volume, the IRMOF–surface transition coexistence region spans a wider density and temperature range, while in MOFs with longer linkers (thus larger pores) the coexistence range for the density becomes very narrow. In IRMOF-16, the MOF with the largest pore volume, the IS transition is increasingly difficult to detect, because the temperature very low and the densities of the phases are very similar. In IRMOF-16 the nature of the IS transition is still unclear, and requires further investigation to ascertain whether it is a first-order phase transition or whether it will vanish in the thermodynamic limit. The ILG transition on the other hand, is similar to the liquid–gas transition and in the limit of infinite pore volume the ILG transition would eventually become the bulk liquid–gas phase transition. In MOFs with small pores, the density of the coexisting ILG phases is very similar, and are almost indistinguishable. Hence, the IS and ILG transitions behave inversely with regard to the critical temperature when tuning the pore size of a MOF. Understanding this can become an important part for practical application when one wants to tune the adsorption behavior of fluids.

Another aspect that is not covered in this work is whether the coexistence of all three phases is possible (i.e. a triple point) – if such a state exists, it is expected to occur at very low temperatures. Due to the large free energy barriers at very low temperatures and the involved difficulties in the sampling of equilibrium states makes a further study unfeasible at this time.

Thermal undulations of the interface of coexisting IS phases are weaker than predicted by capillary wave theory, which is understood as a suppression of long-wavelength and low energy excitations due to the presence of the framework and the low temperatures at which the phase transitions are observable. This suppression is stronger in IRMOF-8, where an interface broadening due to thermal fluctuations can be observed only for very small systems. In larger systems, an interface broadening caused by capillary waves is practically absent. The external field due to the framework atoms suppress thermal fluctuations, thus inhibit capillary waves along the interface – analogously to the external field exerted by gravity.

The proposed Ising model to mimic the phase behavior in metal–organic frameworks has successfully reproduced the ILG phases and the associated first-order phase transition, which lies in the same universality class as in the atomistic model. When one varies the density of the fluid at coexistence pressure and planar interfaces can be observed, both models show an oscillation of interface tension, caused by the geometry of the framework. However, these oscillations vanish with increasing system size. Due to the simplicity of the Ising model, the computational load to simulate larger systems is greatly reduced: we had a system of $4 \times 4 \times 4$ unit cells in IRMOF-16 while the IRMOF–Ising model allowed to increase the system size to $64 \times 64 \times 64$ unit cells. As a result, we could estimate the critical Binder cumulant U_L^* with higher accuracy and have identified small corrections in comparison with the value from the bulk 3D Ising model. Nonetheless, as all framework spins of IRMOF–Ising model interact

identically with the free spins, the IS transition cannot emerge. Hence, heterogeneous framework interactions must be introduced to model the IS transition, too. This could be implemented by increasing the interaction strength or the range at the corners with the free spins, or both.

Our results from molecular dynamics simulations in IRMOF-1 show that the self-diffusion dynamics in the IS low- and high-density phases are very similar and unaffected by the critical point. Although quantitatively different, interdiffusion behaves qualitatively identical to self-diffusion. Therefore, we can conclude that the phase behavior itself is affecting the mobility of the guest particles only marginally, but the study of larger systems to support this claim especially for interdiffusion is still required.

In spite of the fact that both IS and ILG transition are within coexistence densities of bulk methane and below the bulk critical temperature, molecular dynamics simulations on a single MOF grain surrounded by bulk methane show an influence of bulk phase behavior on the adsorption kinetics. For temperatures above the bulk critical point the adsorption behavior is as expected: Particles diffuse into the MOF and at equilibrium the fluid is distributed homogeneously in- and outside the grain. In this case the equilibration process is quite fast. However, at lower temperatures a very different picture is visible, there the gas may liquefy inside the MOF while outside the MOF methane is still in the gas phase. Then, if one increases the pressure such that the grain is fully loaded, the liquid droplet will grow beyond the extents of the grain. While the simulation was limited to one single grain, in a powder with lots of small MOF crystals, intercrystalline liquid bridges can form which slow down the adsorption process. Also, slowly diffusing liquid droplets may form. As a result adsorption into the MOF will decrease and reaching equilibrium will take much longer time. Volumetric adsorption experiments realized at the Heinrich-Heine University Düsseldorf in the group of Prof. Dr. Christoph Janiak confirms this picture. When temperatures are above the bulk T_c , adsorption and desorption curves are identical – but for lower temperatures this is no longer true and a hysteresis occurs, which is found to vanish after a few adsorption-desorption cycles. This behavior is understood as slowing down of the adsorption kinetics by the condensation of gaseous methane on the surface of the MOF crystals and in the free volume of the powder.

This is problematic for adsorption measurements in general, if condensation occurs outside the porous material then the measured adsorption is much higher than the actual loading in the pores. In these cases a protocol to avoid non-equilibrium measurements is required. For example, adsorption on single crystals could be employed to avoid condensation in the free volume between crystallites. Or, applying heating and cooling cycles in order to speed up the diffusion into the pores could be a feasible method, too. Nonetheless, a close collaboration with experimental groups is required to understand the complex processes associated with adsorption in metal-organic frameworks.

There is also room for improvement in the numerical methods. GCMC simulations with successive umbrella sampling have been shown to give valuable results, as for the first time it was possible to access equilibrium states in the coexistence region of phase transitions in MOFs. Still, simplifications were required to obtain our results in a reasonable time. For one, we have only considered rigid MOFs, while in practice the framework atoms, of course, fluctuate in their position. This alone may alter the phase behavior. Even though not necessarily relevant in IRMOFs, in certain MOFs the shape of the pores may change significantly, depending on the loading of guest molecules (which is known as breathing). Further, in this work we considered only methane as the guest molecule. While the observed phase behavior is generic to some extent – as long as the interaction with the framework is heterogeneous – it is not clear how phase transitions with more complex molecules, e.g. CO₂ or H₂O with longer ranging interaction look like. Further, frameworks with pore structures of symmetries other than cubic could be certainly interesting and yield a wide range of (heterogeneous) phases. To that end, the author hopes to stimulate further studies on the phase behavior in MOFs.

BIBLIOGRAPHY

- Aarts, D. G. A. L. & Lekkerkerker, H. N. W. (2004). Confocal scanning laser microscopy on fluid–fluid demixing colloid–polymer mixtures. *Journal of Physics: Condensed Matter*, 16(38), S4231–S4242. doi:10.1088/0953-8984/16/38/035. (Cit. on p. 24)
- Allen, M. P. & Tildesley, D. J. (1989). *Computer Simulation of Liquids*. New York: Oxford University Press. (Cit. on p. 31).
- Bae, Y. S., Yazaydin, A. Ö., & Snurr, R. Q. (2010). Evaluation of the BET method for determining surface areas of MOFs and zeolites that contain Ultra-Micropores. *Langmuir*, 26(8), 5475–5483. doi:10.1021/la100449z. (Cit. on p. 9)
- Barrett, E. P., Joyner, L. G., & Halenda, P. P. (1951). The Determination of Pore Volume and Area Distributions in Porous Substances. I. Computations from Nitrogen Isotherms. *Journal of the American Chemical Society*, 73(1), 373–380. doi:10.1021/ja01145a126. arXiv:arXiv:1011.1669v3. (Cit. on p. 8)
- Batten, S. R., Champness, N. R., Chen, X.-M., Garcia-Martinez, J., Kitagawa, S., Öhrström, L., . . . Reedijk, J. (2013). Terminology of metal–organic frameworks and coordination polymers (IUPAC Recommendations 2013). *Pure and Applied Chemistry*, 85(8), 1715–1724. doi:10.1351/PAC-REC-12-11-20. (Cit. on p. 7)
- Bedeaux, D. & Weeks, J. D. (1985). Correlation functions in the capillary wave model of the liquid–vapor interface. *The Journal of Chemical Physics*, 82(2), 972–979. doi:10.1063/1.448474. (Cit. on pp. 18, 70)
- Berthelot, D. (1898). Sur le mélange des gaz. *Compt. Rendus*, 126, 1703–1706. (Cit. on p. 28).
- Bhattacharjee, J. K. & Ferrell, R. A. (1981). Dynamic scaling theory for the critical ultrasonic attenuation in a binary liquid. *Physical Review A*, 24(3), 1643–1646. (Cit. on p. 81).
- Binder, K. (1981). Finite size scaling analysis of Ising model block distribution functions. *Zeitschrift für Physik B Condensed Matter*, 140, 119–140. (Cit. on pp. 38, 47).
- Binder, K. (1982). Monte Carlo calculation of the surface tension for two- and three-dimensional lattice-gas models. *Physical Review A*, 25(3), 1699–1709. doi:10.1103/PhysRevA.25.1699. (Cit. on pp. 37, 65)
- Binder, K. (1999). Applications of Monte Carlo methods to statistical physics. *Reports on Progress in Physics*, 60(5), 487–559. doi:10.1088/0034-4885/60/5/001. (Cit. on p. 32)
- Binder, K., Block, B. J., Virnau, P., & Tröster, A. (2012). Beyond the Van Der Waals loop: What can be learned from simulating Lennard-

- Jones fluids inside the region of phase coexistence. *American Journal of Physics*, 80(12), 1099. doi:[10.1119/1.4754020](https://doi.org/10.1119/1.4754020). (Cit. on p. 37)
- Binder, K., Horbach, J., Vink, R. L. C., & De Virgiliis, A. (2008). Confinement effects on phase behavior of soft matter systems. *Soft Matter*, 4(8), 1555. doi:[10.1039/b802207k](https://doi.org/10.1039/b802207k). (Cit. on pp. 3, 24)
- Binder, K. & Landau, D. P. (1984). Finite-size scaling at first-order phase transitions. *Physical Review B*, 30(3), 1477–1485. doi:[10.1103/PhysRevB.30.1477](https://doi.org/10.1103/PhysRevB.30.1477). (Cit. on pp. 35, 36, 46)
- Binder, K. & Landau, D. P. (1992). Capillary condensation in the lattice gas model: A Monte Carlo study. *The Journal of Chemical Physics*, 96(2), 1444–1454. doi:[10.1063/1.462180](https://doi.org/10.1063/1.462180). (Cit. on p. 24)
- Binder, K., Landau, D. P., & Müller, M. (2003). Monte Carlo Studies of Wetting, Interface Localization and Capillary Condensation. *Journal of Statistical Physics*, 110(3-6), 1411–1514. doi:[10.1023/A:1022173600263](https://doi.org/10.1023/A:1022173600263). (Cit. on p. 24)
- Biswas, S., Grzywa, M., Nayek, H. P., Dehnen, S., Senkovska, I., Kaskel, S., & Volkmer, D. (2009). A cubic coordination framework constructed from benzobistriazolate ligands and zinc ions having selective gas sorption properties. *Dalton transactions*, (33), 6487–95. doi:[10.1039/b904280f](https://doi.org/10.1039/b904280f). (Cit. on p. 13)
- Borgs, C. & Kotecký, R. (1990). A rigorous theory of finite-size scaling at first-order phase transitions. *Journal of Statistical Physics*, 61(1-2), 79–119. doi:[10.1007/BF01013955](https://doi.org/10.1007/BF01013955). (Cit. on pp. 35, 36)
- Braun, E., Chen, J. J., Schnell, S. K., Lin, L. C., Reimer, J. A., & Smit, B. (2015). Nanoporous Materials Can Tune the Critical Point of a Pure Substance. *Angewandte Chemie International Edition*, 54(48), 14349–14352. doi:[10.1002/anie.201506865](https://doi.org/10.1002/anie.201506865). (Cit. on p. 2)
- Brézin, E. & Zinn-Justin, J. (1985). Finite size effects in phase transitions. *Nuclear Physics B*, 257, 867–893. doi:[10.1016/0550-3213\(85\)90379-7](https://doi.org/10.1016/0550-3213(85)90379-7). (Cit. on p. 69)
- Brunauer, S., Emmett, P. H., & Teller, E. (1938). Adsorption of Gases in Multimolecular Layers. *Journal of the American Chemical Society*, 60(1), 309–319. doi:[10.1021/ja01269a023](https://doi.org/10.1021/ja01269a023). (Cit. on p. 1)
- Buff, F. P., Lovett, R. A., & Stillinger Jr, F. H. (1965). Interfacial density profile for fluids in the critical region. *Physical Review Letters*, 15(15), 621–623. (Cit. on p. 18).
- Cahn, J. W. & Hilliard, J. E. (1958). Free Energy of a Nonuniform System. I. Interfacial Free Energy. *The Journal of Chemical Physics*, 28(2), 258–267. doi:[10.1063/1.1744102](https://doi.org/10.1063/1.1744102). (Cit. on p. 21)
- Cheetham, A. K., Férey, G., & Loiseau, T. (1999). Open-Framework Inorganic Materials. *Angewandte Chemie International Edition*, 38(22), 3268–3292. doi:[10.1002/\(SICI\)1521-3773\(19991115\)38:22<3268::AID-ANIE3268>3.0.CO;2-U](https://doi.org/10.1002/(SICI)1521-3773(19991115)38:22<3268::AID-ANIE3268>3.0.CO;2-U). (Cit. on p. 9)
- Cipra, B. A. (1987). An introduction to the Ising Model. *The American Mathematical Monthly*, 94(11), 937–959. (Cit. on p. 17).
- Colberg, P. H. & Höfling, F. (2011). Highly accelerated simulations of glassy dynamics using GPUs: Caveats on limited floating-point precision. *Computer Physics Communications*, 182(5), 1120–1129.

- doi:10.1016/j.cpc.2011.01.009. arXiv: 0912.3824. (Cit. on pp. 41, 80)
- Coudert, F.-X., Boutin, A., Fuchs, A. H., & Neimark, A. V. (2013). Adsorption Deformation and Structural Transitions in Metal–Organic Frameworks: From the Unit Cell to the Crystal. *The Journal of Physical Chemistry Letters*, 4(19), 3198–3205. doi:10.1021/jz4013849. (Cit. on p. 12)
- Darken, L. S. (1949). Diffusion of carbon in austenite with a discontinuity in composition. *Trans. Aime*, 180(430-438), 53. (Cit. on p. 41).
- Das, S. K., Horbach, J., Binder, K., Fisher, M. E., & Sengers, J. V. (2006). Static and dynamic critical behavior of a symmetrical binary fluid: a computer simulation. *The Journal of Chemical Physics*, 125(2), 024506. doi:10.1063/1.2215613. (Cit. on pp. 81, 82)
- Dietrich, S. (1999). New physical phases induced by confinement. *Journal of Physics: Condensed Matter*, 10(49), 11469–11471. doi:10.1088/0953-8984/10/49/033. (Cit. on p. 23)
- Dubbeldam, D., Frost, H., Walton, K. S., & Snurr, R. Q. (2007). Molecular simulation of adsorption sites of light gases in the metal-organic framework IRMOF-1. *Fluid Phase Equilibria*, 261(1-2), 152–161. doi:10.1016/j.fluid.2007.07.042. (Cit. on p. 45)
- Düren, T., Sarkisov, L., Yaghi, O. M., & Snurr, R. Q. (2004). Design of new materials for methane storage. *Langmuir*, (9), 2683–2689. (Cit. on p. 28).
- Eddaoudi, M., Kim, J., Rosi, N. L., Vodak, D. T., Wachter, J., O’Keeffe, M., & Yaghi, O. M. (2002). Systematic Design of Pore Size and Functionality in Isorecticular MOFs and Their Application in Methane Storage. *Science*, 295(5554), 469–472. doi:10.1126/science.1067208. (Cit. on pp. 2, 51)
- Errington, J. R. (2003). Direct calculation of liquid–vapor phase equilibria from transition matrix Monte Carlo simulation. *The Journal of Chemical Physics*, 118(22), 9915. doi:10.1063/1.1572463. (Cit. on p. 34)
- Eshraghi, M. (2015). *Interfaces of Methane in Metal Organic Frameworks (MOFs)* (Master Thesis, Heinrich-Heine Universität Düsseldorf). (Cit. on p. 64).
- Fairen-Jimenez, D., Seaton, N. A., & Düren, T. (2010). Unusual adsorption behavior on metal-organic frameworks. *Langmuir*, 26(18), 14694–14699. doi:10.1021/la102831e. (Cit. on p. 45)
- Farha, O. K., Eryazici, I., Jeong, N. C., Hauser, B. G., Wilmer, C. E., Sarjeant, A. A., ... Hupp, J. T. (2012). Metal-Organic Framework Materials with Ultrahigh Surface Areas: Is the Sky the Limit? *Journal of American Chemical Society*, 134(36), 15016–15021. doi:10.1021/ja3055639. (Cit. on p. 9)
- Farrusseng, D. (2011). *Metal-organic frameworks: applications from catalysis to gas storage*. John Wiley & Sons. doi:10.1002/9783527635856. (Cit. on p. 1)
- Feldblyum, J. I., Dutta, D., Wong-Foy, A. G., Dailly, A., Imirzian, J., Gidley, D. W., & Matzger, A. J. (2013). Interpenetration, porosity, and high-pressure gas adsorption in Zn 4O(2,6-naphthalene di-

- carboxylate)³. *Langmuir*, 29(25), 8146–8153. doi:10.1021/la401323t. (Cit. on p. 9)
- Fernandez, L. A., Martin-Mayor, V., Seoane, B., & Verrocchio, P. (2012). Equilibrium fluid-solid coexistence of hard spheres. *Physical Review Letters*, 108(16), 165701. doi:10.1103/PhysRevLett.108.165701. arXiv: arXiv:1103.2599v2. (Cit. on p. 73)
- Fernandez, L. A., Martin-Mayor, V., & Yllanes, D. (2009). Tethered Monte Carlo: Computing the effective potential without critical slowing down. *Nuclear Physics B*, 807(3), 424–454. doi:10.1016/j.nuclphysb.2008.07.009. arXiv: arXiv:0806.0543v3. (Cit. on p. 73)
- Ferrenberg, A. M. & Swendsen, R. H. (1988). New Monte Carlo technique for studying phase transitions. *Physical Review Letters*, 61(23), 2635–2638. doi:10.1103/PhysRevLett.61.2635. arXiv: 9709064 [cond-mat]. (Cit. on pp. 35, 46)
- Fisher, M. E. & Nakanishi, H. (1981). Scaling theory for the criticality of fluids between plates. *The Journal of Chemical Physics*, 75(12), 5857–5863. doi:10.1063/1.442035. (Cit. on p. 75)
- Fisk, S. & Widom, B. (1969). Structure and Free Energy of the Interface between Fluid Phases in Equilibrium near the Critical Point. *The Journal of Chemical Physics*, 50(8), 3219–3227. doi:10.1063/1.1671544. (Cit. on p. 21)
- Gau, H., Herminghaus, S., Lenz, P., & Lipowsky, R. (1999). Liquid Morphologies on Structured Surfaces: From Microchannels to Microchips. *Science*, 283(5398), 46–49. doi:10.1126/science.283.5398.46. (Cit. on p. 25)
- Gelb, L. D., Gubbins, K. E., Radhakrishnan, R., & Sliwinski-Bartkowiak, M. (2000). Phase separation in confined systems. *Reports on Progress in Physics*, 63(4), 727–727. doi:10.1088/0034-4885/63/4/501. (Cit. on pp. 1, 23)
- Gelfand, M. P. & Fisher, M. E. (1990). Finite-size effects in fluid interfaces. *Physica A: Statistical Mechanics and its Applications*, 166(1), 1–74. doi:10.1016/0378-4371(90)90099-E. (Cit. on p. 67)
- Hansen, J.-P. & McDonald, I. R. (2006). *Theory of Simple Liquids*. Academic Press. (Cit. on p. 85).
- Harris, M., Sengupta, S., & Owens, J. D. (2007). Parallel Prefix Sum (Scan) with CUDA. *GPU gems*, 3(39), 851–876. (Cit. on p. 87).
- Hasenbusch, M. (2010). A finite size scaling study of lattice models in the three-dimensional Ising universality class. *Physical Review B*, 82(17), 174433. doi:10.1103/PhysRevB.82.174433. arXiv: arXiv:1004.4486v3. (Cit. on pp. 76, 77)
- Hastings, W. K. (1970). Monte carlo sampling methods using Markov chains and their applications. *Biometrika*, 57(1), 97–109. doi:10.1093/biomet/57.1.97. (Cit. on p. 31)
- He, Y., Zhou, W., Qian, G., & Chen, B. (2014). Methane storage in metal-organic frameworks. *Chemical Society reviews*, 43(16), 5657–5678. doi:10.1039/c4cs00032c. (Cit. on p. 11)
- Höft, N. & Horbach, J. (2015). Condensation of methane in the metal-organic framework IRMOF-1: Evidence for two critical points. *Journal of the American Chemical Society*, 137(32), 10199–10204. doi:10.1021/jacs.5b04077. (Cit. on pp. 45–49)

- Horbach, J., Das, S. K., Griesche, A., Macht, M. P., Frohberg, G., & Meyer, A. (2007). Self-diffusion and interdiffusion in Al₈₀Ni₂₀ melts: Simulation and experiment. *Physical Review B*, 75(17), 174304. doi:10.1103/PhysRevB.75.174304. (Cit. on p. 40)
- Horn, D. (2005). Stream reduction operations for GPGPU applications. *Gpu gems*, 2, 573–589. (Cit. on p. 87).
- Ising, E. (1925). Beitrag zur Theorie des Ferromagnetismus. *Zeitschrift für Physik*, 31(1), 253–258. doi:10.1007/BF02980577. (Cit. on p. 16)
- Janiak, C. & Vieth, J. K. (2010). MOFs, MILs and more: concepts, properties and applications for porous coordination networks (PCNs). *New Journal of Chemistry*, 34(11), 2366. doi:10.1039/c0nj00275e. (Cit. on p. 7)
- Jasnow, D. (1984). Critical phenomena at interfaces. *Reports on Progress in Physics*, 47(9), 1059–1132. doi:10.1088/0034-4885/47/9/001. (Cit. on p. 69)
- Jeazet, H. B. T., Koschine, T., Staudt, C., Raetzke, K., & Janiak, C. (2013). Correlation of gas permeability in a metal-organic framework MIL-101(Cr)-polysulfone mixed-matrix membrane with free volume measurements by positron annihilation lifetime spectroscopy (PALS). *Membranes*, 3(4), 331–353. doi:10.3390/membranes3040331. (Cit. on p. 11)
- June, R. L., Bell, A. T., & Theodorou, D. N. (1990). Molecular dynamics study of methane and xenon in silicalite. *Journal of Physical Chemistry*, 94(21), 8232–8240. (Cit. on p. 29).
- Kamieniarz, G. & Blote, H. W. J. (1993). Universal ratio of magnetization moments in two-dimensional Ising models. *Journal of Physics A: Mathematical and General*, 26(2), 201–212. doi:10.1088/0305-4470/26/2/009. (Cit. on pp. 47, 57)
- Kundu, J., Pascal, T., Prendergast, D., & Whitelam, S. (2016). Selective gas capture via kinetic trapping. *Physical Chemistry Chemical Physics*. doi:10.1039/C6CP03940E. arXiv: 1606.00065. (Cit. on p. 79)
- Landau, D. P. & Binder, K. (2014). *A guide to Monte Carlo simulations in statistical physics* (Third Edit). Cambridge University Press. (Cit. on p. 38).
- Landau, L. D. & Lifshitz, E. M. (1980). *Statistical Physics, Part 1* (3rd ed.). Pergamon Oxford. (Cit. on p. 68).
- Langmuir, I. (1916). The Constitution and Fundamental Properties of Solids and Liquids. Part I. Solids. *Journal of the American Chemical Society*, 38(11), 2221–2295. doi:10.1021/ja02268a002. (Cit. on p. 1)
- Langmuir, I. (1918). The Adsorption of Gases on Plane Surfaces of Glass, Mica and Platinum. *Journal of the American Chemical Society*, 40(9), 1361–1403. doi:10.1021/ja02242a004. (Cit. on p. 1)
- Lee, T. D. & Yang, C. N. (1952). Statistical theory of equations of state and phase transitions. II. Lattice gas and ising model. *Physical Review*, 87(3), 410–419. doi:10.1103/PhysRev.87.410. (Cit. on p. 23)
- Lei, X.-g., Jockusch, S., Ottaviani, M. F., & Turro, N. J. (2003). In situ EPR investigation of the addition of persistent benzyl radicals to acrylates on ZSM-5 zeolites. Direct spectroscopic detection of the initial steps in a supramolecular photopolymerization.

- Photochemical & Photobiological Sciences*, 2(11), 1095–1100. doi:10.1039/b307735g. (Cit. on p. 10)
- Lenz, P. & Lipowsky, R. (1998). Morphological Transitions of Wetting Layers on Structured Surfaces. *Physical Review Letters*, 80(9), 1920–1923. doi:10.1103/PhysRevLett.80.1920. (Cit. on pp. 3, 25)
- Li, H., Eddaoudi, M., O’Keeffe, M., & Yaghi, O. M. (1999). Design and synthesis of an exceptionally stable and highly porous metal-organic framework. *Nature*, 402(6759), 276–279. (Cit. on p. 3).
- Li, J.-R., Kuppler, R. J., & Zhou, H.-C. (2009). Selective gas adsorption and separation in metal-organic frameworks. *Chemical Society Reviews*, 38(5), 1477–1504. doi:10.1039/b802426j. (Cit. on p. 79)
- Liu, B., Yang, Q., Xue, C., Zhong, C., Chen, B., & Smit, B. (2008). Enhanced Adsorption Selectivity of Hydrogen/Methane Mixtures in Metal–Organic Frameworks with Interpenetration: A Molecular Simulation Study. *The Journal of Physical Chemistry C*, 112(26), 9854–9860. doi:10.1021/jp802343n. (Cit. on p. 45)
- Llewellyn, P. L., Bourrelly, S., Serre, C., Vimont, A., Daturi, M., Hamon, L., ... Férey, G. (2008). High uptakes of CO₂ and CH₄ in mesoporous metal-organic frameworks MIL-100 and MIL-101. *Langmuir*, 24(14), 7245–7250. doi:10.1021/la800227x. (Cit. on p. 9)
- Loiseau, T., Serre, C., Huguenard, C., Fink, G., Taulelle, F., Henry, M., ... Férey, G. (2004). A rationale for the large breathing of the porous aluminum terephthalate (MIL-53) upon hydration. *Chemistry (Weinheim an der Bergstrasse, Germany)*, 10(6), 1373–1382. doi:10.1002/chem.200305413. (Cit. on p. 11)
- Lorentz, H. A. (1881). Ueber die Anwendung des Satzes vom Virial in der kinetischen Theorie der Gase. *Annalen der Physik*, 248(1), 127–136. doi:10.1002/andp.18812480110. (Cit. on p. 28)
- Luijten, E., Fisher, M. E., & Panagiotopoulos, A. Z. (2002). Universality Class of Criticality in the Restricted Primitive Model Electrolyte. *Physical Review Letters*, 88(18), 185701. doi:10.1103/PhysRevLett.88.185701. (Cit. on p. 47)
- Magdysyuk, O. V., Denysenko, D., Weinrauch, I., Volkmer, D., Hirscher, M., & Dinnebier, R. E. (2014). Formation of a quasi-solid structure by intercalated noble gas atoms in pores of Cu(I)-MFU-4l metal-organic framework. *Chemical Communications*, 51(4), 714–717. doi:10.1039/c4cc07554d. (Cit. on pp. 13, 56)
- Maginn, E. J., Bell, A. T., & Theodorou, D. N. (1993). Transport diffusivity of methane in silicalite from equilibrium and nonequilibrium simulations. *The Journal of Physical Chemistry*, 97(16), 4173–4181. (Cit. on p. 80).
- Martin-Mayor, V., Seoane, B., & Yllanes, D. (2011). Tethered Monte Carlo: Managing Rugged Free-Energy Landscapes with a Helmholtz-Potential Formalism. *Journal of Statistical Physics*, 144(3), 554–596. doi:10.1007/s10955-011-0261-4. arXiv: 1107.2096. (Cit. on p. 73)
- Mason, J. A., Veenstra, M., & Long, J. R. (2014). Evaluating metal–organic frameworks for natural gas storage. *Chemical Science*, 5(1), 32–51. doi:10.1039/C3SC52633J. (Cit. on pp. 1, 9)
- Metropolis, N. (1987). The beginning of the Monte Carlo method. *Los Alamos Science*, 15(584), 125–130. (Cit. on p. 30).

- Metropolis, N., Rosenbluth, A. W., Rosenbluth, M. N., Teller, A. H., & Teller, E. (1953). Equation of State Calculations by Fast Computing Machines. *The Journal of Chemical Physics*, 21(6), 1087–1092. doi:10.1063/1.1699114. arXiv: 5744249209. (Cit. on p. 31)
- Millward, A. R. & Yaghi, O. M. (2005). Metal-organic frameworks with exceptionally high capacity for storage of carbon dioxide at room temperature. *Journal of the American Chemical Society*, 127(51), 17998–17999. doi:10.1021/ja0570032. (Cit. on p. 9)
- Mueller, T. & Ceder, G. (2005). A density functional theory study of hydrogen adsorption in MOF-5. *The journal of physical chemistry. B*, 109(38), 17974–17983. doi:10.1021/jp051202q. (Cit. on p. 45)
- Nakanishi, H. & Fisher, M. E. (1982). Multicriticality of Wetting, Prewetting, and Surface Transitions. *Physical Review Letters*, 49(21), 1565–1568. (Cit. on p. 76).
- Niss, M. (2005). History of the lenz-ising model 1920-1950: From ferromagnetic to cooperative phenomena. *Archive for History of Exact Sciences*, 59(3), 267–318. doi:10.1007/s00407-004-0088-3. (Cit. on p. 16)
- Nvidia, C. (2016). *CUDA C Programming Guide v8.0*. (Cit. on p. 41).
- Palomino, M., Corma, A., Rey, F., & Valencia, S. (2010). New insights on CO₂-methane separation using LTA zeolites with different Si/Al ratios and a first comparison with MOFs. *Langmuir*, 26(3), 1910–1917. doi:10.1021/la9026656. (Cit. on p. 9)
- Pelissetto, A. & Vicari, E. (2002). Critical phenomena and renormalization-group theory. *Physics Report*, 368(6), 549–727. (Cit. on pp. 22, 46, 47).
- Privman, V. & Fisher, M. E. (1984). Universal critical amplitudes in finite-size scaling. *Physical Review B*, 30(1), 322–327. doi:10.1103/PhysRevB.30.322. (Cit. on p. 38)
- Rappé, A. & Casewit, C. (1992). UFF, a full periodic table force field for molecular mechanics and molecular dynamics simulations. *Journal of the American Chemical Society*, 114(25), 10024–10035. (Cit. on p. 28).
- Rosi, N. L., Eckert, J., Eddaoudi, M., Vodak, D. T., Kim, J., O’Keeffe, M., & Yaghi, O. M. (2003). Hydrogen Storage in Microporous Metal-Organic Frameworks. *Science*, 300(5622), 1127–1129. doi:10.1126/science.1083440. (Cit. on p. 45)
- Rouquerol, F., Rouquerol, J., Sing, K. S. W., Llewellyn, P., Maurin, G., Rouquerol, J., . . . Sing, K. S. W. (2014). *Adsorption by Powders and Porous Solids*. doi:10.1016/B978-0-08-097035-6.00012-7. (Cit. on pp. 2, 8, 9)
- Rouquerol, J., Llewellyn, P., & Rouquerol, F. (2007). Is the BET equation applicable to microporous adsorbents? *Studies in Surface Science and Catalysis*, 160, 49–56. doi:10.1016/S0167-2991(07)80008-5. (Cit. on p. 8)
- Rowsell, J. L., Spencer, E. C., Eckert, J., Howard, J. A., & Yaghi, O. M. (2005). Gas adsorption sites in a large-pore metal-organic framework. *Science*, 309(5739), 1350–1354. doi:10.1126/science.1113247. (Cit. on pp. 2, 13, 45)

- Roy, S., Dietrich, S., & Höfling, F. (2016). Structure and dynamics of binary liquid mixtures near their continuous demixing transitions. *The Journal of Chemical Physics*, 145(13), 134505. doi:10.1063/1.4963771. (Cit. on p. 81)
- Rozas, R. E. & Horbach, J. (2011). Capillary wave analysis of rough solid-liquid interfaces in nickel. *EPL (Europhysics Letters)*, 93(2), 26006. doi:10.1209/0295-5075/93/26006. (Cit. on pp. 19, 67)
- Sang, S., Chang, F., Liu, Z., He, C., He, Y., & Xu, L. (2004). Difference of ZSM-5 zeolites synthesized with various templates. *Catalysis Today*, 93, 729–734. doi:10.1016/j.cattod.2004.06.091. (Cit. on p. 9)
- Schultz, M. H. (1973). *Spline analysis*. Prentice-Hall Englewood Cliffs, NJ. (Cit. on pp. 28, 29).
- Siberio-Pérez, D. Y., Wong-Foy, A. G., Yaghi, O. M., & Matzger, A. J. (2007). Raman Spectroscopic Investigation of CH₄ and N₂ Adsorption in Metal-Organic Frameworks. *Chemistry of Materials*, 19(15), 3681–3685. doi:10.1021/cm070542g. (Cit. on p. 45)
- Sing, K. S. W. (2001). The use of nitrogen adsorption for the characterisation of porous materials. *Colloids and Surfaces A: Physicochemical and Engineering Aspects*, 187, 3–9. doi:10.1016/S0927-7757(01)00612-4. arXiv: S0927-7757(01)00612-4. (Cit. on p. 2)
- Sing, K. S. W., Everett, D. H., Haul, R. A., Moscou, L., Pierotti, R. A., Rouquerol, J., & Siemieniewska, T. (1985). Reporting physisorption data for gas/solid systems. *Pure and Applied Chemistry*, 57(4), 603–619. doi:10.1002/9783527610044.hetcat0065. (Cit. on p. 1)
- Skoulidas, A. I. & Sholl, D. S. (2002). Transport diffusivities of CH₄, CF₄, He, Ne, Ar, Xe, and SF₆ in silicalite from atomistic simulations. *The Journal of Physical Chemistry B*, 106(19), 5058–5067. (Cit. on p. 29).
- Skoulidas, A. I. & Sholl, D. S. (2005). Self-diffusion and transport diffusion of light gases in metal-organic framework materials assessed using molecular dynamics simulations. *Journal of Physical Chemistry B*, 109(33), 15760–15768. (Cit. on p. 79).
- Smit, B., Karaborni, S., & Siepmann, J. I. (1995). Computer simulations of vapor-liquid phase equilibria of n-alkanes. *The Journal of Chemical Physics*, 102(5), 2126–2140. doi:10.1063/1.469563. (Cit. on p. 28)
- Stallmach, F., Gröger, S., Künzel, V., Kärger, J., Yaghi, O. M., Hesse, M., & Müller, U. (2006). NMR studies on the diffusion of hydrocarbons on the metal-organic framework material MOF-5. *Angewandte Chemie International Edition*, 45(13), 2123–2126. doi:10.1002/anie.200502553. (Cit. on pp. 26, 82)
- Thommes, M. & Cychoz, K. A. (2014). Physical adsorption characterization of nanoporous materials: Progress and challenges. *Adsorption*, 20(2-3), 233–250. doi:10.1007/s10450-014-9606-z. (Cit. on p. 9)
- Thommes, M., Kaneko, K., Neimark, A. V., Olivier, J. P., Rodriguez-Reinoso, F., Rouquerol, J., & Sing, K. S. W. (2015). *Physisorption of gases, with special reference to the evaluation of surface area and pore size distribution (IUPAC Technical Report)* (tech. rep. No. 9-10). doi:10.1515/pac-2014-1117. (Cit. on pp. 1, 8, 9)

- Toni, M. D., Pullumbi, P., Coudert, F.-X., & Fuchs, A. H. (2010). Understanding the Effect of Confinement on the Liquid- Gas Transition: A Study of Adsorption Isotherms in a Family of Metal-Organic Frameworks. *The Journal of Physical Chemistry C*, 114(49), 21631–21637. doi:10.1021/jp108715q. (Cit. on pp. 3, 13)
- Tonigold, M., Lu, Y., Mavrandonakis, A., Puls, A., Staudt, R., Möllmer, J., ... Volkmer, D. (2011). Pyrazolate-based cobalt(II)-containing metal-organic frameworks in heterogeneous catalytic oxidation reactions: Elucidating the role of entatic states for biomimetic oxidation processes. *Chemistry - A European Journal*, 17(31), 8671–8695. doi:10.1002/chem.201003173. arXiv: arXiv:1408.1149. (Cit. on p. 12)
- Tranchemontagne, D. J., Hunt, J. R., & Yaghi, O. M. (2008). Room temperature synthesis of metal-organic frameworks: MOF-5, MOF-74, MOF-177, MOF-199, and IRMOF-0. *Tetrahedron*, 64(36), 8553–8557. doi:10.1016/j.tet.2008.06.036. (Cit. on p. 12)
- Tuckerman, M. E. (2010). *Statistical mechanics: theory and molecular simulation*. (Cit. on p. 20).
- Uzun, A. & Keskin, S. (2014). Site characteristics in metal organic frameworks for gas adsorption. *Progress in Surface Science*, 89(1), 56–79. doi:10.1016/j.progsurf.2013.11.001. (Cit. on p. 45)
- Varnik, F., Baschnagel, J., & Binder, K. (2000). Molecular dynamics results on the pressure tensor of polymer films. *The Journal of Chemical Physics*, 113(10), 4444. doi:10.1063/1.1288390. arXiv: 0011412 [cond-mat]. (Cit. on p. 85)
- Vink, R. L. C., De Virgiliis, A., Horbach, J., & Binder, K. (2006). Phase diagram and structure of colloid-polymer mixtures confined between walls. *Physical Review E*, 74(3), 031601. doi:10.1103/PhysRevE.74.031601. arXiv: 0607086 [cond-mat]. (Cit. on p. 25)
- Virnau, P. & Müller, M. (2004). Calculation of free energy through successive umbrella sampling. *Journal of Chemical Physics*, 120(23), 10925–10930. doi:10.1063/1.1739216. (Cit. on pp. 34, 73)
- Virta, R. L. & Flanagan, D. M. (2015). *2014 Minerals Yearbook: Zeolites [Advance Release]*. U.S. Department of the Interior. (Cit. on p. 10).
- von Neumann, J. & Goldstine, H. H. (1947). Numerical inverting of matrices of high order. *Bulletin of the American Mathematical Society*, 53(11), 1021–1099. doi:10.1090/S0002-9939-1951-0041539-X. (Cit. on p. 27)
- Wagner, W., Saul, A., & Pruss, A. (1994). International equations for the pressure along the melting and along the sublimation curve of ordinary water substance. *Journal of Physical and Chemical Reference Data*, 23(3), 515–527. (Cit. on p. 15).
- Wallace, D. J. (1982). Critical behaviour in interfaces. In *Phase transitions cargèse 1980* (pp. 423–457). Springer. (Cit. on p. 18).
- Walton, K. S., Millward, A. R., Dubbeldam, D., Low, J. J., Yaghi, O. M., Snurr, R. Q., & Frost, H. (2008). Understanding Inflections and Steps in Carbon Dioxide Adsorption Isotherms in Metal-Organic Frameworks Understanding Inflections and Steps in Carbon Dioxide Adsorption Isotherms in Metal-Organic Frameworks.

- Journal of the American Chemical Society*, 130(2), 406–407. doi:10.1021/ja076595g. (Cit. on p. 45)
- Walton, K. S. & Snurr, R. Q. (2007). Applicability of the BET method for determining surface areas of microporous metal-organic frameworks. *Journal of the American Chemical Society*, 129(27), 8552–8556. (Cit. on pp. 9, 26).
- Wang, F. & Landau, D. P. (2001). Efficient, multiple-range random walk algorithm to calculate the density of states. *Physical Review Letters*, 86(10), 2050–2053. doi:10.1103/PhysRevLett.86.2050. arXiv: 0011379 [cond-mat]. (Cit. on p. 34)
- Wang, M. Q. & Huang, H. S. (2000). *A Full Fuel-Cycle Analysis of Energy and Emissions Impacts of Transportation Fuels Produced from Natural Gas*. Argonne National Lab., IL (US). doi:10.2172/750803. (Cit. on p. 2)
- Wang, S. & Peng, Y. (2010). Natural zeolites as effective adsorbents in water and wastewater treatment. *Chemical Engineering Journal*, 156(1), 11–24. doi:10.1016/j.cej.2009.10.029. arXiv: arXiv:1011.1669v3. (Cit. on p. 10)
- Weeks, J. D. (1977). Structure and thermodynamics of the liquid–vapor interface. *The Journal of Chemical Physics*, 67(7), 3106–3121. doi:10.1063/1.435276. (Cit. on pp. 18, 70)
- Weeks, J. D. (1984). Scaling Relations between Correlations in the Liquid-Vapor Interface and the Interface Width. *Journal of Chemical Information and Modeling*, 52(24), 2160–2163. (Cit. on p. 19).
- Wesselingh, J. A. & Krishna, R. (2000). *Mass transfer in multicomponent mixtures*. Delft University Press. (Cit. on p. 79).
- Widom, B. & Rowlinson, J. S. (1970). New model for the study of liquid-vapor phase transitions. *The Journal of Chemical Physics*, 52(1970), 1670. doi:10.1063/1.1673203. (Cit. on pp. 37, 47)
- Wikimedia Commons. (2010). Kristallstruktur von MIL-53_ht mit gelben Kugeln. Retrieved September 6, 2016, from <https://commons.wikimedia.org/wiki/File:MIL-53ht.png>. (Cit. on p. 11)
- Wilms, D., Winkler, A., Virnau, P., & Binder, K. (2010). Rounding of Phase Transitions in Cylindrical Pores. *Physical Review Letters*, 105(4), 045701. doi:10.1103/PhysRevLett.105.045701. arXiv: 1007.0138. (Cit. on p. 24)
- Yang, C. N. & Lee, T. D. (1952). Statistical theory of equations of state and phase transitions. I. Theory of condensation. *Physical Review*, 87(3), 404–409. doi:10.1103/PhysRev.87.404. (Cit. on p. 23)
- Yildirim, T. & Hartman, M. R. (2005). Direct observation of hydrogen adsorption sites and nanocage formation in metal-organic frameworks. *Physical Review Letters*, 95(21), 215504. doi:10.1103/PhysRevLett.95.215504. arXiv: 0507220 [cond-mat]. (Cit. on p. 45)
- Yilmaz, B., Trukhan, N., & Müller, U. (2012). Industrial Outlook on Zeolites and Metal Organic Frameworks. *Chinese Journal of Catalysis*, 33(1), 3–10. doi:10.1016/S1872-2067(10)60302-6. (Cit. on p. 10)
- Zhang, Y., Sunarso, J., Liu, S., & Wang, R. (2013). Current status and development of membranes for CO₂/CH₄ separation: A review. *International Journal of Greenhouse Gas Control*, 12, 84–107. doi:10.1016/j.ijggc.2012.10.009. (Cit. on p. 11)

Zhou, W., Wu, H., Hartman, M. R., & Yildirim, T. (2007). Hydrogen and methane adsorption in metal-organic frameworks: A high-pressure volumetric study. *Journal of Physical Chemistry C*, 111(44), 16131–16137. (Cit. on p. 59).

EIDESSTATTLICHE VERSICHERUNG

Ich versichere an Eides Statt, dass die Dissertation von mir selbständig und ohne unzulässige fremde Hilfe unter Beachtung der „Grundsätze zur Sicherung guter wissenschaftlicher Praxis an der Heinrich-Heine-Universität Düsseldorf“ erstellt worden ist.

Düsseldorf, den 27.10.2016

Nicolas Höft